High-throughput mutagenesis identifies regulatory interactions and drug resistance mechanisms in Src kinase

Ethan Ahler

A dissertation

submitted in partial fulfillment of the

requirements for the degree of

Doctor of Philosophy

University of Washington

2019

Reading Committee:

Douglas M. Fowler, Chair

Dustin J. Maly

Christine Queitsch

Program Authorized to Offer Degree:

Molecular and Cellular Biology

University of Washington

Abstract

High-throughput mutagenesis identifies regulatory interactions and drug resistance mechanisms in Src kinase

Ethan Ahler

Chair of the Supervisory Committee:
Dr. Douglas M. Fowler
Department of Genome Sciences

The majority of the human proteome is phosphorylated by the eukaryotic protein kinase (EPK) enzyme family. EPKs are subject to multiple layers of regulation that modulate both the magnitude and specificity of their activity and this regulation is crucial, as loss of control over activity often results in disease. Commonly, this regulation is governed by interactions between the catalytic kinase domain and other regions of the protein. A classic example of intramolecular EPK regulation was delineated in the tyrosine kinase Src, whose regulatory SH2 and SH3 domains interface with its catalytic domain to constrain activity. Although this mechanism of Src intramolecular regulation is broadly well established, our knowledge of how the individual catalytic domain residues contribute to regulation is less well understood. To investigate this, we use saturation mutagenesis to functionally interrogate thousands of single missense mutants of the catalytic domain of Src kinase. We identify 27 residues located throughout the catalytic domain that, when mutated, result in increased Src activity. As expected, several of these residues hyper-activate Src by disrupting known mechanisms of SH2 or SH3 domain regulation. However, we also identify a patch of residues on Src's C-lobe which strongly affects its activity but whose mechanism cannot be explained by our current understanding of Src regulation. We investigate this patch and surprisingly find that mutations here affect activity in a manner dependent on Src's membrane-binding SH4 domain. Moreover, these mutations cause Src to associate more with membranes both *in vitro* and in cells, implying these mutations alter SH4 domain conformation. Our results suggest a novel functional interaction between Src's SH4 and catalytic domain that couples localization and activity and thus our study adds an additional layer to the canonical mechanisms of Src kinase regulation. In a follow-up project, we use this same system to systematically identify mutations that confer resistance to three different conformation-selective inhibitors of Src. We identify dozens of

resistance mutations, including some that are specific to a given inhibitor. These "unique" resistance mutations are of particular interest, because these residues may contribute to the adoption of specific conformations of Src's catalytic domain. In summary, this work uncovers a previously unidentified regulatory role for Src's SH4 domain. Moreover, it lays the groundwork for future investigations into the nature of these newly identified resistance mutants for conformation-selective inhibitors.

TABLE OF CONTENTS

LIST OF FIGURES

LIST OF TABLES

ACKNOWLEDGEMENTS

This work would not have been possible without the incredible guidance, support, and assistance offered by many people. First, thank you to my pre-graduate school scientific mentors, Drs. Heather Christofk, Karen Ottemann, and Annah Rolig for the inspiration to continue a career in research. Second, thank you to my graduate school thesis committee, Drs. Jesse Bloom, Maitreya Dunham, Dusty Maly, and Christine Queitsch, for all of your helpful comments, words of wisdom, and support over the years. In particular, Dusty served as a second mentor to me for many of my projects, and his enthusiasm and knowledge has been so important in driving these projects forward. Several students in Dusty's lab: Sujata, Emily, and Linglan, deserve special shouts outs for the incredible amount of work they put into these team efforts. I am very fortunate to have found such an excellent group of collaborators. Graduate school is tough, and having a supportive working environment and friends group is essential. Thank you to all members of the Fowler lab, past and present, for making it great place to work. In particular, Kenny for all the science and career advice, Vanessa for being the best baymate, and Kate for all the scientific and emotional support. Thanks to my graduate program, MCB, and all its amazing staff and students, especially my cohort members Laura, Kelsey, and Piero. And finally, thank you to my graduate advisor Dr. Douglas Fowler. Doug has been an absolutely fantastic and supportive mentor, both scientifically and personally, and I am so grateful for the experience of working in his lab.

Chapter 1. INTRODUCTION

1.1 OPENING COMMENTS

Cells face an ever-changing landscape of molecular and chemical stimuli. To survive, cells must decipher these messages in real-time and initiate appropriate cellular responses. These cell signaling events are primarily orchestrated through a diverse repertoire of signaling proteins. One of the best studied classes of these signaling proteins are the kinases, enzymes that chemically "tag" other proteins and thereby affect the function, localization, or interactions of the marked protein. Almost every basic cellular process—from growth and division, to DNA replication and energy metabolism—is, to some extent, coordinated by kinases. Consequently, kinases are among the most commonly dysregulated families of proteins that cause human diseases.

Given the exceptional importance of kinases to both normal and disease biology, much effort has been devoted to the study of kinase regulation. Kinases are often governed by protein-intrinsic mechanisms that ensure precise, spatiotemporal control of activity. This regulation can be surprisingly sensitive; a single amino acid mutation is often sufficient to completely derange a kinase's activity. Indeed, mutations in kinases are a common cause of the haywire cellular signaling that drives diseases like cancer. However, mutations can also serve as a powerful experimental tool for understanding the molecular principles that dictate kinase function. For my thesis work in Dr. Douglas Fowler's lab, I harnessed the power of high-throughput mutagenesis to investigate fundamental aspects of Src (pronounced *sark*) kinase biology. To motivate my work, I begin by introducing Src, a protein that has fundamentally informed our understanding of both cellular signaling and oncogenesis.

1.2 SRC: A MODEL FOR SIGNALING AND TUMORIGENESIS

Few proteins have had as remarkable a scientific history as Src. As the first discovered tyrosine kinase, (previously, only serine/threonine kinases were known) Src has served as the model to base much of our understanding of tyrosine phosphorylation on (Hunter, 2015). Moreover, Src has the distinction of being the subject of not one, but two separate Nobel Prizes in Medicine: the first in 1966 for the discovery of virally-transmitted cancers and the second in 1989 for its identification as the first proto-oncogene—both major advances in cancer biology (Lipsick, 2019). Given Src's role in these findings, it is not an understatement to say that much of the framework through which we understand cancer was directly shaped by the study of Src.

Src is a 536 amino acid protein and is the archetypal member of the Src Family Kinases (SFKs), a group of eight cytoplasmic tyrosine kinases. Like all kinases, Src has a ~250 residue catalytic domain (CD) that catalyzes the transfer of the γ-phosphoryl group of ATP to the side-chain hydroxyl group of tyrosine residues **(Figure 1.1A**). Additionally, Src contains other domains that flank the CD, including a SH4 domain (which binds lipid membranes), a Unique domain (with poorly defined function), a SH3 domain (binds proline-rich sequences), a SH2 domain (binds phosphorylated tyrosines), and a C-terminal tail that contains a regulatory phosphorylation site (**Figure 1.1B**) (Roskoski, 2015).

Src's best established cellular role is in transducing extracellular growth and proliferative signals. Src sits downstream of many receptor tyrosine kinases (RTKs), including PDGFR, EGFR, and IGFR (Yeatman, 2004). Upon binding their respective ligands, these RTKs auto-phosphorylate on their C-terminal tyrosines which recruits Src via its phospho-tyrosine-binding SH2 domain. Now active, Src phosphorylates other proteins localized at the membranes to further amplify these growth signals. Members of canonical signaling pathways like the RAS-MAPK and PI3K-AKT are all regulated by Src or other SFK activity (Kim et al., 2009). Additionally, Src plays roles in the degradation of extracellular matrix through invadosome formation (Boateng and Huttenlocher, 2012) and regulates cell-cell adhesion through integrin signaling (Mitra and Schlaepfer, 2006). Unsurprisingly, given these cellular processes that are regulated by SFK signaling, much of the research effort surrounding Src focuses on its impact in cancer.

1.3 SRC'S ROLE IN CANCER

Src's roots in cancer biology can be traced back to its discovery in 1911, where the pathologist Francis Peyton Rous was studying sarcoma tumors in chickens. In a seminal experiment, Rous demonstrated that the cell-free filtrate from one chicken's tumor was able to cause cancer when injected into a new host (Weiss and Vogt, 2011). Thus, some subcellular, infectious agent was sufficient to cause disease, an observation that clashed with the dogma that cancer was entirely a disease arising from within a cell. Later on, this agent was identified as a virus, named Rous Sarcoma Virus (RSV) after it's discoverer.

RSV caused tumors in chickens and transformed fibroblasts grown in culture, but through what mechanism? Studies by Hidesaburo Hanafusa and others demonstrated that the oncogenic properties of RSV were not intrinsic to viral pathogenesis, as transformation-defective but replication-competent RSV mutants were isolated (Martin, 2001). Comparison of these strains indicated that the RSV strains capable of cellular transformation had more genetic material than those that couldn't, suggesting that a gene or genes were responsible for RSV's ability to cause cancer (Martin, 2001). Ultimately, this question was resolved when the v-src gene (in 1980 by Hanafusa) and its protein product (in 1977 by Joan Brugge) mapped and its role as the causative transforming factor was identified. Subsequent characterization determined that v-src's molecular function was a highly active tyrosine kinase (Hunter, 2015).

RSV, with its oncogenic v-src gene, clearly caused cancer in the animal systems used in the laboratory, but what was its relevance to human cancers? To explore this, Harold Varmus and Mark Bishop generated DNA probes that were complementary to v-Src and used these to search for similar genes in other organisms (Stehelin et al., 1976). Surprisingly, sequences homologous to v-Src were identified in non-RSV infected chicken cells. Moreover, this finding wasn't limited to avian cells, but these same probes identified Src homologs in all tested animal cell types, including human. These findings supported an intriguing hypothesis, that the v-src gene was not of viral origin, but was instead a co-opted and mutated form of a host's cellular gene! Thus, from Src came the paradigm-shifting concept of a proto-oncogene, a normal gene that, upon mutation, can cause cancer.

Decades of research have uncovered elevated Src activity across multiple cancer types, further cementing Src's credentials as a biomedically-important protein. However, somewhat surprisingly, Src itself is almost never mutated in cancers. Instead, the observed Src activation tends

to occur through mechanisms that preserve Src's sequence, including gene amplifications or mutations in negative Src regulators (Yeatman, 2004). These findings have resulted in many phase I/II clinical trials to target Src in cancer(Kim et al., 2009). However, despite these intense efforts, no Src inhibitors are currently approved as a cancer therapeutic.

1.4 SRC IS A MODEL FOR INTRAMOLECULAR REGULATION

Because of its established role in cancer, understanding the principles that regulate Src activity is of great interest. As noted previously, Src contains contains both a SH3 and SH2 domain upstream from its CD. Interestingly, these domains were first discovered in Src (named for **S**rc **H**omology) and are now appreciated as classic signaling domains. This SH3/SH2 domain module is responsible for the canonical mechanism of Src regulation. In a simplified view, we can think of Src as existing between two states: the "closed" or "open" forms (**Figure 1.1C)**. In the closed form, Src's SH2/SH3 domains are packed directly against its CD domain. This packing forces the SH2-CD linker into a position that prevents Src's αC-helix from forming a critical salt-bridge necessary for ATP binding. Thus, in this closed form, Src's catalytic activity is allosterically inhibited by interactions with its own SH3/SH2 domains. Conversely, in the open form, this intramolecular interaction is abolished and Src's CD can readily adopt a catalytically-competent active conformation.

What dictates the switch between closed and open forms? Although this regulatory mechanism is built directly into Src, these conformational shifts are canonically mediated by extrinsic factors. For example, the primary trigger for Src's closed form occurs through the actions of Csk, a kinase that phosphorylates a tyrosine on Src's C-terminal and thereby initiates the intramolecular recognition binding of Src's SH2 domain. Importantly, Src's SH3/SH2 domains have relatively poor affinity for their intramolecular substrates. Thus, when presented with higher affinity substrates (e.g. ligand-bound RTK), Src's SH3/SH2 domains can disengage from intramolecular interactions and bind to these better substrates, thereby activating the kinase. Coupling control of substrate recognition, localization, and activity all within the SH3/SH2 module elegantly ensures that Src will only be active in its proper cellular context.

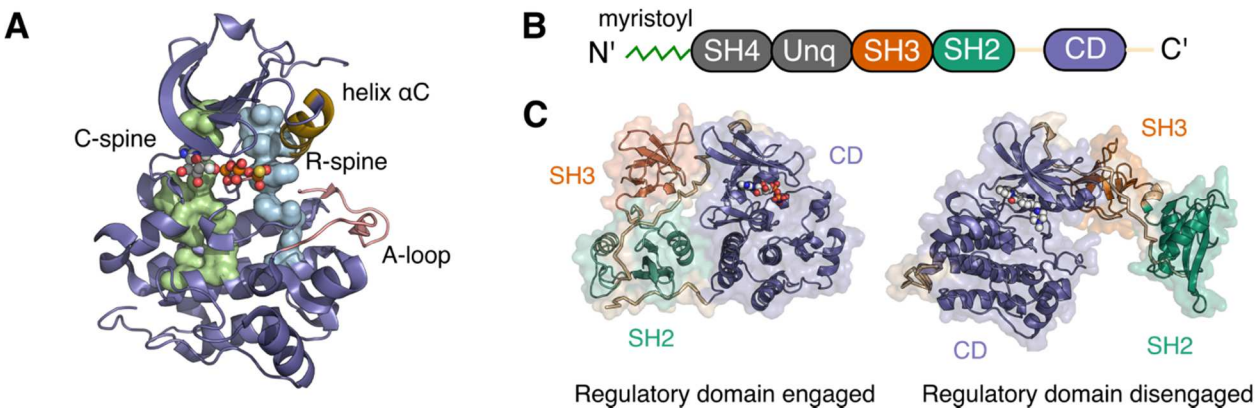

Figure 1.1. Domain architecture and structure of Src kinase.

A. Structural features of Src's catalytic domain (CD) (PDB: 3DQW), showing the C-spine (Catalytic, green), R-spine (Regulatory, blue), helix αC (yellow), and the A-loop (Activation, pink). **B.** Linear schematic of Src kinase (Unq, Unique domain). **C.** Src kinase in the closed, autoinhibited (left: PDB: 2SRC) and an open (right: PDB 1Y57(global conformation. The SH3 domain is shown in orange, the SH2 domain in green, and the CD in purple.

1.5 YEAST AS A MODEL TO STUDY SRC REGULATION

The complexities of Src-associated signaling networks and the functional redundancy of SFKs makes specifically studying Src biology a difficult task in mammalian cells. Some experimental systems to mitigate these issues exist, for example, the SYF cell line is a mouse fibroblast line with the major SFKs genetically deleted and is commonly used in Src studies (Klinghoffer et al., 1999). However, another popular model system to study Src is the in brewer's yeast, *Saccharomyces cerevisiae.* Initially, this may seem like an odd choice, because yeast (like other fungi) lack any dedicated tyrosine kinases encoded in their own genome. However, this provides an advantage in that all tyrosine phosphorylation detected in yeast must be due to the exogenously expressed Src, not from any native yeast kinases. Additionally, yeast lack any of the normal Src binding partners or effectors, meaning any phenotypes captured in yeast likely stem from Src-intrinsic mechanisms. Thus, *S. cerevisiae* provides a eukaryotic cellular environment without the complement of Src-specific regulators found in mammalian cells(Xu et al., 1999).

The final, and perhaps most powerful advantage to using yeast, is Src's effect on yeast growth. This phenotype was first characterized by Joan Brugge in 1984, who expressed Src in *S. cerevisiae* and observed that yeast expressing the kinase grew much slower than the control strain (Brugge et al., 1987). Importantly, this toxicity was dependent on the catalytic activity of Src (Florio

et al., 1994) and the effect on growth was proportional to the activity of the expressed Src mutant. Thus, yeast growth served as a simple proxy for Src kinase activity (and was a much more straightforward assay than traditional biochemical techniques). For decades, the mechanistic basis underlying Src-induced toxicity in yeast was unclear, but a recent study identified the spore wall remodeling kinase SMK1 as a target for the growth impairment caused by Src activity(Kritzer et al., 2018).

1.6 REFERENCES

Boateng, L.R., and Huttenlocher, A. (2012). Spatiotemporal regulation of Src and its substrates at invadosomes. Eur. J. Cell Biol. *91*, 878–888.

Brugge, J.S., Jarosik, G., Andersen, J., Queral-Lustig, A., Fedor-Chaiken, M., and Broach, J.R. (1987). Expression of Rous sarcoma virus transforming protein pp60v-src in Saccharomyces cerevisiae cells. Molecular and Cellular Biology *7*, 2180–2187.

Florio, M., Wilson, L.K., Trager, J.B., Thorner, J., and Martin, G.S. (1994). Aberrant protein phosphorylation at tyrosine is responsible for the growth-inhibitory action of pp60v-src expressed in the yeast Saccharomyces cerevisiae. Mol. Biol. Cell *5*, 283–296.

Hunter, T. (2015). Discovering the first tyrosine kinase. Proc. Natl. Acad. Sci. U.S.a. *112*, 7877–7882.

Kim, L.C., Song, L., and Haura, E.B. (2009). Src kinases as therapeutic targets for cancer. Nature Publishing Group *6*, 587–595.

Klinghoffer, R.A., Sachsenmaier, C., Cooper, J.A., and Soriano, P. (1999). Src family kinases are required for integrin but not PDGFR signal transduction. Embo J. *18*, 2459–2471.

Kritzer, J.A., Freyzon, Y., and Lindquist, S. (2018). Yeast can accommodate phosphotyrosine: v-Src toxicity in yeast arises from a single disrupted pathway. FEMS Yeast Research *18*, 355.

Lipsick, J. (2019). A History of Cancer Research: Tyrosine Kinases. Cold Spring Harb Perspect Biol *11*, a035592–20.

Martin, G.S. (2001). The hunting of the Src. Nat Rev Mol Cell Biol *2*, 467–475.

Mitra, S.K., and Schlaepfer, D.D. (2006). Integrin-regulated FAK-Src signaling in normal and cancer cells. Curr. Opin. Cell Biol. *18*, 516–523.

Roskoski, R. (2015). Src protein-tyrosine kinase structure, mechanism, and small molecule inhibitors. Pharmacological Research *94*, 9–25.

Stehelin, D., Varmus, H.E., Bishop, J.M., and Vogt, P.K. (1976). DNA related to the transforming gene(s) of avian sarcoma viruses is present in normal avian DNA. Nature *260*, 170–173.

Weiss, R.A., and Vogt, P.K. (2011). 100 years of Rous sarcoma virus. J. Exp. Med. *208*, 2351–2355.

Xu, Y., Singer, M.A., and Lindquist, S. (1999). Maturation of the tyrosine kinase c-src as a kinase and as a substrate depends on the molecular chaperone Hsp90. Proc Natl Acad Sci USA *96*, 109–114.

Yeatman, T.J. (2004). A renaissance for SRC. Nat Rev Cancer *4*, 470–480.

Chapter 2. A COMBINED APPROACH REVEALS A REGULATORY MECHANISM COUPLING SRC'S KINASE ACTIVITY, LOCALIZATION, AND PHOSPHOTRANSFERASE-INDEPENDENT FUNCTIONS.

This chapter has been adapted with only minor revisions from: **Ahler E***, Register AC*, Chakraborty S, Fang L, Dieter EM, *et al.* "A combined approach reveals a regulatory mechanism coupling Src's kinase activity, localization, and phosphotransferase-independent functions." Molecular Cell. April 2019. *denotes equal authorship. This project was only possible through the incredibly close collaboration with members of Dusty Maly's lab in the University of Washington's Chemistry department.

2.1 ABSTRACT

Multiple layers of regulation modulate the activity and localization of protein kinases. However, many details of kinase regulation remain incompletely understood. Here, we apply saturation mutagenesis and a chemical genetic method for allosterically modulating kinase global conformation to Src kinase, providing insight into known regulatory mechanisms and revealing a previously undiscovered interaction between Src's SH4 and catalytic domains. Abrogation of this interaction increased phosphotransferase activity, promoted membrane association and provoked phosphotransferase-independent alterations in cell morphology. Thus, Src's SH4 domain serves as an intramolecular regulator coupling catalytic activity, global conformation and localization, as well as mediating a phosphotransferase-independent function. Sequence conservation suggests that the SH4 domain regulatory interaction exists in other Src-family kinases. Our combined approach's ability to reveal a regulatory mechanism in one of the best-studied kinases suggests that it could be applied broadly to provide insight into kinase structure, regulation and function.

2.2 INTRODUCTION

Eukaryotic protein kinases (EPKs) comprise a family of ~540 enzymes in humans that are integral mediators of signal transduction (Taylor et al., 2012). Dysregulation of EPK activity is associated with numerous human diseases (Lahiry et al., 2010). Regulation of EPK phosphotransferase activity is varied and complex, encompassing catalytic domain (CD)-intrinsic mechanisms contained completely within the CD (**Figure 1.1A**), interdomain mechanisms between the CD and other regions of the kinase, and extrinsic mechanisms that provide context-dependent control. Interdomain regulation is pervasive: half of all EPKs contain at least one other protein domain (Manning et al., 2002). Although these domains often directly regulate CD activity, they can also have important phosphotransferase-independent functions (Kung and Jura, 2016).

One of the best-characterized families of multi-domain EPKs is the Src-family of kinases (SFKs). In addition to a C-terminal CD, SFKs contain a membrane-interacting SH4 domain, a Unique domain, and regulatory SH2 and SH3 domains (**Figure 1.1B**). Decades of research have elucidated the structure, mechanisms of regulation and biological functions of SFKs, with the roles of the SH2 and SH3 domains in regulating phosphotransferase activity best understood (**Figure 1.1C**) (Boggon and Eck, 2004). Despite this knowledge about SFKs in general and Src in particular, questions regarding regulation and phosphotransferase-independent functions remain. How do SFK domains coordinate to regulate CD activity? Do the less well understood SH4 and Unique domains play a role in directly regulating phosphotransferase activity? What are the phosphotransferase-independent roles of SFK regulatory domains? These questions are challenging to investigate—both for Src and for other multi-domain kinases—because of the dearth of tools for manipulating conformation, probing the importance of specific residues in regulating phosphotransferase activity and investigating phosphotransferase-independent functions.

To answer these questions, we combined CystIMATIK, a chemical genetic method for controlling kinase conformation, with comprehensive mutagenesis of Src's CD (**Figure 2.1A-B**). This integrated approach revealed details of well-studied Src domains and uncovered an interaction between Src's SH4 domain and a pocket in the C-lobe of Src's CD with no previously known function. Abrogation of this SH4 domain/CD interaction increased phosphotransferase activity, disengaged the SH2 and SH3 regulatory domains, and increased association with membranes. Moreover, exposure of Src's SH4 domain mediated phosphotransferase-independent alterations in cell morphology. Thus, Src's SH4 domain serves as an intramolecular regulator coupling catalytic

activity, global conformation and localization, and also mediating a phosphotransferase-independent cellular function. Analysis of SFK residue conservation in the light of comprehensive mutagenesis data, combined with additional biochemical experiments, strongly suggests that the SH4 regulatory interaction is conserved amongst SFKs.

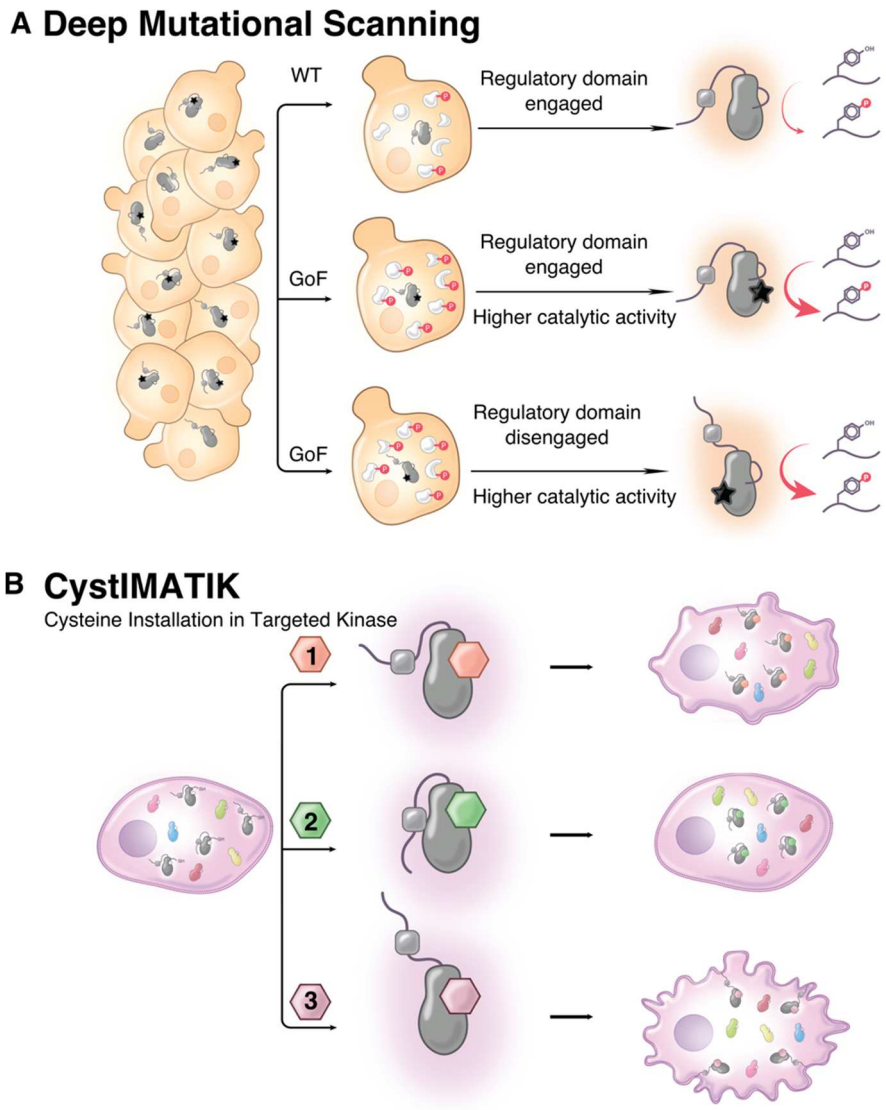

Figure 2.1. Schematics of Deep Mutational Scanning and CystIMATIK.

A. Deep mutational scanning for the simultaneous measurement of the activity of nearly all possible single mutants of a kinase. **B.** Cysteine installation for modulating allostery and targeted inhibition of kinases (CystIMATIK), a method for selectively modulating intramolecular regulatory domain interactions and global conformation of a drug-sensitized kinase with conformation-selective, ATP-competitive probes.

2.3 RESULTS

Parallel measurement of the activity of 3,506 Src mutants

To identify residues important for regulating Src's activity, we used deep mutational scanning (DMS) (Fowler and Fields, 2014; Fowler et al., 2010), adapting an assay based on *S. cerevisiae* growth (**Figure 2.2A**) (Kritzer et al., 2018). Yeast provides a eukaryotic cellular environment to probe intrinsic regulation in the absence of extrinsic regulatory factors, with growth rates correlating to overall levels of cellular phospho-tyrosine (**Figure 2.2B-C**). We mutagenized the CD of full-length Src (Src^{myr}, refer to **Figure 2.3A** and for all constructs), transformed this library into yeast, collected samples during outgrowth and deeply sequenced each sample to quantify the frequency of all variants at every time point (**Figure 2.2A**, **Figure 2.3B**). Then, we calculated activity scores for all 3,506 single amino acid variants in our library (**Figure 2.2D**, **Figure 2.3C**, **Table S2**) (Rubin et al., 2017); classified each variant as either gain-of-function, loss-of-function, or WT-like (**Figure 2.2E**); and organized our large-scale Src variant activity scores into a sequence-function map covering ~70% of possible CD single mutants (**Figure 2.2F**). The map revealed expected patterns (**Figure 2.3C-D**) and identified 46 essential residues where >90% of mutations resulted in loss-of-function. Finally, individually-determined growth rates were negatively correlated with large-scale variant activity scores (**Figure 2.2G**), and the activity scores accurately reflected yeast and human cellular phospho-tyrosine levels (**Figure 2.2H-I**, **Figure 2.3E-F**).

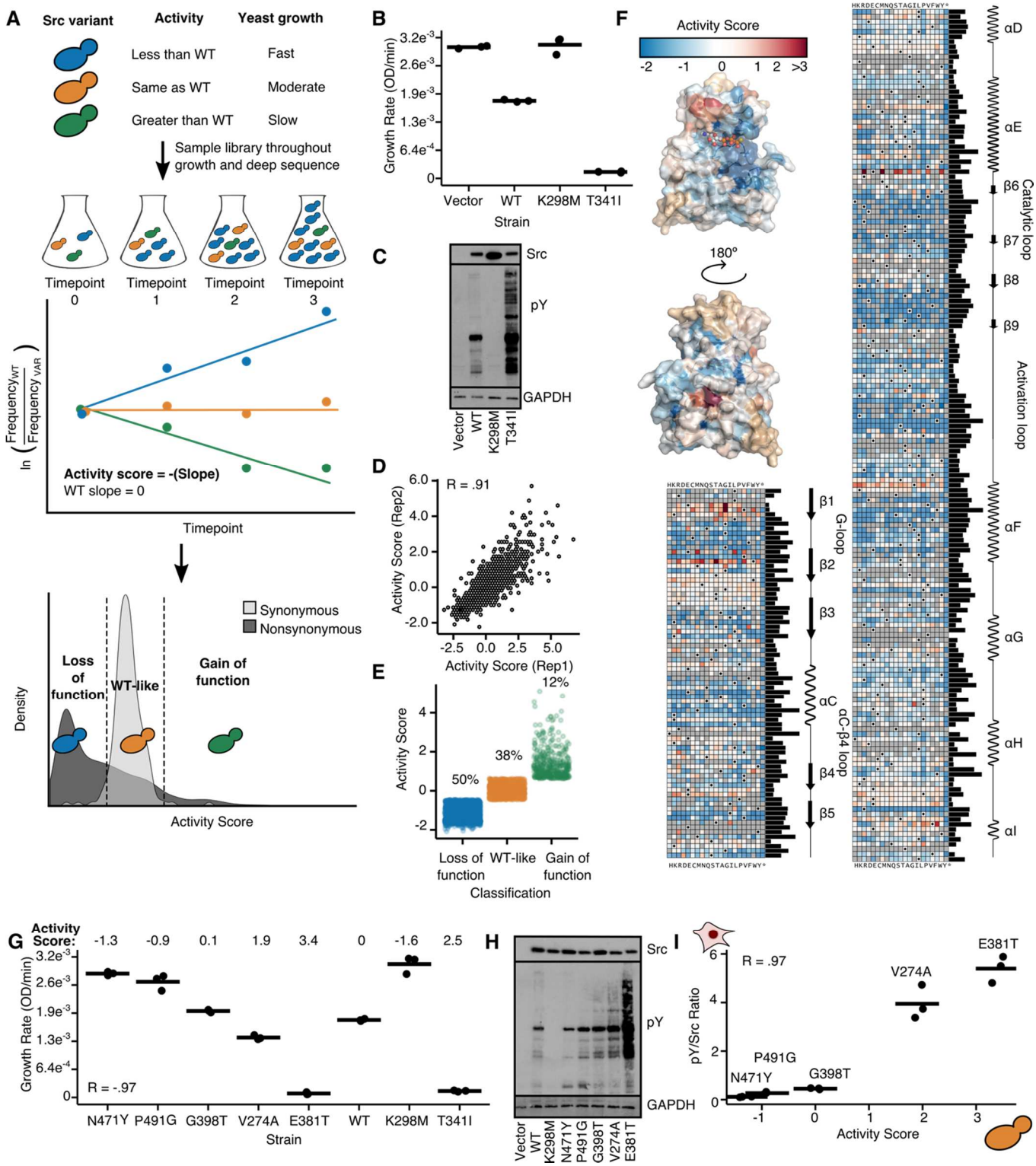

Figure 2.2. Multiplex measurement of the activity of 3,506 single amino acid Src variants.

A. Schematic of a yeast growth-based deep mutational scan (DMS) of the Src catalytic domain. **B.** Individually-assessed growth curves for yeast expressing Src^{myr} WT, K298M, T341I, or a control vector (n=3). **C.** Src and phospho-tyrosine (pTyr) immunoblots of yeast expressing Src^{myr} variants

for 24 hr. **D.** Scatterplot showing activity score correlations between two independent transformations of the Src^{myr} variant library (Pearson's R = 0.91). **E.** Activity scores for variants classified as gain-of-function (n=403, green), WT-like (n=1288, orange), or loss-of-function (n=1681, blue). **F.** Position-averaged activity scores mapped onto the Src catalytic domain (PDB: 3DQW). Nonsense mutants were excluded from the average score. Sequence-activity map of Src catalytic domain. Black dots in the map indicate the WT amino acid, gray tiles indicate missing data. Bar graph indicates relative evolutionary conservation at each position as determined by Kullback-Leibler entropy. Secondary structure and functional motif annotations were obtained from the ProKinO database. **G.** Dot plot of individually assessed growth rates compared to activity scores for a panel of Src^{myr} variants (n=3; Pearson's R = -.97). Growth rates for WT, K298M, and T341I from are shown for comparison. **H.** Src and phospho-tyrosine immunoblots of yeast expressing Src^{myr} variants. **I.** Correlation between yeast DMS-derived activity scores and the ratio of phospho-tyrosine/Src levels in HEK293Ts for a panel of Src^{myr} variants (n=3; Pearson's R = 0.97). Points represent individual measurements and the horizontal lines indicate the mean of all measurements.

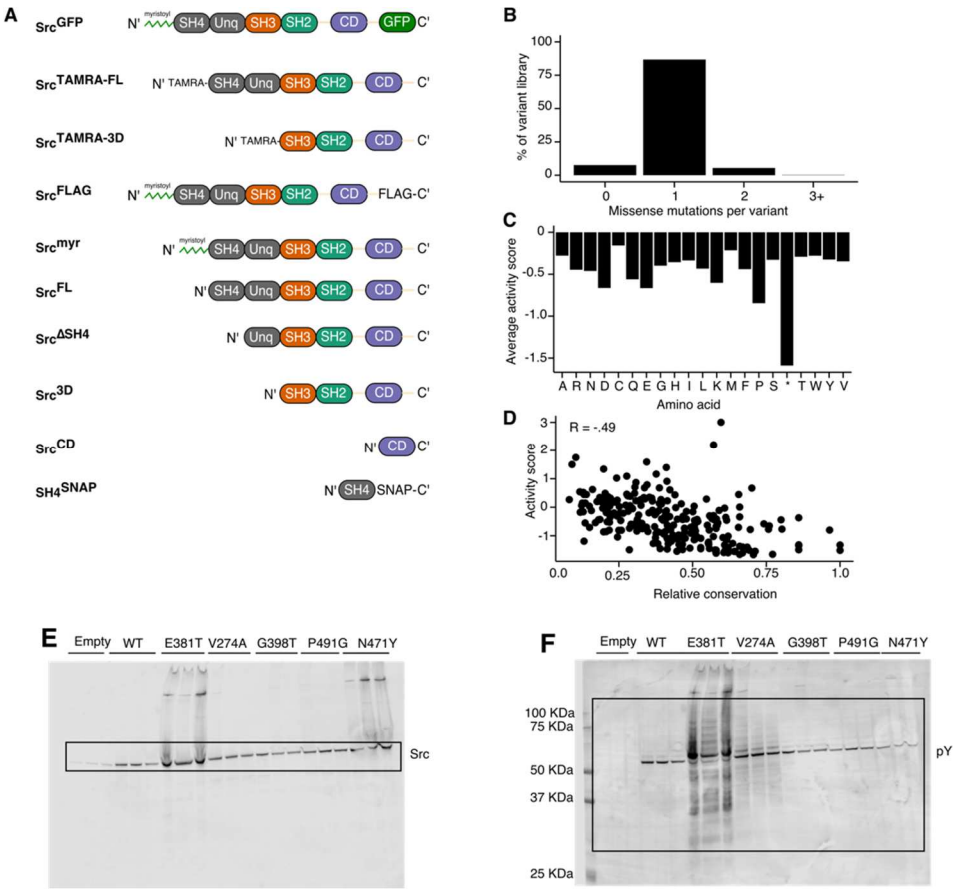

Figure 2.3. Deep mutational scan of Src's CD.

A. Schematic of all Src constructs used in this manuscript. Src^{GFP} (Expressed in mammalian cells: Src residues 1-536 with an 8 amino acid C-terminal linker fused to GFP. Src^{FLAG} (Expressed in mammalian cells: Src residues 1-536 fused directly to a C-terminal FLAG tag. Src^{myr} (Expressed in mammalian cells and *S. cerevisiae*: Src residues 1-536. Src^{FL} (Expressed in *E. coli*: Src residues 1-536. Src^{3D} (Expressed in *E. coli* and *S. cerevisiae*: Src residues 87-536. Src$^{\Delta SH4}$ (Expressed in *E. coli* and *S. cerevisiae*: Src residues 19-536. Src^{CD} (Expressed in *E.*: Src residues 261-536. Src$^{TAMRA-FL}$ (Expressed in *E. coli*): Src residues 2-

536 with an N-terminal TAMRA label. $Src^{TAMRA\text{-}3D}$ (Expressed in *E. coli*: Src residues 87-536 with an N-terminal TAMRA label. $SH4^{SNAP}$ (Expressed in *E. coli*: Src residues 1-18 fused to the N-terminus of SNAP-tag with a short LPETGG linker in between SH4 and SNAP. **B.** Bar graph of percentage of library members that are WT or have one, two, or three or more amino acid mutations. **C.** Bar graph of average activity score of Src library grouped by mutant amino acid identity. **D.** Scatter plot comparing evolutionary conservation with average activity score at each residue (Pearson's R = -.49). **E.** Representative total Src immunoblot for Src^{myr} WT, Src^{myr} E381T, Src^{myr} V274A, Src^{myr} G398T, Src^{myr} P491G, and Src^{myr} N471Y transiently expressed in HEK293T cells for 24 hr**.** Representative total phospho-tyrosine immunoblot for Src^{myr} WT, Src^{myr} E381T, Src^{myr} V274A, Src^{myr} G398T, Src^{myr} P491G, and Src^{myr} N471Y transiently expressed in HEK293T cells for 24 hr.

Residue-scale mapping of Src regulatory interactions

Our large-scale mutagenesis data provide the first comprehensive functional view of Src intramolecular regulation at residue-scale resolution. We reasoned that residues in the CD that participate in autoinhibitory interactions would contain multiple gain-of-function mutations. To identify surfaces important for autoinhibition, we clustered the 27 residues in Src's CD that had at least five gain-of-function mutations based on spatial proximity. Seven clusters of residues emerged, distributed across both lobes of the CD (**Figure 2.4A**).

Two gain-of-function clusters, 4 and 7, coincided with autoinhibitory interactions between Src's CD and its SH2 and SH3 domains. Autoinhibited Src adopts a closed global conformation, with the SH2 and SH3 domains forming an extensive interaction interface with the CD (**Figure 2.4C,** (Xu et al., 1997)). While the importance of the interaction between Src's phosphorylated C-terminal tail and the SH2 domain in stabilizing the closed, autoinhibited global conformation is well understood (Young et al., 2001), the contributions of specific residues lining the SH2 domain/CD interface have not been determined. Thus, we mapped gain-of-function cluster 4 onto the CD's SH2 domain interface (SH2-CD; **Figure 2.4B**, **top**). Every substitution at position D368 was activating, suggesting that D368's interaction with R159 (**Figure 2.5A**) in the SH2 domain is important for stabilizing the closed, autoinhibited conformation. We purified a non-phosphorylated, full-length Src construct lacking an N-terminal myristoyl group (Src^{FL}), measured phosphotransferase activity (**Figure 2.4C**, **Figure 2.5B**) and assessed intramolecular regulatory domain engagement using an immobilized SH3 domain ligand pulldown (**Figure 2.4D**)**.** Consistent with D368K leading to increased activity by disrupting Src's intramolecular autoinhibition, Src^{FL} D368K's association with an immobilized SH3 ligand was increased ~10-fold relative to Src^{FL} WT (**Figure 2.4E**, **Figure 2.5C**). Therefore, the D368–K159 salt bridge is critical for stabilizing the closed, autoinhibited global conformation of Src, with other interface interactions making minimal contributions.

In autoinhibited Src, the SH3 domain binds to a surface composed of the CD's N-terminal lobe and the linker connecting the CD to the SH2 domain (SH3/Linker-CD; **Figure 2.4B**, **middle**). Mutations that disrupt interactions between the SH3 domain, CD, and SH2-linker hyperactivate SFKs (Gonfloni et al., 1997; LaFevre-Bernt et al., 1998). We found that many of the residues lining the SH3 domain/CD/SH2-linker interface, which contains cluster 7, have gain-of-function mutations. Thus, unlike the SH2 domain/CD interface, the SH3 domain/CD/SH2-linker interface is much less tolerant of substitutions. Src^{FL} T293D, a gain-of-function mutant in this interface, had increased phosphotransferase activity and association with the immobilized SH3 domain ligand (**Figure 2.4C**,**E**). Our data support the canonical model of Src autoinhibition: the SH3 domain acts as a clamp that forms broadly distributed interactions with the SH2-linker and the CD, and the SH2 domain serves as a latch that stabilizes a closed global conformation (Xu et al., 1999).

Two of the largest gain-of-function clusters we identified do not overlap known intramolecular regulatory interfaces. The largest, cluster 2, is located at the intersection of the αF/αE/αI helices in the C-terminal lobe of Src's CD and contains five of the fifteen most activating mutations (**Figure 2.4B**, **bottom**). This region, to the best of our knowledge, is not known to participate in regulatory interactions in any tyrosine kinase. However, surface geometry comparison analysis suggested that this region comprises an orphan binding pocket, called the "αF pocket", for many kinases (Thompson et al., 2009). The αF pocket is highly conserved across SFKs (**Figure 2.4F**). Interestingly, two αF pocket Src mutants can transform cells (Levy et al., 1986) via an unknown mechanism (Bjorge et al., 1995; Seidel-Dugan et al., 1992).

Based on its large 1,361 $Å^2$ surface area and the number of gain-of-function mutations, we hypothesized that the αF pocket serves as an intramolecular regulatory surface that stabilizes Src's closed, autoinhibited global conformation. To test this hypothesis, we characterized the Src^{FL} αF pocket mutants E381T and I444K. *In vitro*, both mutants showed ~10-fold increases in k_{cat} but little difference in K_m for ATP relative to Src^{FL} WT (**Figure 2.4C**, **Figure 2.5B**). Expression of Src^{myr} E381T led to high levels of cellular phospho-tyrosine compared to WT in multiple mammalian cells lines (**Figure 2.4I**, **Figure 2.5D**-**E**). Next, we examined the subcellular localization of GFP C-terminal fusions of Src in Src/Yes/Fyn (-/-/-) fibroblasts (SYFs) (Klinghoffer et al., 1999). Src^{GFP} E381T displayed enhanced localization to late endosomes and the perinuclear region compared to Src^{GFP} WT (**Figure 2.4G**, **S2F**). In addition, it promoted non-apoptotic membrane blebbing (**Figure 2.4G**), a phenotype consistent with localized disruption of the actin-myosin cortex (Charras, 2008). To the best of our knowledge, this blebbing phenotype has not previously been observed with any

other hyperactive Src variants. Thus, we were curious whether blebbing derived from the E381T mutant's increased phosphotransferase activity or through a phosphotransferase-independent mechanism such as exposure of an otherwise intramolecularly sequestered binding surface.

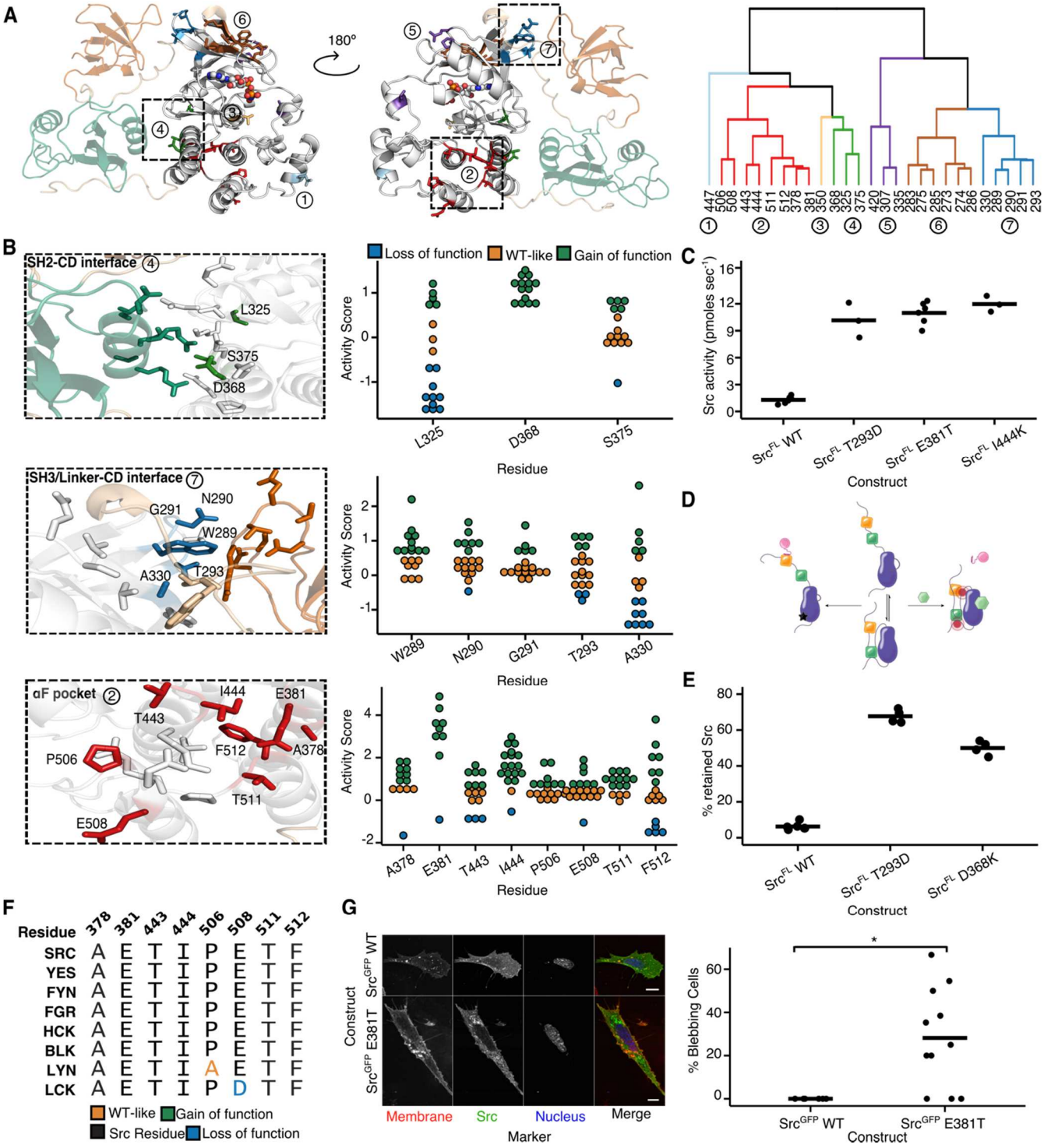

Figure 2.4. Large-scale mutagenesis data reveal Src's regulatory interfaces.

A. Hierarchical clustering of Src residues with at least five gain-of-function mutations based on spatial coordinates of the atomic centroids of each sidechain (*right panel*) projected onto the Src structure (*left panel*, PDB: 2SRC). **B**. Structural detail (*left panels*) and activity scores (*right panels*) for every variant at each residue comprising clusters that overlap with the SH2-CD (cluster 4, *top*), SH3/Linker-CD (cluster 7, *middle*) and αF pocket (cluster 2, *bottom*) interfaces (PDB: 2SRC). In the left panels, CD residues that are not part of a cluster are shown in white, SH2-linker residues in tan, SH2 residues in green, and SH3 residues in orange. **C**. Phosphotransferase activity of purified Src^{FL} WT, T293D, E381T, or I444K (n=3-6). **D**. Schematic of the SH3 pulldown assay. To detect global conformation, Src is incubated with an immobilized SH3 domain ligand. Closed, SH3-engaged Src is unable to bind to the resin, whereas open, SH3-disengaged Src binds. After washing, retained Src is eluted and quantified by western blot or in-gel fluorescence. **E**. Percent retained Src in the SH3 pulldown assay with purified Src^{FL} WT, T293D, or D368K (n=3-6). **F**. Sequence alignment of Src-family kinase αF pocket residues. **G**. Representative micrographs (*left*) and percent bleb quantification (*right*) for SYFs expressing either Src^{GFP} WT or Src^{GFP} E381T. Scale bars = 10 μm. Each point represents a replicate transfection with multiple cells imaged and scored in a double-blind fashion. Horizontal lines indicate the mean of all replicates. *p <0.05.

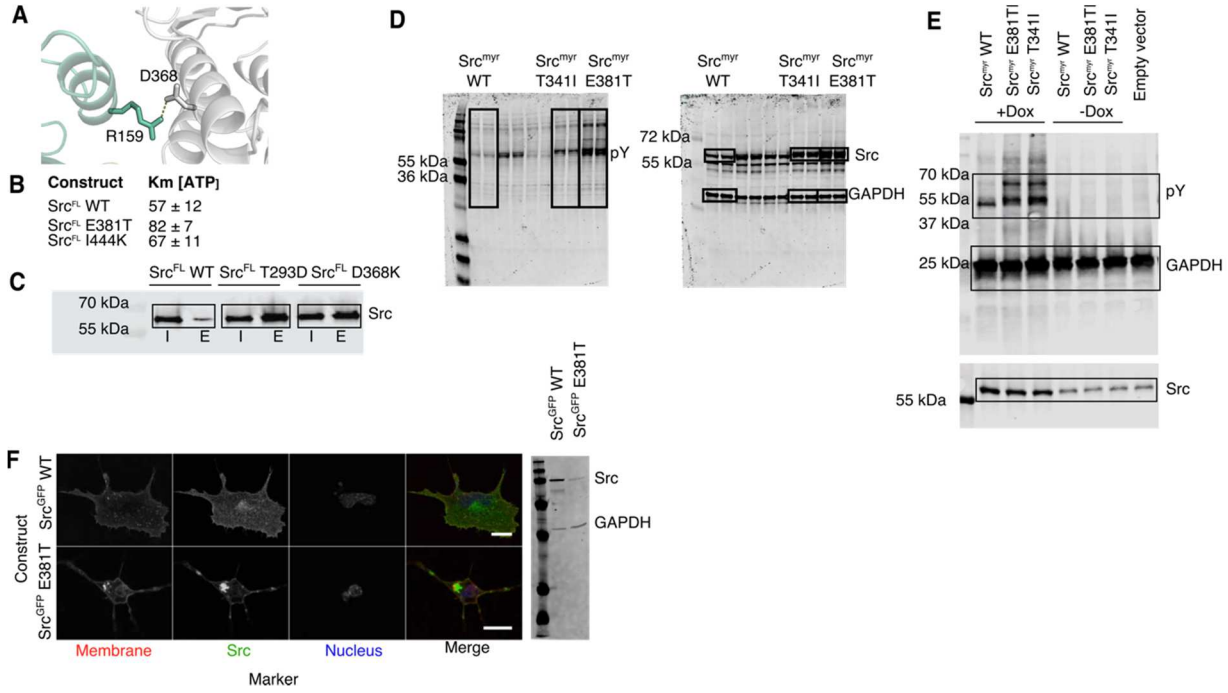

Figure 2.5. Interrogation of Src's intramolecular regulatory surfaces.
A. Salt bridge formed between R159 (*green*) and D368 (*white*) in Src's closed conformation, PDB:2SRC. Measured ATP Michaelis-Menten constants (K*m* [ATP]) for Src^{FL} WT, Src^{FL} E381T, and Src^{FL} I444K (n=3, mean ± s.e.m). **C**. Total Src immunoblots for SH3 domain pulldown assays performed with Src^{FL} WT, Src^{FL} T293D, and Src^{FL} D368K (I = input Src construct; E = Src construct retained after SH3 pulldown). Retained Src was quantified by fitting the immunoblot signal intensity to a Src titration standard curve. **D.** Immunoblots showing phospho-tyrosine (pY, (*left panel*)), total Src (*right panel*) and GAPDH of Src^{myr} WT, Src^{myr} T341I and Src^{myr} E381T transiently expressed in SYFs. E. Immunoblots showing phospho-tyrosine (pTyr), GAPDH and total Src of transiently expressed Src^{myr} WT, Src^{myr} E381T, or Src^{myr} T341I in HeLa cells under a doxycycline (Dox) inducible promoter. **F.** Representative micrographs comparing the localization of Src^{GFP} WT

with Src^{GFP} E381T in SYFs (*left*). Total Src and GAPDH immunoblot of SYFs transiently expressing Src^{GFP} WT or Src^{GFP} E381T (same day transfection for both) (*right*).

Chemical genetic control of kinase global conformation

Many protein kinases, including SFKs, possess phosphotransferase–independent cellular roles (Kung and Jura, 2016). Determining whether a phenotypic effect, like the one we observed for Src E381T, is caused by changes in phosphotransferase activity or via a phosphotransferase-independent mechanism is challenging as options for decoupling conformational state from activity are limited. Kinase inhibitors can modulate intramolecular regulatory domain interactions and global conformation by stabilizing different ATP-binding site conformations. For example, stabilization of SFKs in the helix αC-out conformation with inhibitors promotes a closed global conformation and reduces engagement of intermolecular binding partners (Krishnamurty et al., 2012; Leonard et al., 2014). Conversely, stabilization of an inactive conformation of the Asp/Phe/Gly (DFG)-motif at the base of the activation loop promotes an open global conformation (Skora et al., 2013). Thus, conformation-selective inhibitors that modulate SFK global conformation while simultaneously blocking phosphotransferase activity could be used to investigate phosphotransferase-independent phenotypic effects. However, this strategy requires a set of inhibitors selective for distinct conformations, each with specificity sufficient to ascribe observed phenotypes to modulation of the conformation of the targeted SFK.

To address this shortcoming, we developed Cysteine Installation for Modulating Allostery and Targeted Inhibition of Kinases (CystIMATIK). CystIMATIK is based on the introduction of a functionally neutral cysteine mutation into the active site of a target kinase, sensitizing it to a set of electrophile-containing CystIMATIK probes that stabilize different ATP-binding site conformations. Only the mutant kinase is sensitive to the CystIMATIK probes, which should not bind to other kinases or the WT targeted kinase. As a starting point for our probes, we used **1**, a derivative of an inhibitor that only binds to the ATP-binding sites of kinases that contain both a Cys residue on the β2 strand of the N-terminal lobe and a Thr residue at the gatekeeper position (V284 and T341 in Src, respectively, (**Figure 2.6A**-**B** (Serafimova et al., 2012))**.** As expected, we found that WT Src and Hck, another SFK, are insensitive to **1**, but that V284C variants are potently inhibited (**Figure 2.6C**, **Figure 2.7A**).

CystIMATIK probe **1** contains a substituent at the C-5 position of the pyrrolopyrimidine scaffold that should not affect the conformation of SFK ATP-binding sites, thus minimally perturbing global conformation. To generate conformation-selective versions of **1**, we introduced

substituents at the C-5 position to stabilize the helix αC-out (**2**) or DFG-out conformations (**3**). Like **1**, probes **2** and **3** potently inhibited V284C mutants of Src and Hck but showed minimal inhibition of WT SFKs (**Figure 2.6C**). Crystal structures of **1**-**3** bound to Src^{CD} V284C confirmed that each probe stabilizes the expected ATP-binding site conformation (**Figure 2.6D**). Thus, CystIMATIK probes that stabilize desired ATP-binding site conformations can be generated by varying the pyrrolopyrimidine scaffold's C-5 substituent.

Next, we performed SH3 domain pulldown assays with CystIMATIK probe-SFK complexes to determine whether each probe promotes the expected SFK global conformation (**Figure 2.6E**) (Krishnamurty et al., 2012; Leonard et al., 2014). Helix αC-out-stabilizing inhibitor **2** led to minimal pulldown of Src^{FLAG} V284C, consistent with **2** stabilizing a closed global conformation. Conversely, the DFG-out-stabilizing inhibitor **3** greatly increased SH3 domain-accessible Src^{FLAG} V284C. **1**, which minimally perturbs global conformation, yielded an intermediate level of SH3 domain accessibility. The same trend was observed with Hck^{FLAG} V284C in **1**-**3**-treated cells (**Figure 2.7B**) and with purified Src lacking the SH4 and Unique domains (Src^{3D} V284C) (**Figure 2.7C**). Furthermore, we found that the C-terminal tails of **2**- and **3**-bound Src^{3D} V284C and Hck^{3D} V284C demonstrated expected levels of accessibility to phosphorylation by C-terminal Src kinase (Csk; **Figure 2.6F**-**G**, **Figure 2.7D-F** (Leonard et al., 2014)). Thus, CystIMATIK probes affect intramolecular engagement of SFK SH2 and SH3 domains and, consequently, global conformation as predicted based on the ATP-binding site conformations they stabilize.

To assess the specificity of our CystIMATIK probes, we performed comprehensive kinase profiling assays (Golkowski et al., 2017). Lysates from SILAC-labeled HEK293T cells, engineered to stably express Hck^{FLAG} V284C along with low levels of endogenous WT Hck, were incubated with 10 μM **1**, **2**, **3**, or DMSO, and an immobilized matrix of non-selective inhibitors. Mass spectrometric determination of kinase enrichment in the presence of each CystIMATIK probe relative to DMSO allowed us to assess probe-kinase binding (**Figure 2.7G**). Hck^{FLAG} V284C was the only kinase among the ~220 enriched that was depleted in the presence of inhibitors **1** and **2**. Inhibitor **3** was slightly less selective for Hck^{FLAG} V284C, with EPHA2 also showing significant depletion (**Figure 2.6H**, **Figure 2.7H**). Therefore, CystIMATIK probes enable precise control of CD conformation in a highly selective manner, allowing us to decouple Src's phosphotransferase activity from its global conformation.

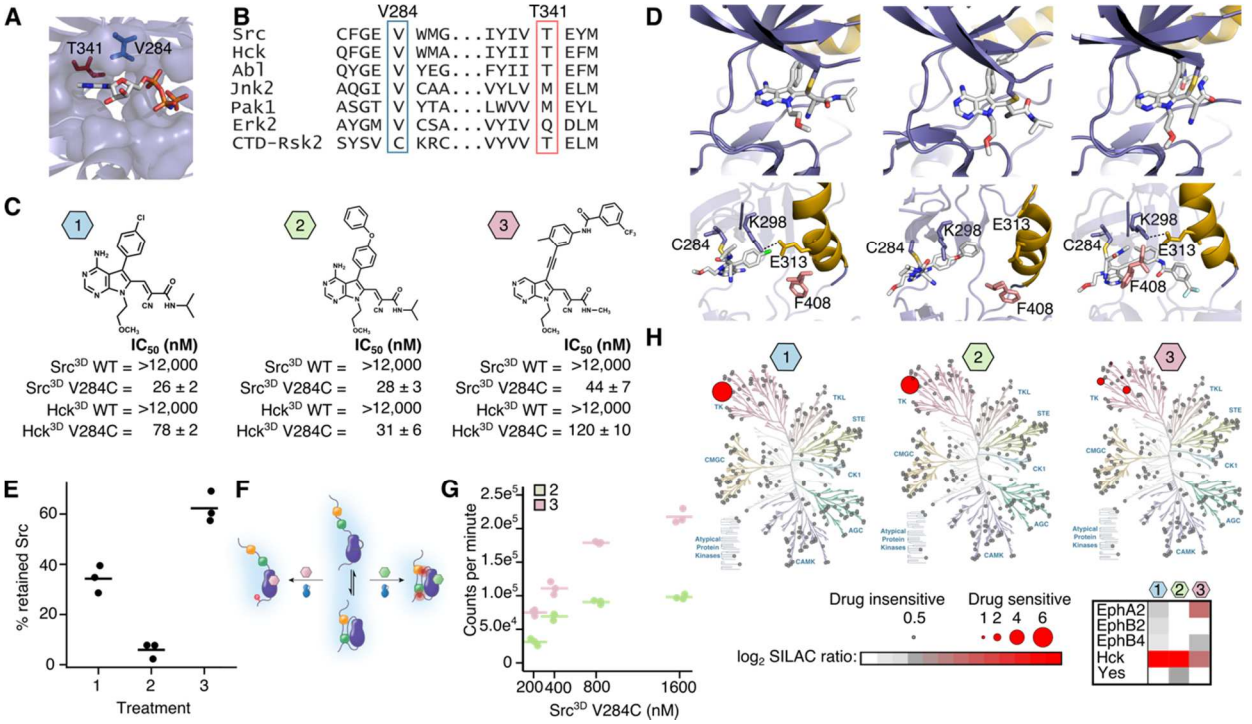

Figure 2.6. Cysteine Installation for Modulating Allostery and Targeted Inhibition of Kinases (CystIMATIK).

A. Structure of the CD of Src (PDB: 2SRC) bound to AMP-PNP. Positions that are important for sensitivity to CystIMATIK probes are shown as sticks (T341 (*red*) and V284 (*blue*)). **B**. Sequence alignment of Src and Hck with various kinases and the C-terminal kinase domain of p90 ribosomal protein S6 kinase, CTD-RSK2. **C**. CystIMATIK probes 1-3. IC_{50} values (n=3, mean ± s.e.m), determined in the presence of 1 mM ATP, for Src^{3D} WT, Src^{3D} V284C, Hck^{3D} WT, and Hck^{3D} V284C are shown below each probe. Hck is numbered according to analogous Src residue. **D**. Crystal structures of the Src^{CD} V284C-1 (*left*; PDB:5SWH), Src^{CD} V284C-2 (*middle*; PDB:5TEH) and Src^{CD} V284C-3 (*right*; PDB:5SYS) complexes. Top panels: 1-3 are shown as sticks colored by atom. Bottom panels: Helix αC (*yellow*) and the Phe (*pink*) of the DFG motif are shown. C284, K298, and E313 are depicted as sticks. **E**. Percent retained Src in the SH3 pulldown assay for Src^{FLAG} V284C-expressing HEK293s treated with CystIMATIK probe 1, 2, or 3 (n=3). **F**. SH2 domain accessibility assay using Csk. Src^{3D} V284C-CystIMATIK probe complexes are incubated with Csk and γ^{32}P-ATP, and radioactive phosphate transfer to Src^{3D} V284C is quantified. Closed, SH2-engaged Src cannot be phosphorylated by Csk whereas open, SH2-disengaged Src is efficiently phosphorylated by Csk. **G**. Quantification of Csk's phosphorylation of the Src^{3D} V284C-2 and Src^{3D} V284C-3 complexes. **H**. Kinome profiling of CystIMATIK probes 1-3. Profiled kinases are represented by grey circles and interacting kinases by red circles. For interacting kinases, circle size scales with log2 SILAC ratio of DMSO control over 10 μM of each CystIMATIK probe (a mean log2 SILAC ratio >1 cut-off was applied; n=3). The heatmap shows all kinase targets for each CystIIMATIK probe. For 2.6E and 2.6G, points represent individual measurements and the horizontal lines indicate the mean of all measurements.

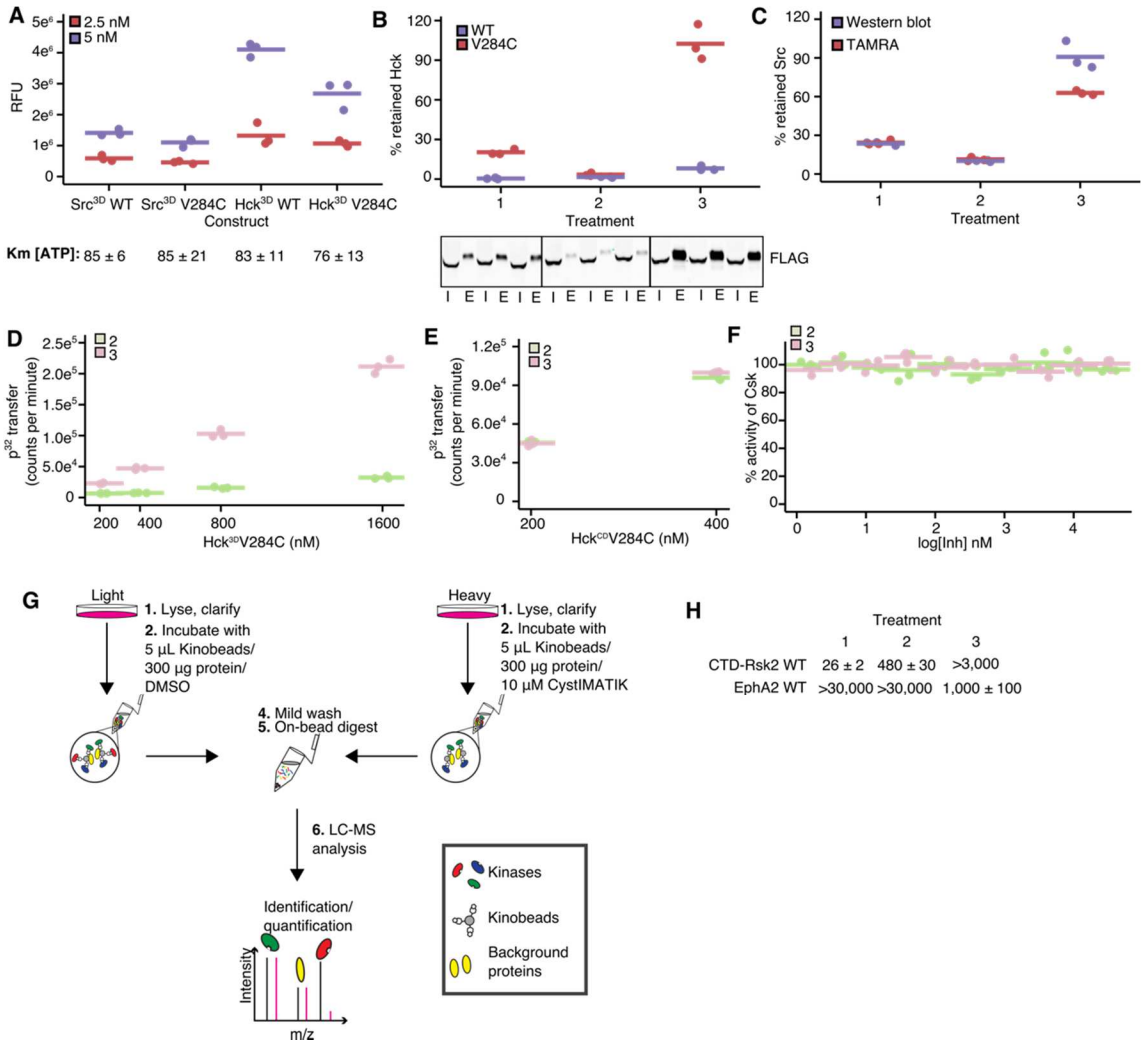

Figure 2.7. Development and characterization of CystIMATIK.
A. Comparison of the catalytic activities (*top*) and K*m* [ATP]s (*bottom*) for Src^{3D} WT and Src^{3D} V284C or Hck^{3D} WT and Hck^{3D} V284C (n=3). Catalytic activity was measured at either 2.5 nM (*red*) or 5 nM (*purple*) SFK^{3D} concentration (n=3). For catalytic activity comparisons, each SFK^{3D} was incubated with 20 µM of a self-reporting fluorescence SFK peptide (EEEIYGE-(DAP-Pyrene)-EA) and 1 mM ATP and relative fluorescence units (RFU) was measured after 60 min. **B**. Quantification of percent retained Hck in the SH3 pulldown assay for HEK293Ts expressing Hck^{FLAG} V284C (*red*) (human Src numbering) or Hck^{FLAG} WT (*purple*) and treated with 10 µM 1, 2, or 3 (n=3). Hck was quantified with an anti-FLAG antibody. A representative FLAG immunoblot for HEK293Ts expressing Hck^{FLAG} V284C and treated with 1, 2, or 3 is shown (I = input Hck^{FLAG} V284C; E = Hck^{FLAG} V284C retained after SH3 pulldown). **C**. Quantification of SH3 pulldown for purified Src^{3D} V284C (*purple*) or tetramethylrhodamine-labeled Src$^{TAMRA-3D}$ V284C (*red*) complexed to inhibitors 1, 2, or 3 (n=3). Retained Src was quantified by fitting the immunoblot signal intensity to a Src (using an anti-Src antibody) titration standard curve. **D**. SH2 domain accessibility assay of the Hck^{3D} V284C-2 (*green*) and Hck^{3D} V284C-3 (*pink*) complexes (n=3). Various concentrations of Hck^{3D} V284C-2 and Hck^{3D} V284C-3 were incubated with Csk (25 nM) and 0.4 µCi/mL γ^{32}P-ATP for 60 min. γ^{32}P transfer on Y530 (Src numbering) of Hck^{3D} V284C by Csk is represented as individual measurements and the horizontal lines indicate the mean of all measurements. **E**. SH2 domain

accessibility assay of 200 or 400 nM Hck^{CD} V284C-2 (*green*) and Hck^{CD} V284C-3 (*pink*) complexes (n=3) in the presence of Csk (25 nM) and 0.4 μCi/mL γ^{32}P-ATP. γ^{32}P transfer on Y530 (Src numbering) of Hck^{CD} V284C by Csk is represented as individual measurements and the horizontal lines indicate the mean of all measurements. **F**. Activity assay of Csk and an exogenous peptide substrate (Csktide, KKKKEEIYFFFG) in the presence CystIMATIK probes 2 (*green*) or 3 (*pink*) at the concentrations shown (n=3). **G**. Schematic for Kinobead profiling. Hck^{FLAG} V284C-expressing HEK293 cells were grown for at least 5 cell doublings in SILAC medium and then lysed and clarified. Lysates were then incubated with a kinobead matrix and DMSO (*left*) or 10 μM CystIMATIK probes 1, 2, or 3 (*right*). After mild washing, kinobead matrices (*left* and *right*) were combined, subjected to on-bead digestion, and relative kinase enrichment quantified by LC-MS. **H**. IC_{50} values of CystIMATIK probes 1-3 for WT off-target kinases. Probe 1 is a close structural analog of a selective inhibitor of the C-terminal catalytic domain of the p90 ribosomal protein S6 kinase Rsk2 (CTD-Rsk2; (Serafimova et al., 2012)). The CTD of Rsk2 contains a Cys residue at the position analogous to Val284 in Src and a Thr gatekeeper residue but Rsk2 was not one of the ~220 enriched kinases in our kinobead profiling experiment. Therefore, the IC_{50} values of CystIMATIK probes 1-3 for CTD-Rsk2 (substrate used: CTDide, sequence RRQLFRGFSFVAK) were also determined. We also determined the IC_{50} values of 1-3 for WT EphA2. IC_{50} value determinations for both kinases were performed in the presence of 0.08 μCi/mL γ^{32}P-ATP. (n=3, mean ± s.e.m.) Points represent individual measurements and the horizontal lines indicate the mean of all measurements.

Phenotypic effects of conformation-selective Src inhibition

We next used CystIMATIK to modulate Src's global conformation in the absence of phosphotransferase activity. If Src E381T's increased phosphotransferase activity drives the blebbing we observed (**Figure 2.4G**), all three CystIMATIK probes should abolish the effect. Conversely, if blebbing is a phosphotransferase-independent consequence of E381T exposing an otherwise intramolecularly sequestered binding surface, treatment with CystIMATIK probes **3** and, to a lesser extent, **1**, should result in blebbing. Expression of Src^{GFP} V284C or Src^{GFP} WT in SYFs yielded a small number of blebbing cells, which was minimally affected by treatment with probe **2** (**Figure 2.8A**, **Figure 2.9A-B**). However, treatment of Src^{GFP} V284C-expressing SYFs with probe **3** resulted in rapid (**Figure 2.8B**, **Figure 2.9C**) and dose-dependent (**Figure 2.8C**) induction of blebbing. Blebbing appears to be a direct consequence of modulation of Src's conformation because treatment of SYFs expressing Src^{GFP} WT, which is resistant to CystIMATIK probes, with **3** did not significantly increase membrane blebs (**Figure 2.9D**). Deletion of the GFP tag did not change the results (**Figure 2.9E-F**). To exclude artifacts arising from variability in probe cell permeability, we performed a pre-treatment competition experiment with inhibitor **2**. Consistent with the ability of inhibitor **2** to rapidly permeate cells and occupy the ATP-binding site of Src, Src V284C-expressing cells pre-treated with **2** for 15 minutes prior to addition of **3** showed levels of blebbing comparable

to cells treated with DMSO or **2** alone (**Figure 2.8A**, **Figure 2.9F**). Thus, the open global conformation of Src, stabilized by **3**, appears to promote blebbing in a phosphotransferase-independent fashion.

The blebbing observed in Src^{GFP} E381T- and Src^{GFP} V284C-expressing SYFs treated with **3** are similar in dynamics and scale to features that depend on Rho GTPase-mediated contractility (Charras, 2008). Indeed, pre-treating Src^{GFP} V284C-expressing SYFs or Src^{myr} V284C-expressing HeLa cells with a selective inhibitor of the Rho effector kinase Rock prevented **3**-promoted blebbing (**Figure 2.8D**, **Figure 2.9G**). To explore whether Src membrane localization is important for blebbing, we tested whether **3** could promote blebbing in SYFs expressing Src^{GFP} G2A/V284C, which cannot be myristoylated at its N-terminus. This Src mutant demonstrates a decreased association with membranes because both the N-myristoyl group and the polybasic SH4 domain are required for high affinity membrane interaction (Sigal et al., 1994). Treatment of Src^{GFP} G2A/V284C-expressing SYFs with **3** did not produce blebbing (**Figure 2.8E**), suggesting that adoption of an open conformation alone is insufficient to induce blebbing and that high affinity membrane association is required.

Overexpression of SFK SH4 domain constructs also results in dynamic membrane blebbing through an incompletely defined mechanism (Tournaviti et al., 2007). Our discovery that **3** produces a similar phenotype suggests that Src's membrane-interacting N-terminus can be allosterically modulated through Src's ATP-binding site like its SH2 and SH3 domains. Thus, we performed co-sedimentation assays with purified, myristoylated WT Src (Src^{FLAG}), analogs of our CystIMATIK probes (inhibitors **4**-**6**, **Figure 2.8F**), and liposomes (**Figure 2.8G**, **Figure 2.9H-I**). The Src^{FLAG}-**6** complex, stabilized in the DFG-out conformation, showed significantly increased liposome association compared to *apo* Src^{FLAG} and the Src^{FLAG}-**4** complex, suggesting that the N-terminus is more accessible to membranes when intramolecular SH2 and SH3 domain engagement is disrupted. Furthermore, stabilization of the helix αC-out conformation with inhibitor **5** resulted in the lowest level of co-sedimentation, reinforcing a correlation between SH2/SH3 domain intramolecular engagement and N-terminus sequestration. Thus, stabilization of the DFG-out conformation, with concomitant adoption of an open global conformation, increases the accessibility of Src's membrane-interacting N-terminus. Moreover, promoting Src's open global conformation results in striking blebbing, which requires Src's interactions with membranes but not its phosphotransferase activity.

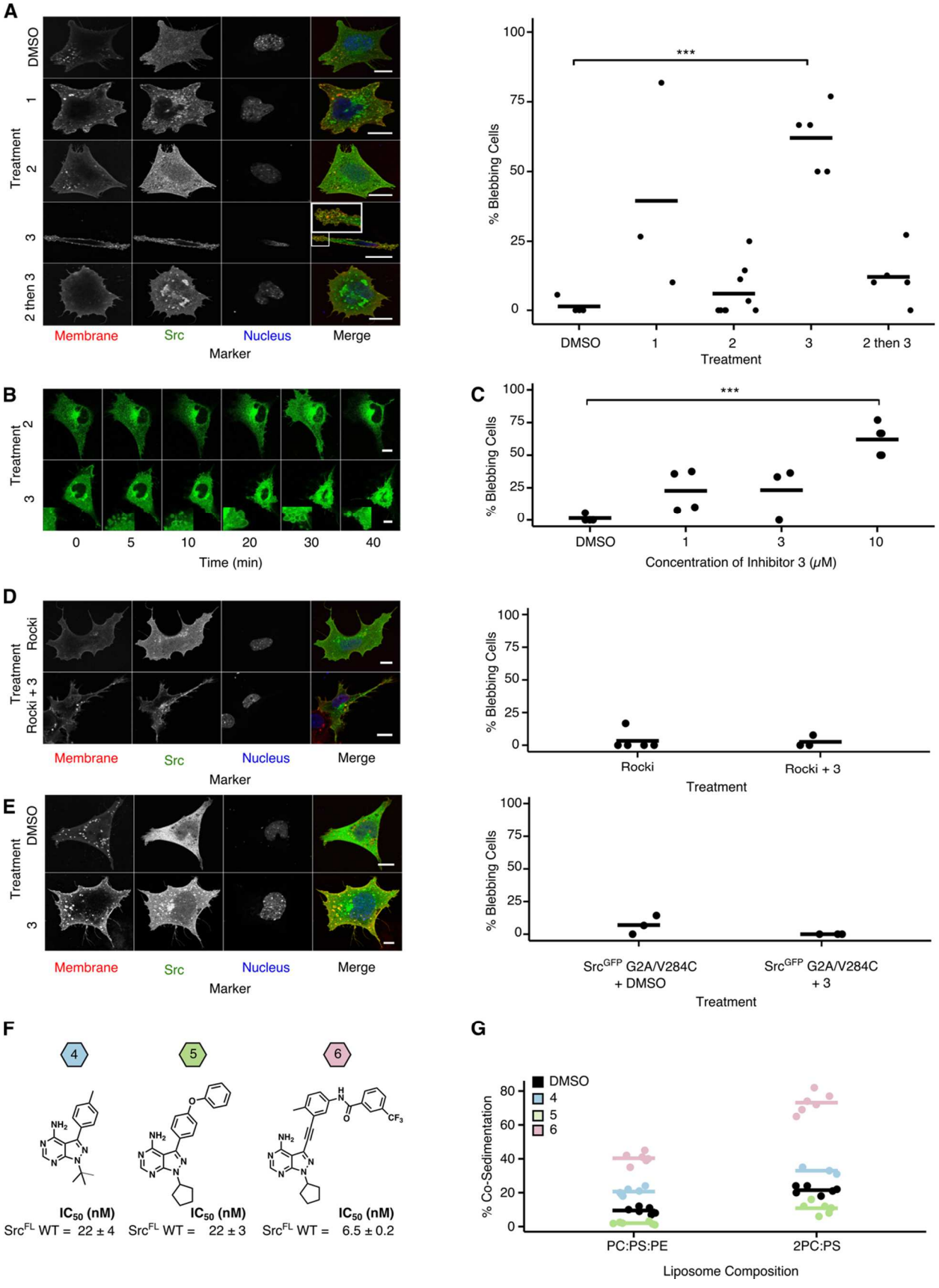
A
DMSO
1
2
3
2 then 3
Treatment
Membrane
Src
Nucleus
Merge
Marker
% Blebbing Cells
***
DMSO
1
2
3
2 then 3
Treatment
B
Treatment
2
3
0
5
10
20
30
40
Time (min)
C
% Blebbing Cells
***
DMSO
1
3
10
Concentration of Inhibitor 3 (μM)
D
Treatment
Rocki
Rocki + 3
Membrane
Src
Nucleus
Merge
Marker
% Blebbing Cells
Rocki
Rocki + 3
Treatment
E
Treatment
DMSO
3
Membrane
Src
Nucleus
Merge
Marker
% Blebbing Cells
SrcGFP G2A/V284C + DMSO
SrcGFP G2A/V284C + 3
Treatment
F
4
5
6
IC50 (nM)
SrcFL WT = 22 ± 4
IC50 (nM)
SrcFL WT = 22 ± 3
IC50 (nM)
SrcFL WT = 6.5 ± 0.2
G
% Co-Sedimentation
DMSO
4
5
6
PC:PS:PE
2PC:PS
Liposome Composition

Figure 2.8. Conformational changes at the ATP-binding site drive phosphotransferase-independent cellular blebbing.
A. Representative micrographs (*left*) and percent bleb quantification (*right*) for Src^{GFP} V284C-expressing SYFs treated for 15 min with DMSO, CystIMATIK probe 1, 2, 3, or pre-treated with 2 for 15 min, followed by 3. **B**. Representative micrographs from time course experiments performed with Src^{GFP} V284C-expressing SYFs treated with CystIMATIK probe 2 or 3. Insets show membrane blebs. **C**. Percentage of Src^{GFP} V284C-expressing SYFs treated with 1, 3, or 10 μM 3 for 15 min showing blebs. Values for DMSO and 10 μM conditions were used previously in Figure 2.8A. **D**. Representative micrographs (*left*) and percent bleb quantification (*right*) for Src^{GFP} V284C-expressing SYFs pre-treated with the Rock inhibitor GSK429286A, and then treated with DMSO or 3 for 15 minutes. **E**. Representative micrographs (*left*) and percent bleb quantification (*right*) for Src^{GFP} G2A/V284C-expressing SYFs treated with DMSO or 3 for 15 minutes. **F**. Structures of probes 4, 5, and 6 and IC_{50} values for Src^{FL} WT determined in the presence of 1 mM ATP (n=3, mean ± s.e.m). **G**. Quantification of Src immunoblots for co-sedimentation assays performed with *apo* Src^{FLAG}, Src^{FLAG}-4, Src^{FLAG}-5, or Src^{FLAG}-6, and lipsosomes composed of 1:1:1 phosphatidylcholine, phosphatidylserine and phosphatidylethanolamine (PC:PS:PE) or 2:1 PC and PS (2PC:PS). In all micrographs, scale bars = 10 μm. For 2.8A-E, each point represents a replicate treatment with multiple cells imaged and scored in a double-blind fashion. Horizontal lines indicate the mean of all replicates. ***$p < 0.001$.

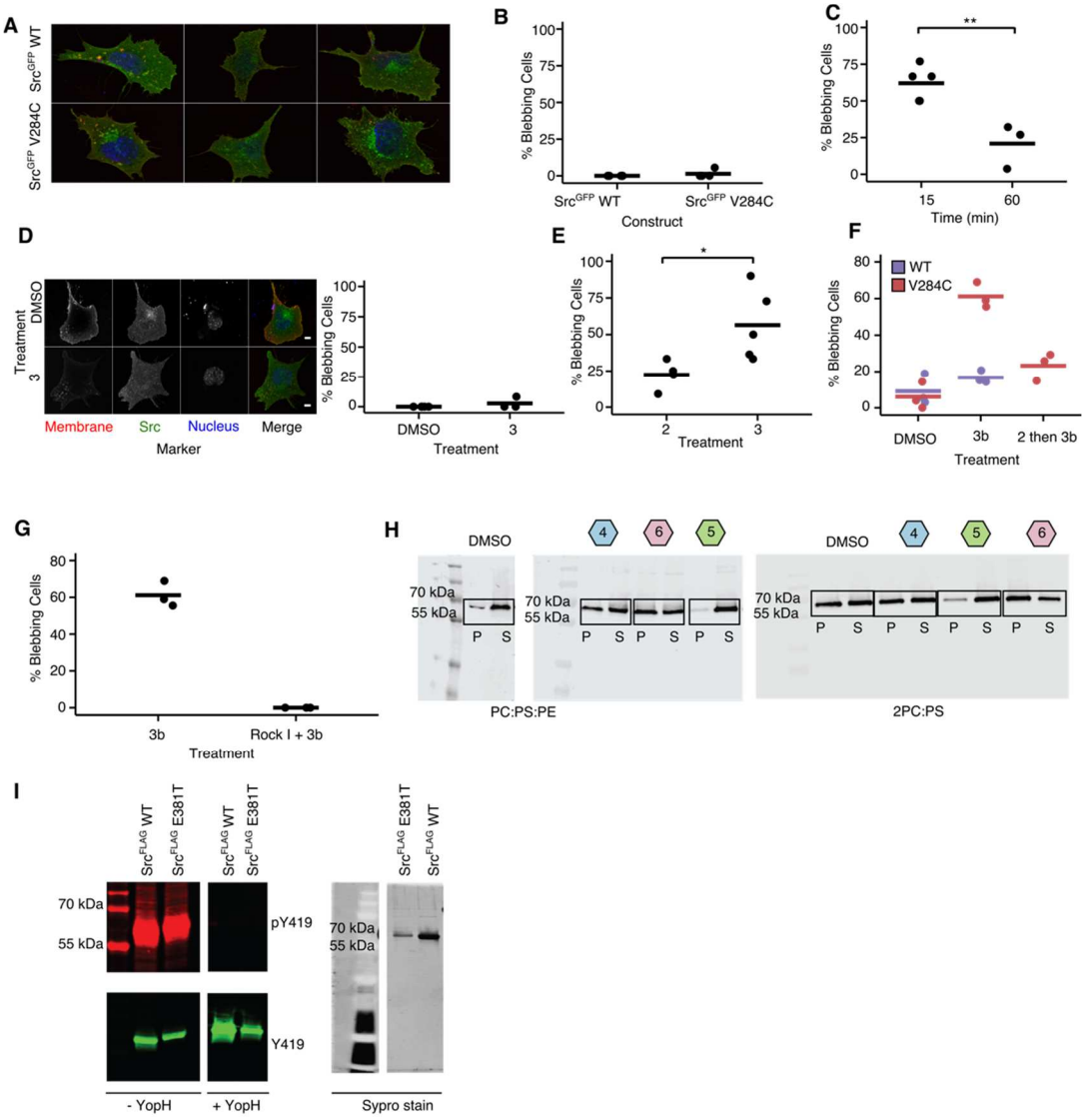

Figure 2.9. Conformational changes at the ATP-binding site drive phosphotransferase-independent cellular blebbing

A. Three representative micrographs of untreated SYFs expressing Src^{GFP} WT or Src^{GFP} V284C. **B**. Percentage of untreated SYFs expressing expressing Src^{GFP} WT or Src^{GFP} V284C with blebs. **C**. Percentage of SYFs expressing Src^{GFP} V284C with blebs 15 or 60 min after treatment with 3. **D**. Representative micrographs of Src^{GFP} WT-expressing SYFs treated for 15 min with DMSO or 3 (*left panels*). Percentage of Src^{GFP} WT-expressing SYFs with blebs after treatment with DMSO or 3 for 15 minutes. **E**. Percentage of Src^{myr} V284C-expressing SYFs with blebs after treatment with 2 or 3 for 15 min. **F**. Percentage of HeLa cells expressing Src^{myr} WT or Src^{myr} V284C with blebs after treatment with DMSO, 5 μM 3b, or pre-treated with 2 for 15 min, followed by 3b (3b is an analog of CystIMATIK probe 3 that lacks a methyl group on the cyanoacrylamide moiety). **G**. Percentage of HeLa cells expressing Src^{myr} V284C pre-treated with DMSO or Rock inhibitor GSK429286A, and then treated with 3b. **H**. Representative Src (anti-Src) immunoblots for the co-sedimentation assays quantified in Figure 2.8G. (P) = pelleted and (S) = soluble Src fractions after sedimentation. Representative data for *apo* Src^{FLAG} WT (DMSO), Src^{FLAG} WT-4, Src^{FLAG} WT-5 or Src^{FLAG} WT-6 with

liposomes composed of 1:1:1 phosphatidylcholine, phosphatidylserine and phosphatidylethanolamine (PC:PS:PE) or 2:1 PC and PS (2PC:PS) are shown. Pelleted and soluble Src were quantified by fitting the immunoblot signal intensity to a Src (using an anti-Src antibody) titration standard curve. **I**. Purification and characterization of non-phosphorylated Src^{FLAG} WT and Src^{FLAG} E381T from HEK293T cells. The left panels show phosphorylated (anti-pTyr419 SFK) and non-phosphorylated (anti-Tyr419 SFK) blots before (- YopH) and after (+ YopH) treatment with *Yersinia pestis* protein tyrosine phosphatase (YopH). The right panels show total protein (Sypro staining) after dephosphorylation and purification. For 2.9B-G, each point represents a replicate treatment with multiple cells imaged and scored in a double-blind fashion. Points represent individual measurements and the horizontal lines indicate the mean of all measurements. $p < 0.05$; $^{**}p < 0.01$.

Characterization of a N-terminal regulatory site in Src

Our co-sedimentation and cellular data are consistent with intramolecular sequestration of Src's N-terminus in the closed global conformation, preventing membrane interaction. Disengagement of the SH2 and SH3 regulatory domains disrupts this sequestration and exposes the N-terminus in the open global conformation. Moreover, our large-scale mutagenesis and biochemical data support the importance of the αF pocket in regulating Src's conformation. Thus, guided by structure-based modeling, we hypothesized that the αF pocket binds to and sequesters the N-terminus (**Figure 2.10A**, **Figure 2.11A**). Our hypothesis predicts that αF pocket mutations should disrupt sequestration of the N-terminus, exposing it and increasing Src's affinity for membranes. We performed co-sedimentation assays comparing membrane association of purified Src^{FLAG} WT and Src^{FLAG} E381T (**Figure 2.10B**, **Figure 2.11B**). Src^{FLAG} E381T showed enhanced membrane association relative to Src^{FLAG} WT, implying that the E381T mutation results in a more membrane-accessible N-terminus.

We also observed that the αF pocket mutations increase the phosphotransferase activity of full-length Src in yeast, mammalian cells, and *in vitro*. Moreover, deletion of the SH4 domain (Src^{3D} or $Src^{\Delta SH4}$) resulted in a ~10-fold increase in phosphotransferase activity compared to Src^{FL} WT (**Figure 2.10C**, **Figure 2.11C-E**). These observations suggest a model where the SH4 domain serves as a "fastener" promoting the intramolecular association of Src's regulatory SH2 and SH3 domains through its interaction with the αF pocket, thereby decreasing phosphotransferase activity. If αF pocket mutations and SH4 domain deletions abrogate the same SH4 domain/αF pocket interaction, then combining the two should yield a minimal additional increase in phosphotransferase activity. Indeed, neither E381T nor I444K appreciably increased the phosphotransferase activity of Src^{3D} or $Src^{\Delta SH4}$ (**Figure 2.10C**, **Figure 2.11C-E**). In contrast, activating mutations located outside of the αF pocket further increased Src^{3D}'s catalytic activity (**Figure Figure 2.11E**). N-terminal myristoylation

did not affect E381T activity, suggesting that E381T mainly disrupts interactions with the SH4 domain and not the N-terminal myristoyl group (**Figure Figure 2.11F**). Finally, E381T increased purified Src^{FL}'s capacity for activation loop autophosphorylation, and, as for *trans*-phosphorylation, deletion of the SH4 domain did not increase autophosphorylation further (**Figure 2.10D**, **Figure 2.11G**). Thus, mutations in the αF pocket and deletion of the SH4 domain are both activating in a variety of contexts, but combining the two does not further increase activity.

Consistent with the αF pocket/SH4 domain fastener model, the level of intramolecular SH3 domain engagement of constructs lacking an SH4 domain ($Src^{\Delta SH4}$ or Src^{3D} WT) was lower than Src^{FL} WT in a pulldown assay (**Figure 2.10E**, **Figure 2.11H-J**). While αF pocket mutations significantly decreased intramolecular SH3 domain engagement in Src^{FL}, they only minimally influenced the already increased level of SH3 domain disengagement in constructs lacking an SH4 domain (**Figure 2.10E**, **Figure 2.11H-J**). Thus, mutations in the αF pocket appear to activate Src's phosphotransferase activity by releasing intramolecular autoinhibition promoted by the SH4 domain fastener, although indirect disruption of the SH2/CD interface may also contribute. These results strongly suggest that the activity-modulating effects of the SH4 domain and the αF pocket operate through the same mechanism and that these two distal regions physically interact.

Next, we used chemical footprinting to determine whether the αF pocket is shielded when Src is in the closed global conformation (**Figure 2.10F**-**H**). We measured isotopically-coded maleimide labeling (Kahsai et al., 2014) of a purified Src construct (Src^{FL} K445C) containing a solvent accessible cysteine mutation. Isotopic coding allowed ratiometric, quantitative comparisons of maleimide labeling between Src^{FL} complexed to inhibitors **5** or **6**, which promote closed or open global conformations, respectively. We found that K445C labeling was ~5-fold greater in the DFG-out, open conformation compared to the helix αC-out, closed conformation (**Figure 2.10H**). However, no change in labeling was observed at a control cysteine residue whose accessibility should not change between the closed and open conformations. Deletion of the SH4 and Unique domains abrogated global conformation-dependent differences in labeling of K445C, suggesting that the N-terminal region physically occludes the αF pocket.

We next evaluated the interaction in *trans* by performing pulldowns with an immobilized construct consisting of the non-myristoylated SH4 domain of Src (**Figure 2.10I**). A Src construct containing only the CD (Src^{CD}) exhibited efficient SH4 domain-mediated pulldown (**Figure 2.10J**, **Figure 2.11K**). Moreover, E381T and I444K mutations abrogated pulldown in the context of Src^{CD}, while activating mutations located outside the αF pocket did not. Src^{FL} WT demonstrated less

efficient pulldown than Src^{CD} WT, consistent with intramolecular SH4 domain engagement competing with SH4 pulldown in *trans* (**Figure 2.10K**). Moreover, pulldown of the SH2/SH3 domain-disengaged Src^{FL} V284C-**3** complex was much greater than the SH2/SH3 domain-engaged Src^{FL} V284C-**2** complex, showing that the conformation of Src's regulatory SH2 and SH3 domains are coupled to the SH4 domain's fastening interaction with the αF pocket (**Figure 2.11L**). Thus, a more open global conformation of full-length Src increases αF pocket accessibility and hence pulldown with an immobilized SH4 domain in *trans*.

Finally, the non-myristoylated SH4 domain construct used for pulldowns did not affect Src^{CD} autophosphorylation when added in *trans*, suggesting that the SH4 domain fastener does not directly influence the CD's phosphotransferase activity (**Figure 2.11M**). However, the rate of Src^{FL} autophosphorylation increased in the presence of the non-myristoylated SH4 domain construct, consistent with disruption of intramolecular SH4 domain-mediated autoinhibition (**Figure 2.11N**). Autophosphorylation of I444K and E381T Src^{FL} were not affected by the addition of the non-myristoylated SH4 domain construct (**Figure 2.11O**), consistent with these mutations disrupting the interaction between the αF pocket and SH4 domain either in *cis* or in *trans*.

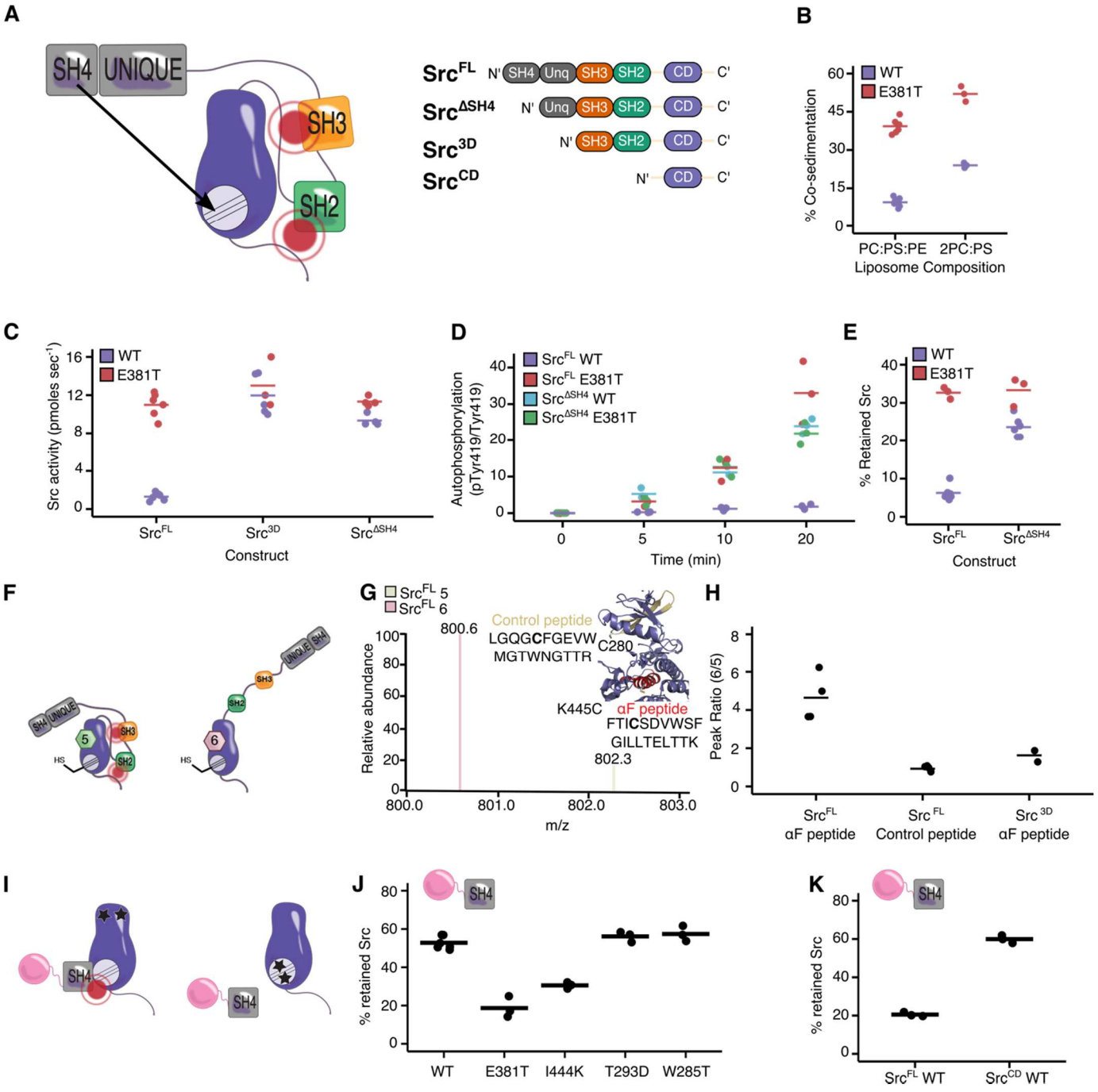

Figure 2.10. Direct interaction of the SH4 and catalytic domain regulates Src activity and dictates cellular phenotype.

A. Proposed SH4 domain "fastener" model (*left*) and the Src constructs used for biochemical characterization (*right*). **B**. Quantification of Src immunoblots for co-sedimentation assays performed with Src^{FLAG} WT or Src^{FLAG} E381T, and liposomes composed of PC:PS:PE or 2PC:PS. **C**. Phosphotransferase activity of purified Src^{FL}, Src^{3D} or $Src^{\Delta SH4}$ with either the WT or E381T sequence. (n=4-6). Values for Src^{FL} WT and E381T were used previously in Figure 2.4C. **D**. Autophosphorylation quantification of Src^{FL} or $Src^{\Delta SH4}$ with either the WT or E381T sequence at various time points after ATP addition (n=3). **E**. Percent retained Src in the SH3 pulldown assay

with purified Src^{FL} or $Src^{\Delta SH4}$ with either the WT or E381T sequence (n=3-5). Values for Src^{FL} WT were used previously in Figure 2.4E. **F**. Model showing the global conformation of Src^{FL} K445C-5 or Src^{FL} K445C-6. **G**. Isotope-coded maleimide labeling of Src^{FL} K445C. An example mass spectrum of the light and heavy maleimide-labeled peptide containing K445C (αF peptide). The inset shows the location of the αF and control peptides. **H**. Peak intensity ratios of the maleimide-labeled αF and control peptides from the Src^{FL} K445C-5 or Src^{FL} K445C-6 complexes (n=4). Peak intensity ratios of the maleimide-labeled αF peptide from the Src^{3D} K445C-5 or Src^{3D} K445C-6 complexes (n=2) are also shown. **I**. SH4 pulldown assay schematic. Src variants are incubated with the immobilized SH4 domain (residues 1-18) of Src and the amount of retained Src is quantified after washing and elution. Src^{CD} variants with mutations outside (*left*) and within (*right*) the αF pocket are shown. **J**. Percent retained Src in the SH4 pulldown assay with purified Src^{CD} WT, E381T, I444K, T293D, or W285T (n=3). **K**. Percent retained Src in the SH4 pulldown assay with purified Src^{CD} WT or Src^{FL} WT (n=3). Points represent individual measurements and the horizontal lines indicate the mean of all measurements.

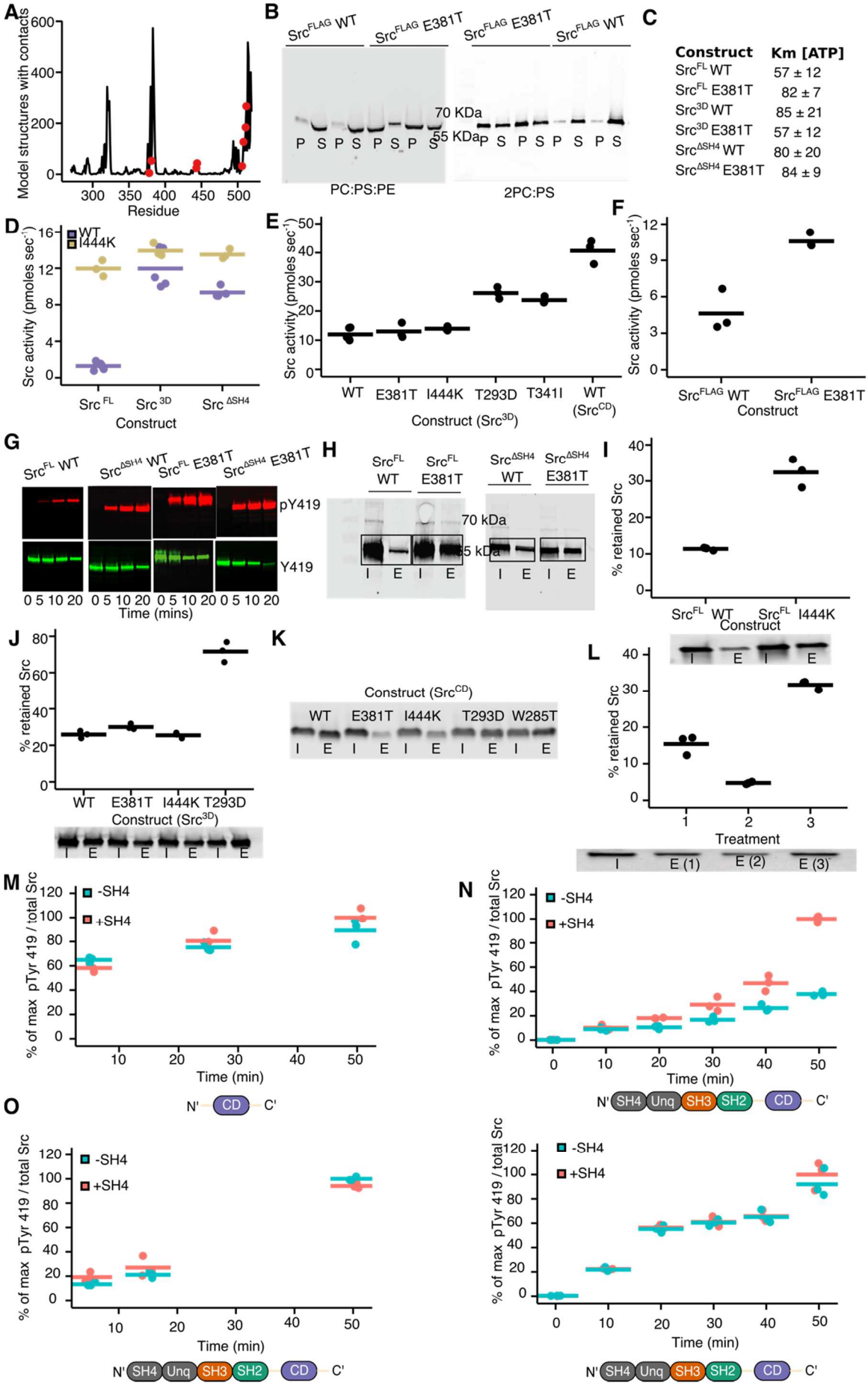
A
Model structures with contacts
Residue
B
Src^FLAG WT
Src^FLAG E381T
Src^FLAG E381T
Src^FLAG WT
70 KDa
55 KDa
P S P S P S P S P S P S P S P S
PC:PS:PE
2PC:PS
C
Construct
Km [ATP]
Src^FL WT 57 ± 12
Src^FL E381T 82 ± 7
Src^3D WT 85 ± 21
Src^3D E381T 57 ± 12
Src^ΔSH4 WT 80 ± 20
Src^ΔSH4 E381T 84 ± 9
D
WT
I444K
Src activity (pmoles sec-1)
Src FL
Src 3D
Src ΔSH4
Construct
E
Src activity (pmoles sec-1)
WT
E381T
I444K
T293D
T341I
WT (Src^CD)
Construct (Src^3D)
F
Src activity (pmoles sec-1)
Src^FLAG WT
Src^FLAG E381T
Construct
G
Src^FL WT
Src^ΔSH4 WT
Src^FL E381T
Src^ΔSH4 E381T
pY419
Y419
0 5 10 20 0 5 10 20 0 5 10 20 0 5 10 20
Time (mins)
H
Src^FL WT
Src^FL E381T
Src^ΔSH4 WT
Src^ΔSH4 E381T
70 kDa
55 kDa
I E I E I E I E
I
% retained Src
Src^FL WT
Src^FL I444K
Construct
J
% retained Src
WT
E381T
I444K T293D
Construct (Src^3D)
I E I E I E I E
K
Construct (Src^CD)
WT
E381T
I444K
T293D
W285T
I E I E I E I E I E
L
% retained Src
Treatment
I
E (1)
E (2)
E (3)
M
% of max pTyr 419 / total Src
-SH4
+SH4
Time (min)
N'
CD
C'
N
% of max pTyr 419 / total Src
-SH4
+SH4
Time (min)
N'
SH4
Unq
SH3
SH2
CD
C'
O
% of max pTyr 419 / total Src
-SH4
+SH4
Time (min)
N'
SH4
Unq
SH3
SH2
CD
C'
% of max pTyr 419 / total Src
-SH4
+SH4
Time (min)
N'
SH4
Unq
SH3
SH2
CD
C'

Figure 2.11. Characterization of the SH4 domain/αF pocket interaction.
A. 4,528 N-tail model structures were created with Rosetta based on the 2SRC crystal structure. Plot of the number of N-tail model structures that contact each catalytic domain residue. The red dots indicate αF pocket residues. **B**. Representative Src (anti-Src) immunoblots for the co-sedimentation assays quantified in Figure 2.10B. P = pelleted and S = soluble Src fractions after sedimentation. Representative data for *apo* Src^{FLAG} WT (DMSO) and *apo* Src^{FLAG} E381T with liposomes composed of 1:1:1 phosphatidylcholine, phosphatidylserine and phosphatidylethanolamine (PC:PS:PE) or 2:1 PC and PS (2PC:PS) are shown. Pelleted and soluble Src were quantified by fitting the immunoblot signal intensity to a Src (using an anti-Src antibody) titration standard curve. **C**. K*m* [ATP] for Src^{FL} WT, Src^{FL} E381T, Src^{3D} WT, Src^{3D} E381T, $Src^{\Delta SH4}$ WT and $Src^{\Delta SH4}$ E381T (n=3, mean ± s.e.m). **D**. Phosphotransferase activity of purified Src^{FL}, Src^{3D} or $Src^{\Delta SH4}$ with either the WT or I444K sequence. (n=4-6). Values for WT (FL and truncations) were used previously in Figure 2.10C. **E**. Phosphotransferase activity of purified Src^{3D} comparing WT, E381T, I444K, T293D and T341I sequence (n=3-5). The phosphotransferase activity of Src^{CD} WT is provided as reference for Src's activity in the absence of regulatory SH2 and SH3 domains. Values for Src^{3D} WT, E381T, and I444K were shown previously in Figures 2.10C, 2.10D. **F**. Phosphotransferase activity of Src^{FLAG} with either the WT or E381T sequence (n=3) purified from HEK293T cells. **G**. Representative (anti-pTyr419 SFK) (*top*) and non-phosphorylated (anti-Tyr419 SFK) (*bottom*) Src immunoblots for autophosphorylation assays quantified in Figure 2.10D. Non-phosphorylated Src variants were incubated with ATP (30 μM) for varying times and then the ratio of pTyr419 and Tyr419 was quantified. **H**. Representative Src immunoblots for SH3 pulldown assays performed with $Src^{\Delta SH4}$ WT or E381T and Src^{FL} WT or E381T and quantified in Figure 2.10E. (I = input Src construct; E = Src construct retained after SH3 pulldown). Retained Src was quantified by fitting the immunoblot signal intensity to a Src titration standard curve. **I**. Quantification (*top panel*) and representative immunoblots (*bottom panel*) for SH3 pulldown assays performed with Src^{FL} WT or I444K (n=3, I = input Src construct; E = Src construct retained after SH3 pulldown). Values for Src^{FL} WT were used previously in Figure 2.10E. **J**. Quantification (*top panel*) and representative immunoblots (*bottom panel*) for SH3 pulldown assays performed with Src^{3D} WT, E381T, I444K and T293D (n=3, I = input Src construct; E = Src construct retained after SH3 pulldown). **K**. Representative immunoblots for SH4 pulldown assays performed with Src^{3D} WT, E381T, I444K, T293D and W285T (I = input Src construct; E = Src construct retained after SH4 pulldown). Retained Src was quantified by fitting the immunoblot signal intensity to a Src titration standard curve. **L**. Quantification (*top panel*) and representative fluorescent gel (*bottom panel*) for SH4 pulldown assays performed with tetramethylrhodamine-labeled $Src^{TAMRA\text{-}FL}$ V284C (Figure S1A and Table S1) complexed to 5 μM inhibitor 1, 2, or 3 (n=3, I = input $Src^{TAMRA\text{-}FL}$ V284C; E = $Src^{TAMRA\text{-}FL}$ V284C retained after SH4 pulldown). Input and eluted Src was quantified using fluorescence gel scanning. **M**. Autophosphorylation quantification of Src^{CD} WT in the presence of $SH4^{SNAP}$ (residues 1-18 of Src, +SH4, *red*) or control SNAP (-SH4, *blue*) at various time points after the addition of ATP (n=3). **N**. Autophosphorylation quantification of Src^{FL} WT in the presence of $SH4^{SNAP}$ (residues 1-18 of Src, +SH4, *red*) or control SNAP protein (-SH4, *blue*) at various time points after the addition of ATP (n=3). **O**. Autophosphorylation quantification of Src^{FL} E381T (*left*) and I444K (*right*) in the presence of $SH4^{SNAP}$ (residues 1-18 of Src, +SH4, *red*) or control SNAP protein (-SH4, *blue*) at various time points after the addition of ATP (n=3). For 2.11N-O, autophosphorylation was quantified by measuring the ratio of pTyr419 (anti-pTyr419 SFK) to total Src (anti-Src) by immunoblotting. Points represent individual measurements and the horizontal lines indicate the mean of all measurements.

The SH4 domain regulatory interaction is conserved in other SFKs

We revealed a previously unknown, direct regulatory interaction between Src's SH4 domain and its αF pocket and showed that the interaction regulates Src's conformation, activity, localization and effect on cells. Src shares a common domain architecture with the seven other human SFKs, suggesting that the SH4 domain regulatory interaction might also be shared. The αF pocket is highly conserved amongst SFKs but varies considerably among the 12 human tyrosine kinases that have the same SH3/SH2/CD domain organization as the SFKs but lack SH4 domains (SH4-, **Figure 2.12A**, **Figure 2.13A**). To better understand the meaning of these substitutions, we analyzed them in light of their effects on Src phosphotransferase activity (**Figure 2.4F**). Neither of the two SFK substitutions, relative to Src, were gain-of-function whereas 11 of the 48 SH4- kinase substitutions were gain-of-function. While the limited number of substitutions amongst the SFKs precludes meaningful statistical analysis, this trend suggests that αF pocket substitutions in SFKs preserve interaction with the SH4 domain, whereas substitutions in SH4- kinases disrupt it.

To provide additional support for the conservation of the SH4 domain/αF pocket interaction amongst SFKs, we investigated Fyn. As for Src, deletion of Fyn's SH4 and Unique domains (Fyn^{3D}) increased phosphotransferase activity and promoted an SH3 domain-accessible, open global conformation relative to Fyn^{FL} (**Figure 2.12B-C**, **Figure 2.13B**). Treatment of Fyn^{myr} V284C-expressing SYFs with probe **3** resulted in a marked increase in blebbing, like for Src (**Figure 2.12D**, **Figure 2.13C**). Thus, Fyn likely has an intramolecular SH4 domain interaction analogous to Src's.

Unlike the αF pocket, SFK SH4 domain sequences are diverse, leading us to wonder which residues are important for the SH4 domain/αF pocket interaction. Therefore, we asked whether the phosphotransferase activity of SH4 domain variants could be measured in yeast. We worried that yeast activity measurements could be confounded by SH4 domain variant effects on myristoylation and localization. However, we found that two N-terminal Src truncations ($Src^{\Delta SH4}$ and Src^{3D}), which are not myristoylated and cannot associate with membranes, strongly suppressed yeast growth, reflecting their enhanced *in vitro* activities (**Figure 2.13D**). Encouraged by these results, we performed a DMS of Src's SH4 domain (residues 2-19) in the context of Src^{myr} (**Figure 2.12E**). Unlike for Src's CD, 76% of SH4 domain mutations were functionally neutral, with only 16% resulting in loss-of-function and 8% in gain-of-function. Thus, the SH4 domain is under greatly reduced functional constraint, relative to the CD. Mutations at SH4 domain residues 2 through 9 had much larger effects, both positive and negative, than mutations at residues 10 through 19. In

particular, mutations at residues Ser3 and Pro8 conferred greatly increased Src activity. Pulldown of Src^{3D} with SH4 domain P8N, one of the most activating mutants, was substantially decreased compared to WT (**Figure 2.12F, Figure 2.13E**). Introduction of a second gain-of-function mutant, K5I, further decreased Src^{3D} pulldown. The importance of the N-terminal portion of the SH4 domain for interacting with the αF pocket helps to explain why disruption of this interaction alters Src's capacity to interact with membranes *in vitro* and in cells because this region is also required for high affinity membrane interactions (McLaughlin and Aderem, 1995).

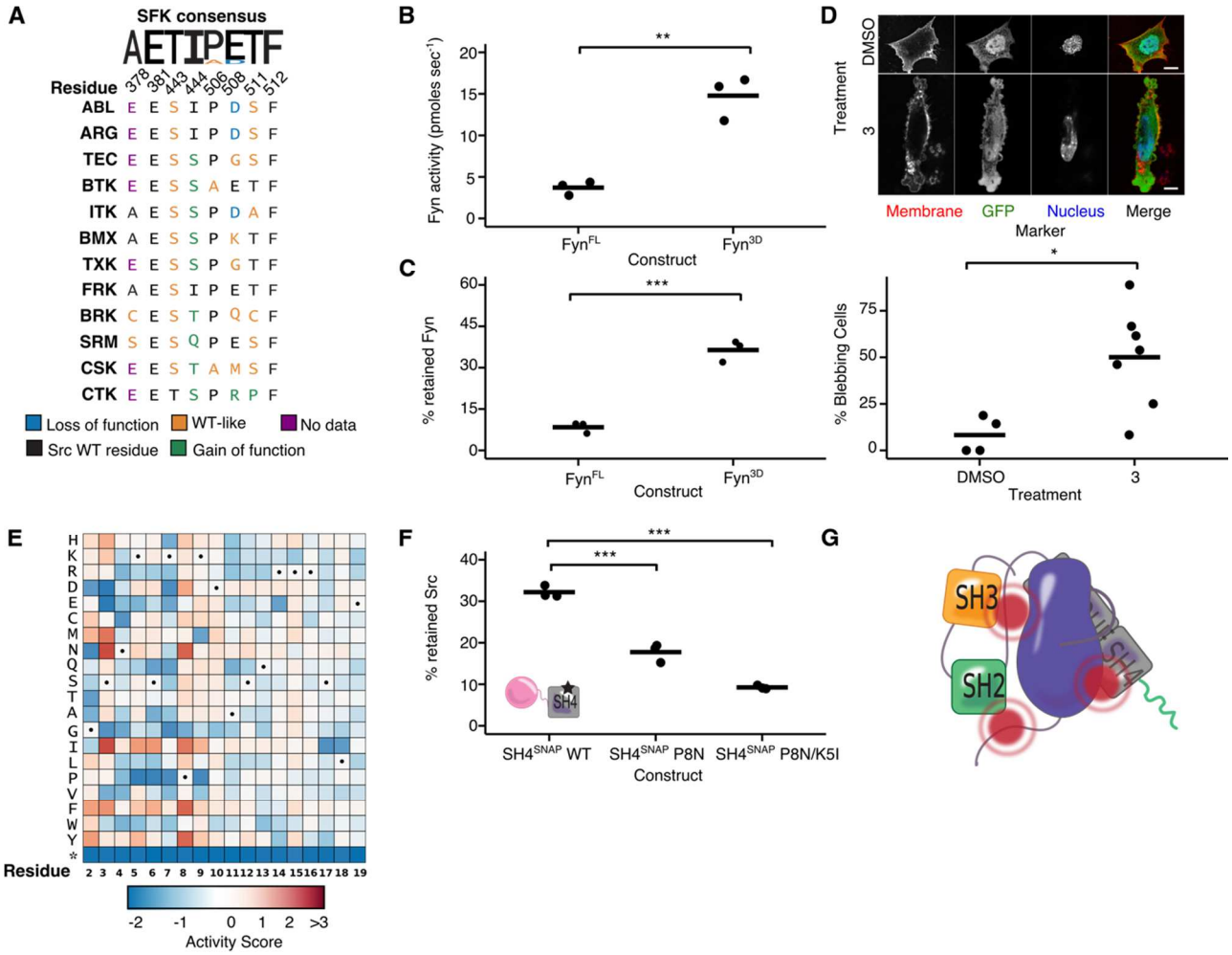

Figure 2.12. . Functional characterization of the SH4 domain/αF pocket interaction. **A.** Sequence alignment of SH4 domain-lacking human non-receptor tyrosine kinases (SH4-) at αF pocket residues. Colors indicate classification of the analogous mutation from the Src DMS. **B.** Phosphotransferase activity of purified Fyn^{FL} WT or Fyn^{3D} WT (n=3). **C.** Percent retained Fyn in the SH3 pulldown assay with purified Fyn^{FL} WT or Fyn^{3D} WT (n=3). **D.** Representative micrographs (*top panel*) and percent bleb quantification (*bottom panel*) for Fyn^{myr}-expressing SYFs treated with

DMSO or CystIMATIK probe 3 for 15 min. **E**. DMS of Src's SH4 domain. Dots indicate WT amino acid at that residue. **F**. Percent retained $Src^{TAMRA\text{-}3D}$ in an SH4 pulldown assay with immobilized WT, P8N, or P8N/K5I SH4 domain (n=3). **G**. Proposed model of SH4 domain-mediated autoinhibition (myristoyl (*green*), unstructured SH4 and Unique (*gray*), SH3 (*orange*), SH2 (*green*), and CD (*purple*)). For 2.12D, each point represents a replicate treatment with multiple cells imaged and scored in a double-blind fashion. Horizontal lines indicate the mean of all replicates.

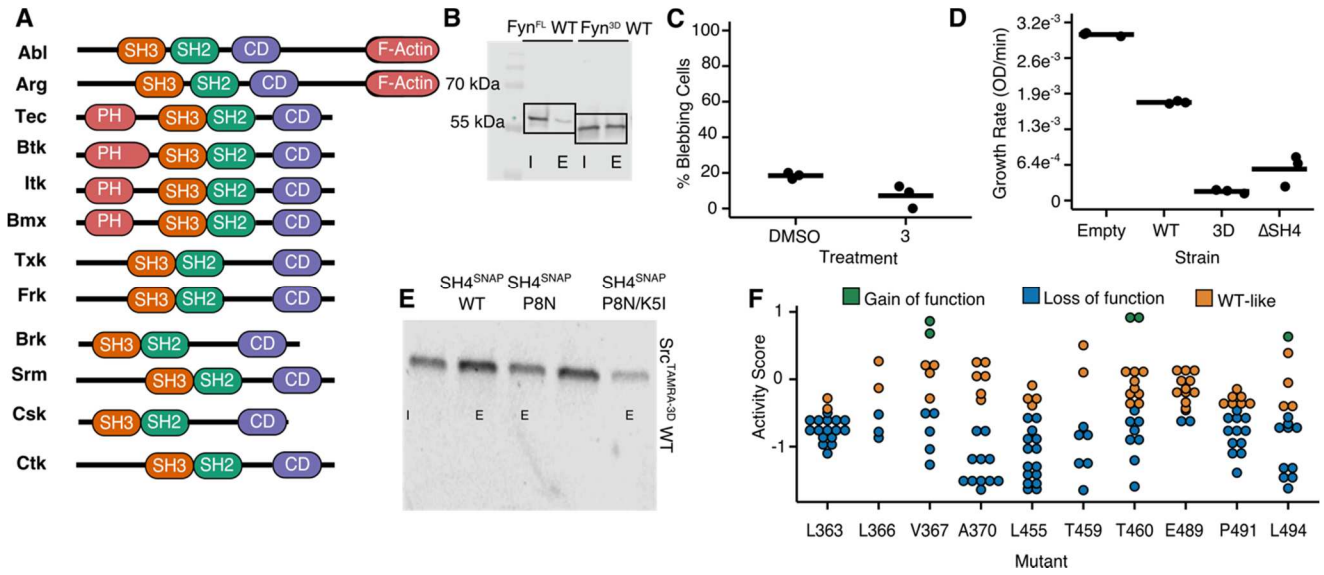

Figure 2.13. Conservation of the SH4 domain regulatory interaction amongst the SFKs. **A.** Domain organization of SH4 domain-lacking (SH4-) human non-receptor tyrosine kinases that contain an SH3/SH2/CD architecture. **B**. Representative Fyn immunoblots (anti-Tyr419 SFK) for SH3 pulldown assays performed with Fyn^{FL} WT or Fyn^{3D} WT. (I = input Fyn construct; E = Fyn construct retained after SH3 pulldown). Retained Fyn was quantified by fitting the immunoblot signal intensity to a Fyn (anti-Tyr419 SFK) titration standard curve. **C**. Percentage of Fyn^{myr} WT-expressing SYF cells with blebs after treatment with DMSO or 3. **D**. Quantification of growth rates in yeast strains expressing Src^{FL} WT, Src^{3D} WT, $Src^{\Delta SH4}$ WT, or empty vector control (n=3). **E**. Representative fluorescent gel of SH4 pulldown assays performed with tetramethylrhodamine-labeled $Src^{TAMRA\text{-}3D}$ WT and immobilized $SH4^{SNAP}$ (residues 1-18 of Src) variants (WT, P8N or P8N/K5I) (n=3, I = input $Src^{TAMRA\text{-}3D}$ WT; E = $Src^{TAMRA\text{-}3D}$ WT retained after SH4 pulldown). **F**. Activity scores of Src residues that overlay with Abl's myristoyl-binding pocket (as defined in Cowan-Jacob, 2005). Most variants in this region are loss-of-function or WT-like. Points represent individual measurements and the horizontal lines indicate the mean of all measurements.

2.4 DISCUSSION

Together, DMS and CystIMATIK revealed a regulatory interaction in Src, defined by the intramolecular engagement of the membrane-interacting, N-terminal SH4 domain with the αF pocket in the C-terminal lobe of the CD. We propose that the interaction between the SH4 domain and the αF pocket serves as a fastener that enhances autoinhibitory engagement of the core SH2/SH3 regulatory module with the CD (**Figure 2.12G**). By enhancing SH2/SH3 domain-mediated autoinhibition, the SH4 domain fastener ensures that Src possesses low phosphotransferase activity and minimal accessibility to intermolecular binding partners when the SH4 domain is not associated with membranes. Release of the SH4 domain fastener, through competitive association with membranes, could act as an initial step in Src activation by facilitating increased accessibility of Src's SH2 and SH3 domains to other binding partners. Because the intramolecular engagement of the SH2, SH3, and SH4 domains of Src appear to be coupled, intermolecular binding partners that disrupt autoinhibitory SH2/SH3 domain engagement could also weaken the SH4 domain's intramolecular interaction with the αF pocket and promote the enhanced membrane association of Src.

A recent report suggests that in the open global conformation, Src forms a homodimer that facilitates autophosphorylation via interaction of the N-terminus of one protomer with the CD domain of the other (Spassov et al., 2018). Intramolecular release of the SH4 domain fastener could enable the N-terminus to form an asymmetric dimer with the CD of a second Src protomer. Thus, this dimerization-dependent autophosphorylation mechanism is consistent with our SH4 domain fastener model, with the N-terminus of Src contributing to autoinhibition in a closed global conformation and autophosphorylation in an open global conformation.

A truncated construct comprising Src's SH4, Unique and SH3 domains adopts a compacted structure with SH3 and SH4 interdomain contacts (Maffei et al., 2015). How this affects the SH4 domain's interaction with the αF pocket is unclear, but additional structural studies with full length Src constructs should provide insight into whether these are competitive or complementary binding events. Another unresolved question is how the SH4 domain/αF pocket interaction affects autoinhibition through Src's phosphorylated C-terminal tail. Our SH4 domain fastener model predicts that intramolecular engagement of Src's SH4 domain should strengthen the interaction between the SH2 domain and the CD's phosphorylated C-terminal tail and vice versa. Whether

intramolecular engagement of the SH4 domain affects inhibitory C-terminal tail phosphorylation by Csk and dephosphorylation by phosphatases also remains to be determined.

The SH4 domain/αF pocket interaction likely plays a regulatory role in SFKs beyond Src. Deletion of Fyn's N-terminus led to increased phosphotransferase activity and a more open global conformation, and CystIMATIK probes promoting an open global conformation of Fyn led to blebbing, consistent with release of SH4 domain sequestration. Moreover, the αF pocket sequence is highly conserved amongst SFKs and lacks any gain-of-function substitutions. By contrast, SFK SH4 domains are diverse and subjected to varying degrees of post-translational palmitoylation. What can explain this diversity? Our results show that the SH4 domain is under at least two distinct functional constraints: mediating binding to the αF pocket and binding to membranes. These two different constraints may help to explain the SH4 domain's intrinsic disorder, which is a common strategy for binding to multiple partners (Maffei et al., 2015; Olsen et al., 2017). This intrinsic disorder is reflected in the relative mutational tolerance and low sequence conservation we observed, compared to the αF pocket. Nevertheless, our SH4 domain DMS results suggested that the N-terminal portion of Src's SH4 domain, particularly residues Ser3 and Pro8, are important for interaction with the αF pocket.

In addition to Src, several other tyrosine kinase N-termini add a layer of regulation to a core SH3-SH2-linker-CD architecture (Devkota et al., 2017; Joseph et al., 2017; Wang et al., 2015). For example, Abl's N-terminal myristate binds to its CD, reducing phosphotransferase activity (Hantschel et al., 2003). Like all SKFs, Src's N-terminus is also myristoylated. However, our data, and a previous study, suggest that Src's myristate does not function like Abl's. (Patwardhan and Resh, 2010). The region of Src's CD that overlaps with Abl's myristate-binding pocket, which is ~20 Å away from the αF pocket, contains several sequence differences relative to Abl. Our DMS in yeast, where Src is likely myristoylated because yeast N-myristoyltransferase can efficiently modify Src's N-terminus (Towler et al., 1988), shows almost no Src gain-of-function substitutions in this region (**Figure 2.13F**). The αF pocket could recognize Src's myristate in addition to the SH4 domain, but the biochemical experiments we performed with myristoylated Src suggest that the αF pocket mainly interacts with the SH4 domain.

Like Src and Abl, Btk's N-terminal PHTH domain is important for regulating CD phosphotransferase activity. The details of how the N-termini of Src, Abl, and Btk lead to autoinhibition vary, but they share common mechanistic themes. Like Src's SH4 domain, Abl's N-terminal myristate and Btk's PHTH domain directly interact with the CD. All three N-termini

strengthen autoinhibitory CD/SH3 and CD/SH2 domain interactions, further promoting a closed global conformation. The N-termini of all three kinases have an affinity for lipids, which intramolecular sequestration diminishes. Thus, coupling of membrane association to the release of autoinhibition via the N-terminus appears to be a recurrent theme amongst tyrosine kinases.

Interdomain regulation is a defining feature of multidomain kinases, and ~50% of kinases contain more than one domain. Our discovery of a intramolecular regulatory interaction in Src, one of the best-studied kinases, highlights the need to dissect kinase intramolecular regulation. In addition to modulating phosphotransferase activity, kinase regulatory domains often mediate important phosphotransferase-independent functions, as is the case for Src's SH4 domain. We showed how two powerful tools, DMS and CystIMATIK, can be used to investigate intramolecular kinase regulation and probe phosphotransferase-independent function. Application of DMS and CystIMATIK to a wide range of kinases could reveal mechanisms of regulation and uncover biological functions.

2.5 METHODS

S. cerevisiae genetics and cell culture

Yeast experiments were performed in BY4741 Green Monster ((Suzuki et al., 2011)a generous gift from Dr. Fritz Roth, DMS experiments) or BY4741 (MATa his3Δ1 leu2Δ0 met15Δ0 ura3Δ0, all other experiments). All Src constructs were cloned into the p415 GAL1 plasmid and transformants were selected for by plating on C-Leu media. All growth experiments were performed in C-Leu media to maintain plasmid.

Mammalian cell culture

Human HEK293s, HEK293Ts, HeLas and murine SYF cells were used for pulldowns and imaging experiments. Authenticity of human cell lines were confirmed by STR analysis, and SYF cells were purchased from ATCC. Cells were maintained in DMEM (Gibco) supplemented with 10% FBS (Gibco). Transient transfections were performed with a 3:1 ratio of μL turbofectin (Origene)/μg DNA.

Cloning

All mutants were generated using either QuikChange Site Directed Mutagenesis (Agilent) or IVA cloning (García-Nafría et al., 2016) following standard protocols. Mutations were verified by Sanger sequencing. All subcloning was achieved using Gibson assembly or directional cloning following standard protocols and validated by Sanger sequencing.

Protein purification and expression

(*Src^{CD}*) For x-ray crystallography, Src^{CD} V284C (residues 261-536) was cloned into the bacterial expression plasmid pET-28a as a N-terminal His_6-Tev tagged construct. The construct was co-transformed (Krishnamurty et al., 2012; Leonard et al., 2014) in *E. coli* with *Yersinia pestis* tyrosine phosphatase YopH (pCDF-Duet-1 vector) and chaperonin GroEL (pACYCDuet-1 vector) and plated on triple selective plates (Kanamycin/Chloramphenicol/Streptomycin). A single colony was picked and grown in an overnight culture of 50 mL of Terrific broth containing all three antibiotics. Three 2 L cultures were then inoculated with the starter culture, grown to an OD_{600} of 1.2, dropped to 18 ºC and protein expression was induced with 0.2 M IPTG. The next day, cells were harvested through centrifugation, lysed by sonication in lysis buffer (50 mM HEPES, pH 8.0, 300 mM NaCl, 1 mM PMSF, 0.1% Triton-X, 20 mM imidazole), and centrifuged for 45 min at 10,000 rpm. Cleared lysates were incubated with 1.5 mL Ni-NTA resin (Thermo) for 1 h. The lysate was then discarded, and beads were washed with 20 mL lysis buffer before bound protein was eluted with lysis buffer containing 300 mM imidazole. Protein was dialyzed overnight at 4 ºC in dialysis buffer (50 mM Tris, pH 8.0, 150 mM NaCl, 5% glycerol, 1 mM DTT) with 1:25 ratio of Tev protease:eluted protein (wt:wt). The next day, the solution was filtered through a 0.22-μm filter then loaded onto a Ni-affinity column (GE Lifescience) and equilibrated with buffer A (50 mM Tris, pH 8.0, 5% glycerol, 1 mM DTT). The loaded column was washed with five column volumes of buffer A, then protein was eluted with a linear gradient of 0-35% of buffer B (50 mM Tris, pH 8.0, 1 M NaCl, 5% glycerol, 1 mM DTT). Peak fractions were analyzed by SDS-PAGE, and fractions containing Src were pooled, and used for crystallization.

(*Src^{FL}, $Src^{\Delta SH4}$, Src^{3D}, Src^{CD}, Hck^{3D}, Fyn^{FL}, and Fyn^{3D}*) For *in vitro* biochemical assays, full length SFK (SFK^{FL}; residues 1-536 for Src, residues 1-537 for Fyn), delta-SH4 ($Src^{\Delta SH4}$; residues 19-536 for Src), three domain (3D) (SFK^{3D}; residues 87-536 for Src, residues 85-537 for Fyn, residues 81-526 for Hck) or catalytic domain (Src^{CD}; residues 261-536) were cloned into the bacterial expression plasmid pMCSG7 as an N-terminal His_6-SUMO tagged constructs (Hck lacked the SUMO tag). SFK constructs were co-transformed in *E.coli* with YopH/GroEL and plated on triple selective plates

(Ampicilin/Chloramphenicol/Streptomycin). A single colony was picked and grown in an overnight culture of 15 mL of Terrific broth containing all three antibiotics. A 1 L culture was then inoculated with the starter culture, grown to an OD_{600} of 1.0, the temperature was then dropped to 18 ºC and protein expression was induced with 0.4 M IPTG. Protein was expressed overnight at 18 ºC. Ni-NTA was used to purify His_6-SUMO-SFK after lysing cells in lysis buffer (50 mM HEPES, pH 8.0, 300 mM NaCl, 1 mM PMSF, 0.1% Triton-X, 20 mM imidazole) and eluted in purification buffer (50 mM HEPES, pH 8.0, 300 mM NaCl, 1 mM PMSF, 0.1% Triton-X, 10% glycerol, 0.2% BME, 100 mM imidazole). A 2 h dialysis in dialysis buffer (50 mM HEPES, pH 8.0, 150 mM NaCl, 1 mM DTT, 10% glycerol) was carried out before the first buffer exchange. 1:25 ratio of His_6-ULP1 protease:eluted protein (wt:wt) was added into the dialysis cassette containing His_6-SUMO-SFK and the mixture was allowed to cleave overnight in fresh dialysis buffer at 4 ºC. Following cleavage, a second Ni-NTA purification was carried out to remove any non-cleaved SFK and His_6-ULP1. Finally, an anion exchange column (Pierce) was used to remove YopH and GroEL to yield SFK at >95% purity.

(*$Src^{TAMRA\text{-}FL}$ and $Src^{TAMRA\text{-}3D}$*) For N-terminal TAMRA labeling, Src was expressed as an N-terminal His6-SUMO construct with one extra glycine N-terminal to Gly2 ($Src^{TAMRA\text{-}FL}$) or two extra glycines added N-terminal to Thr87 ($Src^{TAMRA\text{-}3D}$). 5(6)-Carboxytetramethylrhodamine N-succinimydil ester was conjugated to ε-5-Caproic acid-LPYTGG (GenScript) to generate a rhodamine-labeled Sortase A substrate peptide (Theile et al., 2013). SFKs were expressed and the SUMO-tag was cleaved as described above. After the first dialysis, His6-Ulp1 was added to the dialysis cassette to cleave N-terminal His6-SUMO releasing N-terminal Gly-Gly motif. Anion exchange columns were then used to remove YopH and GroEL. Sortase A (Addgene, #64979), and rhodamine-labeled Sortase A substrate peptide were added to a purified SFK (10 (Sortase A): 10 (Sortase A substrate peptide): 1 (SFK)) and incubated in the dark for 2 h, at 4 ºC in Sortase buffer (50 mM Tris-HCl, pH 7.5, 150 mM NaCl). His_6-Sortase and His6-Ulp1 were removed using Ni-NTA and excess peptide was removed using Zeba desalting columns (Thermo).

(purified *Src^{FLAG} and Hck^{FLAG}*) pcDNA 3.3 containing residues 1-536 of Src (residues 1-526 for Hck) with a C-terminal FLAG (Src^{FLAG} variants WT or E381T) was transiently transfected into HEK293Ts using 3:1 Turbofectin:µg DNA following manufacturer's protocol. Cells were lysed after 24 h in Mod. RIPA buffer 3 (50 mM Tris, pH 7.8, 150 mM NaCl, 1 mM EDTA, 1x Pierce Protease Inhibitor Cocktail (Thermo), 1% IGEPAL CA-630), pelleted, and the supernatant was incubated with 50 nM of YopH and 0.5 mM BME at 4 ºC for 2 h. BME was removed using Zeba Spin

desalting column (Thermo) and the lysate was allowed to bind to Anti-Flag magnetic resin (Sigma) for 4 h at 4 °C. The magnetic bead was washed 3x with Flag purification buffer (50 mM Tris, pH 7.5, 150 mM NaCl, 5% glycerol) and dephosphorylated myristoylated Src was eluted off the resin by treating resin with 3x Flag-peptide (Sigma) diluted in Flag elution buffer (50 mM Tris, pH 7.5, 150 mM NaCl, 5% glycerol, 1mM DTT). Quantitative dephosphorylation was confirmed with a Src pTyr419 antibody (1:2500 Cell Signaling, #2101) and Tyr419 antibody (1:2500 Cell Signaling, #2102).

(*SH4*^{SNAP}) Residues 1-18 from Src were fused to the N-terminus of SNAP-tag through a LPETG linker (SH4^{SNAP}). SH4^{SNAP} (WT, P8N, K5I-P8N) constructs were cloned into the pMCSG7 vector and expressed in BL21 at an OD_{600} of 0.7 with 0.4 M IPTG. The protein was purified using Ni-NTA following the protocol described above using elusion buffer (50 mM HEPES, pH 7.6, 300 mM NaCl, 10% glycerol, 200 mM imidazole) and dialysed into storage buffer (50 mM HEPES, pH 7.6, 150 mM NaCl, 1mM DTT, 10% glycerol).

Csk was expressed and purified as a C-terminal GST tagged protein as described in (Leonard et al., 2014).

Western blotting of yeast and mammalian cell lysates

For yeast protein prep, single colonies of each BY4741 strain were inoculated into 5 mL C-Leu with 2% glucose and grown overnight. The next day, each strain was back diluted into new C-Leu with 2% raffinose, grown for 3 h, then inoculated into C-Leu with 2% galactose. 24 h after induction, 3 OD_{600} units of each culture were collected, spun down, and the resultant pellet was lysed in 200 µL 1x SUMEB buffer (1% SDS, 8 M Urea, pH 6.8, 10 mM MOPS, 10 mM EDTA, 0.01% bromophenol blue, 5% 2-mercaptoethanol) with 1x Protease Inhibitor Cocktail and 200 µL acid washed beads. Each sample was vortexed for 3 min, heated at 65 °C for 10 min, and centrifuged at 17,000x g at 4 °C for 5 min. Protein was quantified using Qubit Protein Assay (Thermo). Samples were run on NuPAGE gels (Invitrogen) in 1x MOPS (Invitrogen) with 7 µL Spectra Multicolor Broad Protein Ladder (Thermo) at 200V for 1 h. Gels were transferred to a PVDF membrane in 1x Transfer buffer (Invitrogen) at 24V and 4 °C for 1 h. All subsequent wash steps were performed 3x in 1x TBST for 5 min while shaking. Membrane was washed and blocked in 5% BSA in 1x TBST for 1 h. Blocked membrane was washed and incubated with a Src antibody (Cell Signaling, #2110), anti-pTyr (Cell Signaling, #9411), or anti-Actin (Abcam, #8224) antibodies at 4 °C overnight. Probed membrane was washed and incubated with anti-Rabbit (1:10000) or anti-Mouse (1:10000)

secondary (Invitrogen) for 1 h. After a final wash, blots were exposed using Super Signal West (Thermo) and developed. Blots were quantified using imageJ.

HEK293T and SYF cells were transfected with the indicated constructs for 24 h, then washed once with 1x PBS and lysed in Mod RIPA buffer 1 (50 mM Tris, pH 8.0, 150 mM NaCl, 1 mM EDTA, 1x Pierce Protease Inhibitor Cocktail (Thermo), 1% IGEPAL CA-630, 2 mM Sodium Orthovanadate, 30 mM Sodium Fluoride). Cells were pelleted at 13,000 g at 4 ºC, then the supernatant was boiled with 3x SDS buffer (240 mM Tris, pH 6.8, 30% glycerol, 3% SDS, 0.01% bromophenol blue, 15% 2-mercaptoethanol) and separated by SDS-PAGE. Samples were visualized by western blotting with a Src antibody (Cell Signaling, #2110) and a Src pTyr419 antibody (Cell Signaling, #2101). After incubation with a secondary antibody, scanned blots were quantified with LI-COR Odyssey software to determine the percent phosphorylation.

HeLa tRex cells were transfected with indicated constructs (in pcDNA5.0 under a doxycycline (Dox) inducible promoter) or blank using Turbofectin:DNA (1:1) for 24 h, and 1 μg/mL of Dox was added to respective wells. The wells were washed once with 1x PBS and lysed in Mod RIPA buffer 1 (50 mM Tris, pH 8.0, 150 mM NaCl, 1 mM EDTA, 1x Pierce Protease Inhibitor Cocktail (Thermo), 1% IGEPAL CA-630, 2 mM Sodium Orthovanadate, 30 mM Sodium Fluoride). Cells were pelleted at 13,000x g at 4 ºC, then the supernatant was boiled with 3x SDS buffer (240 mM Tris, pH 6.8, 30% glycerol, 3% SDS, 0.01% bromophenol blue, 15% 2-mercaptoethanol) and separated by SDS-PAGE. Samples were visualized by western blotting with a Src antibody (Cell Signaling, #2110) and a Src pTyr419 antibody (Cell Signaling, #2101). After incubation with a secondary antibody, scanned blots were quantified with LI-COR Odyssey software to determine the percent phosphorylation.

Inhibitor IC_{50} and K_i determination

For all IC_{50} determination experiments, a kinase titration was performed prior to inhibitor testing in order to ensure that the kinase concentration assayed was in the linear range.

(*Src and Hck*) Src^{3D} WT (7.5 nM), Src^{3D} V284C (7.5 nM), Hck^{3D} WT (5 nM), Hck^{3D} V284C (5 nM), Src^{FL} WT (8 nM), Abl^{3D} WT (15 nM), or Abl^{3D} V284C (24 nM) in assay buffer (76 mM HEPES, pH 7.5, 5 mM $MgCl_2$, 150 mM NaCl, 3.8 mM EGTA, 0.2 mg/mL BSA, 150 uM Na_3VO_4, 1 mM BME) were incubated with inhibitors (initial concentration = 30 μM, 3-fold serial dilutions, 10 data points) and 1 mM ATP for 30 min in a 384-black assay plate (Corning, #3573). 20 μM of a fluorescent SFK peptide (EEEIYGE-(Dap-Pyrene)-EA) or 40 μM of an Abl peptide (AEAIYAA-(Dap-pyrene)-LA) (Wang et al., 2006) was then added to plate and incubated for 2 h. Raw fluorescence units were

measured on an Envision plate reader (Perkin Elmer) with an excitation wavelength of 344 nm and an emission wavelength of 405 nm. Data was analyzed using GraphPad Prism software, and IC_{50} values were determined using "One-site fit logIC_{50}" option. All IC_{50} values were then converted to K_i by implementing the Cheng-Prusoff equation using the ATP K_m determined for each kinase and 1 mM ATP in case of SFKs; Ki is equal to IC_{50} for EphA2 and Rsk2. All assays were performed in triplicate

Kinobead profiling experiments

SILAC cell culture and generation of HEK293 lysate containing Hck^{FLAG} V284C

Hck^{FLAG} V284C was integrated into the Flp-In T-REx system (Thermo) as described in the product documentation and maintained with 50 µg/mL hygromycin after selection. Flp-In T-REx HEK293 cells stably expressing Hck^{FLAG} V284C were grown in custom -Lys/-Arg DMEM (Caisson Labs) supplemented with 10% dFBS (Sigma), 200 µg/ml proline and SILAC amino acids (0.2 mM natural isotope abundance Lys/Arg for light label, 0.2 mM Lys8/Arg10 for heavy label; Cambridge Isotope Labs). Cells were grown for at least 5 cell doublings in SILAC medium and harvested after reaching 90% confluency and 24 h induction with 0.5 mg/mL dox. For harvesting, cells were rinsed twice with ice cold PBS and lysed in 750 µL of mod. RIPA buffer 2 (50 mM Tris, pH 7.8, 150 mM NaCL, 10 mM NaF, 0.25% Na-deoxycholate, 1% NP-40 and 5% glycerol containing Halt Protease Inhibitor Cocktail (100x, Thermo Scientific), and Phosphatase inhibitor cocktail 2 and 3 (Sigma)). The ice-cold lysate was vortexed five times intermittently for 3 s and clarified by centrifugation at 21,000xg and 4 °C for 20 min. The protein content of the samples was determined using the Pierce 660 nm Assay Reagent (Thermo), then snap frozen in liquid nitrogen and stored at -80 °C until used(Golkowski et al., 2017).

CystIMATIK probe profiling experiments

CystIMATIK probe profiling experiments were performed with a modified Kinobead profiling method (Golkowski et al., 2017). Briefly, 10 µL of a 50% Kinobead slurry (Kinobead matrix described in (Golkowski et al., 2017)) in 20% aqueous ethanol was pipetted into a 1.5 mL microtube and washed twice with 100 µL of mod. RIPA buffer 2. In parallel, 300 µg of cell extract in mod. RIPA buffer (ca. 2 mg/ml protein concentration) from either light or heavy labeled cells was pipetted into a 1.5 mL micro tube for each pulldown. Each CystIMATIK probe in DMSO (10 µM final concentration) or pure DMSO (control) was added to the corresponding SILAC lysate (1%

DMSO final) and the tubes were agitated at 4 °C for 20 min on a rotator. For the SILAC label swap experiments, the addition of CystIMATIK probe to, for example, the light lysate was switched to heavy lysate, and addition of the DMSO control to the heavy lysate was switched to light lysate. After incubation, the pretreated lysate was pipetted individually to the tubes containing Kinobead affinity resin and the slurry was agitated on a rotator for 3 h at 4 °C. The supernatant was removed, and the beads were washed twice with 100 µL of ice cold mod. RIPA buffer. Then the beads were re-suspended in 100 µL of ice cold TBS (50 mM Tris-HCl, pH 7.8, 150 mM NaCl), the SILAC samples (beads) were combined pairwise (competition and control experiments) and the supernatant was removed. The beads were washed twice more with TBS and then re-suspended in 25 µL of 8 M tris buffered urea (8 M urea, 50 mM Tris-HCl, pH 7.8) containing 5 mM *tris*-(2-carboxyethyl)phosphine (TCEP) and 10 mM 2-chloroacetamide (CAM). The bead slurry was agitated for 30 min at 37 °C and 1400 rpm on a thermomixer. For digestion, the slurry was diluted two-fold with 100 mM aqueous triethylammonium bicarbonate solution (TEAB, urea concentration ≤4 M), the pH was adjusted to 9 with 1 N NaOH and 0.4 µg of LysC was added for every 5 uL of settled affinity resin that was added. The slurry was shaken for 2 h at 1400 rpm and 37 °C. Then the slurry was further diluted 2-fold with 100 mM TEAB (urea concentration ≤ 2 M) and 1 µg of trypsin per 5 µl of affinity resin was added. Samples were digested overnight on a shaker at 37 °C, diluted two-fold with 5% aqueous acetonitrile containing 0.1% TFA and acidified with formic acid (1% final). Peptides were extracted using StageTips (Rappsilber et al., 2007) and then analyzed in single nanoLC- MS/MS runs.

LC-MS/MS and data analysis

Peptides were separated on a Thermo-Dionex RSLCNano UHPLC instrument with 10 cm fused silica capillary columns made in-house with a laser puller (Sutter) and packed with 3 µm 120 Å reversed phase C18 beads (a gift from Dr. Maisch, Ammerbuch, DE). The LC gradient was 90 min long with 10-35% Buffer B at 200 nL/min. LC solvent A was 0.1% acetic acid and LC solvent B was 0.1% acetic acid, 99.9% ACN. MS data was collected with a Thermo Orbitrap Elite spectrometer. Data-dependent analysis was applied using Top15 selection with CID fragmentation. Raw files were analyzed by MaxQuant/Andromeda (Golkowski et al., 2017) version 1.5.2.8 using protein, peptide and site FDRs of 0.01 and a score minimum of 40 for modified peptides, 0 for unmodified peptides; delta score minimum of 17 for modified peptides, 0 for unmodified peptides. MS/MS spectra were searched against the UniProt human database (updated July 22nd, 2015). MaxQuant search

parameters: Variable modifications included Oxidation (M). Carbamidomethyl (C) was a fixed modification. Max. labeled amino acids was 3, max. missed cleavages was 2, enzyme was Trypsin/P, max charge was 7, multiplicity was either 1, 2 or 3, SILAC labels were Arg0/Lys0 (light), Arg6/Lys4 (medium), Arg10/Lys8 (heavy). The MaxQuant Re- Quantification feature was enabled. The initial search tolerance for FTMS scans was 20 ppm and 0.5 Da for ITMS MS/MS scans. Data was further processed using the Perseus software package (version 1.5.2.6), the R environment, Origin Pro 8.0 and Microsoft Excel. Significantly competed kinases were determined by applying a moderated two-tailed, two-sample t-test in Perseus with an FDR of 0.05.

X-ray crystallography data acquisition and processing

A 20 mM stock solution of inhibitor **1**, **2**, or **3** (in 100% DMSO) was added to purified Src^{CD} V284C (5 mg/mL) to a final concentration of 75 μM. This mixture was incubated on ice for 1 h and spun down to remove insoluble compound prior to setting up the crystallization experiment. Crystals were grown at room temperature by vapor diffusion from a sitting drop containing 1 μL Src V284C-**1**, **2**, or **3** solution (5 mg/mL protein, 100 mM NaCl, 5% glycerol, 1 mM DTT, 25 mM Tris, pH 8.0, 2 mM inhibitor, 10% DMSO) plus 1 μL crystallization buffer (**1**: 100mM MES, pH 6.0, 8% PEG 3350, 3% glycerol, 10 mM DTT, 10 mM NaOAc, **2**: 100 mM MES, pH 6.3, 40 mM NaOAc, 8% PEG3350, 10% glycerol, 10 mM DTT, **3**: 100 mM MES pH 6.0, 8% PEG 3350, 10 mM NaOAc, 14% glycerol, 10 mM DTT). Diffraction images were measured at SSRL Beamline BL9-2 at an X-ray wavelength of 0.9795 Å and processed using Mosflm and the CCP4 program suite. The initial structural models were taken from PDB entry 3UQF for Src-**1**, 5SWH for Src-**2**, and 3G6G for Src-**3** and refined using alternating rounds of manual fitting in Coot and automated refinement in Refmac. Model geometry was validated using Molprobity. The final models have been deposited with the PDB as entry 5SWH (Src-**1**), 5TEH (Src-**2**), and 5SYS (Src-**3**).

Yeast growth assay

To confirm that Src expression affects growth when expressed in *S. cerevisiae*, codon-optimized full-length human Src^{myr} (Blue Heron Biotech) and indicated mutants were transformed into the *S. cerevisiae* BY4741 strain using standard LiAc transformation protocols (Gietz and Schiestl, 2007) and plated on C-Leu plates to select for successful transformants. Three independent colonies for each strain were collected and treated as biological replicates. Single colonies for each strain were grown overnight in 5 mL of 3% raffinose C-Leu to saturation. Strains were back diluted and allowed to

double at least once, then 150 µL of each strain were plated in biological replicates and grown in a BioTek Synergy plate reader under constant shaking at 30 ºC. OD_{600} was measured every 30 min over a 48 h time period. Growth rates of each strain were calculated using the GrowthRates software (Hall et al., 2013) using the BioTek plate readers option.

Src catalytic domain mutant library creation

All subsequent cleaning steps were performed using the Clean & Concentrate kit (Zymogen). To generate a mutant library of Src catalytic domain variants, we employed an inverse PCR saturation mutagenesis strategy (Jain *et al.* 2013). Briefly, we designed primer pairs corresponding to each of the 250 positions that comprise Src's catalytic domain in p415 GAL1 Src. For each position, the forward primer contained a degenerate 'NNK' codon corresponding to that position, where "N" represents any possible nucleotide while "K" represents a "G" or "T". The reverse primer sits immediately upstream to the forward primer. Primer pairs were melting temperature and GC-content matched and ordered in 96-well format (Integrated DNA Technologies). For amplification of each position, 10 µL 2x KAPA HiFI HotStart ReadyMix (KAPA Biosystems), 2 µL of both 2.5 µM forward and reverse primers for that position, 5 µL H_2O, and 1 µL 500 pg/µL p415 GAL1 Src. Thermocycler conditions used were: Initial denaturation at 95 ºC for 3 min, followed by 20 cycles of 98 ºC for 20 s, 60 ºC for 15 s, and 72 ºC for 8.5 min, and ending with a final extension at 72 ºC for 10 min. ~90% of all positions were successfully amplified using these conditions, with the remaining positions requiring various PCR optimizations. 5 µL of each reaction was run on an agarose gel to verify correct amplification. Once confirmed, band intensities were quantified using the ImageJ software (https://imagej.nih.gov/ij/) and compared to a standard curve of intensities from known DNA concentrations. Based on measured intensities, each position was binned and pooled. After pooling, the linearized variant library was 5`phosphorylated by incubating with T4 Polynucleotide Kinase at 37 ºC for 30 min, followed by a heat inactivation step at 65 ºC for 20 min. This product was then ligated to re-circularize the vector with T4 DNA Ligase at 16 ºC overnight, cleaned, and transformed by electroporation into One Shot TOP10F Electrocomp *E. coli* (Thermo) according to manufacturer's protocol. Transformed cells were plated on LB + Ampicillin plates to determine library size and inoculated into LB + Ampicillin liquid and prepped using GenElute Midiprep Kit (Sigma).

Subassembly of Src variant library

Subassembly of variant library was performed following a previous protocol(Hiatt et al., 2010). The barcode oligo (EA01) was made double stranded by mixing 4.5 µL 25 µM EA01, 4.5 µL 25 µM EA02, 4 µL Buffer 3.1 and 27 µL H_2O. This reaction was heated at 98 ºC for 3 min, ramped down to 25 ºC at a rate of 0.1 ºC/s and then 1 µL of DNA Polymerase I, Large Fragment and 1.35 µL of 1 mM dNTPS (Qiagen) were added and incubated at 25 ºC for 15 min. The now double stranded barcode was cleaned using and eluted in 10 µl H_2O. In parallel, 10 µL of the plasmid-encoded Src variant library (268 ng/µL) was digested in 5 µL 10x Cutsmart Buffer, 1 µL SalI-HF, and 34 µL H_2O overnight at 37 ºC. The digested vector was treated with 5 µl 10x Antarctic Phosphatase Buffer and 1 µl Antarctic Phosphatase for 1 h at 37 ºC, heat inactivated for 5 min at 70 ºC, gel extracted (Qiagen), then cleaned and eluted in 10 µl H_2O. 100 ng of vector and 150 ng of barcode were incubated with 2x Gibson Mastermix for 1 h at 50 ºC, then cleaned and transformed into *E. coli* as above. Multiple gibsons were transformed in parallel to enable bottlenecking at a desired library size. A library corresponding to ~100,000 colonies was chosen for all future steps (henceforth referred to as Src CD library). A region encompassing Src's catalytic domain and barcode was amplified using 25 µL 2x KAPA HiFI HotStart ReadyMix, 6 µL 2.5 µM EA03, 6 µL 2.5 µM EA04, 12 µL H_2O, and 1 µL 10 ng/µL BC Src library, with 8 replicates for each of the three Bal-31 digestion conditions. Thermocycler conditions used were: Initial denaturation at 95 ºC for 3 min, followed by 17 cycles of 98 ºC for 20 s, 60 ºC for 15 s, and 72 ºC for 4.5 min. Eight replicates were pooled and cleaned. To generate fragments spanning the mutagenized region of Src's catalytic domain, three different Bal-31 digestion conditions were performed: undigested, Bal-31 30 min, and ScaI/Bal-31 10 min. For the ScaI/Bal-31 10 min condition, 20 µL of amplicon, 5 µL 10x CutSmart buffer, 24 µL H_2O, and 1 µL ScaI-HF was incubated overnight at 37 ºC and subsequently cleaned. Each sample was digested using the endonuclease Bal-31 using 25 µL 2x Bal-31 Buffer, enough DNA for 40 ng/µL final concentration, and 1 µL of 1:5 Bal-31 enzyme at 25 ºC for the indicated time. The digestion was stopped by adding 10 µL 100 mM EGTA and heating to 65 ºC for 10 min. The digested DNA was cleaned and was run on a gel for visual conformation of fragment range. Each reaction was treated with END-IT Kit (Epicentre), cleaned, and A-tailed by adding the entire reaction to 5 µL 10x Taq Buffer, 8 µL H_2O, 1 µL 10 mM ATP, and 1 µL GoTaq for 30 min at 72 ºC then cooled down to 25 ºC. Subassembly adapter was generated by mixing 10 µL of 100 µM EA05, 10 µL of 100 µM EA06, and 40 µL H_2O, heating to 95 ºC, then ramping down to 25 ºC at 0.1ºC/sec. Subassembly adapter

was then ligated to cleaned DNA from above at a 3:1 Adapter:Amplicon ratio using T4 DNA ligase for 20 min at 25 ºC, then heat inactivated for 10 min at 65 ºC. Standard Illumina cluster generators were appended to ligated products by 25 µL KAPA HiFI HotStart ReadyMix, 1 µL 10 µM EA07, 1 µL 10 µM EA08, 21 µL H_2O, and 2 µL 2 ng/µL respective template. Thermocycler conditions used were: Initial denaturation at 95 ºC for 3 min, followed by 17 cycles of 98 ºC for 20 s, 62.4 ºC for 30 s, and 72 ºC for 1 min. Cluster-forming amplicons were quantified using KAPA Library Quantification Kit (Kapa Biosystems). Paired end MiSeq 300bp kit (Illumina) using both the standard primers and a custom sequencing primer EA09 was used to sequence both the barcode and coding regions of each Src variant. All reads sharing a common barcode sequence were collapsed to form the consensus variant sequence, resulting in 72,822, barcodes, of which 31,728 contained "N"s, leaving 41,094 barcodes passing initial filter (Fowler et al., 2011; Starita et al., 2015). We then applied a quality filter to these remaining barcodes, wherein every base needed >=5x reads in agreement, leaving 25,390 high quality subassembled barcodes. These 25,390 barcodes represent 70% of all possible single amino acid mutants of the Src kinase domain, with an average of ~5 barcodes per variant.

Src library transformation into yeast

A single colony of freshly streaked BY4741 Green Monster was picked and grown in 5 mL of 2x YPAD (4% Peptone, 2% Bacto Dehydrated Yeast Extract, 0.008% Adenine sulfate, 2% glucose) overnight. The following morning, the saturated culture was backdiluted into 50 mL of 2x YPAD at an initial OD_{600} of 0.3 and grown until reaching an OD_{600} of ~2. The entire culture was centrifuged at 3,000 xg for 5 min and the resultant pellet was washed in 25 mL sterile H_2O. This wash step was repeated twice. Pellet was resuspended in 1 mL sterile H_2O, aliquoted equally into 10 eppendorf tubes, and spun down at 17,000G for 30 s to pellet. Each pellet was resuspended in transformation mix consisting of 240 µL 50% PEG, 50 µL 2 mg/mL Salmon Sperm (Invitrogen), 36 uL 1M LiAc. Eight of the samples had 500 ng BC Src library added, one had 250 ng BC Src library and 250 ng pRS411 added, and one received H_2O vehicle. All samples were incubated at 42 ºC for 45 min then washed in 1 mL sterile H_2O. The eight 500 ng BC Src library tubes were pooled, added to 50 mL C-Leu 2% glucose and grown shaking at 30 ºC. Serial dilutions of this culture were plated on C-Leu plates to enumerate library size, while dilutions of the BC Src/pRS411 condition were plated on C-

Leu/Met plates to enumerate percent of double transformants. After 72 h of growth, aliquots of library were frozen in 20% glycerol at -80ºC.

Selection & sequencing

Aliquots of frozen library were thawed and grown overnight in C-Leu 3% raffinose media. The next morning, cultures were back diluted to 0.5 OD_{600} in C-Leu 3% raffinose and grown for an additional doubling. Selection was initiated by inoculation at a final OD_{600} of 0.01 into 200 mL C-Leu 2% galactose media. Growth was monitored throughout the selection by measuring OD_{600}. Selection 1 timepoints were OD_{600}s: 0.164, 0.626, and 3.26. Selection 2 timepoints were OD_{600}s: 0.239, 0.657, and 2.37. 4 OD_{600} units of each time point were harvested, spun down at 3,000G for 5 min, and immediately stored at -80 ºC. Plasmids were extracted from frozen pellets using Yeast Plasmid Prep I (Zymogen) according to manufacturer's protocol and resuspended in 15 µL H_2O. To append Illumina cluster generators and append indices, 25 µL 2x KAPA2G Robust HotStart ReadyMix (KAPA Biosystems), 2 µL 10 µM EA10-EA12 (indexing primers), 2 µL 10 µM EA13-EA17 (indexing primers), 13.5 µL H_2O, and 7.5 µL extracted plasmid. Thermocycler conditions used were: Initial denaturation at 95ºC for 3 min, followed by 17 cycles of 95ºC for 15s, 60ºC for 15s, and 72ºC for 15s. Each amplification was cleaned, quantified using KAPA Library Quantification Kit, then sequenced on NextSeq 500/550 High Output v2 kit (75 cycles) with standard Illumina sequencing primers and the custom primers EA18 and EA19.

Src variant library analysis

Raw Illumina reads were processed and demultiplexed using bcl2fastq and ea-utils. Functional scores for Src variants were calculated using Enrich2(Rubin et al., 2017) using Barcoded Variant SeqLib with "Weighted Least Squares" scoring option and "Wild Type" normalization. The OD_{600} readings of each sample (multiplied by 100, see "Selection & Sequencing") were used as timepoints. The barcode map from subassembly step was used, with additional filtering of WT-associated barcodes (using 2x Std. Dev. of mean WT barcode activity score as a cutoff to filter out aberrantly-acting WT barcodes) and spiking in of barcoded variants Src K298M and T341I to ensure adequate representation of controls.

SH4 domain DMS

The SH4 domain mutant library was generated following a modified mutagenesis protocol(García-Nafría et al., 2016). For amplification of each position, 15 µL 2x KAPA HiFI HotStart ReadyMix, 0.9 µL of 10 µM mix of primers for that position (**Table S6,** sequences labeled with SH4), 10.1 µL H_2O, and 4 µL 10 ng/ µL p415 GAL1 Src. Thermocycler conditions used were: Initial denaturation at 95 ºC for 3 min, followed by 7 cycles of 98 ºC for 20 s, 60 ºC for 15 s, and 72 ºC for 9 min, and ending with a final extension at 72 ºC for 9 min. After amplification, 0.6 µL of DpnI was added and incubated at 37 ºC for 1 h. Each product was cleaned and transformed into 10-beta electrocompetent cells (New England Biolabs) following manufacturer's protocol. Transformed cells were plated on LB + Ampicillin plates to determine library size and inoculated into LB + Ampicillin liquid. This library (henceforth refered to as Src SH4 library) was transformed into yeast and grown as described for the Src CD library. Two independent transformations were performed, Selection 1 timepoints were OD_{600}s: 0.156, 0.671, and 2.29. Selection 2 timepoints were OD_{600}s: 0.171, 0.653, and 2.23. Plasmids were extracted and indexed as described for the Src CD library, except EA20 and EA21-EA28 were used. Amplicons were sequenced on NextSeq 500/550 High Output v2 kit (150 cycles) with custom primers EA29-EA32. Sequencing reads were processed and functional scores calculated as described for Src CD library, except the reads were paired using PEAR and the Basic SeqLib option was used.

Rosetta modeling of N-tail conformation

We used the Rosetta Comparative Modeling protocol (Song et al., 2013)to model conformations of Src's N-terminal tail (residues 2-86). A starting model of residues 87-536 created by running the Rosetta FastRelax protocol on the pdb structure 2SRC and threading the full sequence from residues 2-536 onto this structure. 3,798 models were generated using Rosetta@home (R@h; http://boinc.bakerlab.org/rosetta). Each final model was relaxed again using FastRelax to obtain the final score and conformation. Each output structure was analyzed using Pymol. Cα-Cα distances were calculated between tail residues (2-86) and all other residues. Cα-Cα distances < 8 Å are tabulated as a contact between residues. The Rosetta relaxed 2SRC structure was used to extract structural features of the kinase domain. Solvent accessible surface area of each residue was calculated using DSSP and the ratio of solvent accessible surface area to total surface area (rSASA) was calculated with respect to the theoretical surface areas(Tien et al., 2013).

Phylogenetic analysis

Amino acid sequences for all aligned proteins were obtained from Uniprot and aligned using the MEGA software with the Muscle algorithm.

Kinase activity assay

Activity of purified Src variants were measured using a self-reporting fluorescence SFK peptide (EEEIYGE-(DAP-Pyrene)-EA) in an *in vitro* kinase assay. Briefly, purified Src^{FL}, Src^{3D}, or $Src^{\Delta SH4}$ constructs of each variant (WT, E381T, I444K) were diluted in kinase reaction buffer (76 mM HEPES, pH 7.5, 5 mM $MgCl_2$, 150 mM NaCl, 3.8 mM EGTA, 0.2 mg/mL BSA, 150 uM Na_3VO_4) and incubated with 1 mM ATP at room temperature for 30 min to ensure full conversion of kinase to phosphorylated species. 60 nmoles of SFK peptide was pipetted to respective wells and raw fluorescence units were measured immediately on Envision (Perkin Elmer) with excitation wavelength of 344 nm and emission wavelength of 405 nm in real time for the first 10 min. Calculation of kinase activity in terms of pmole sec^{-1} of phosphorylated substrate is discussed below under "Calculation of Src kinase substrate phosphorylation rates".

SH3 domain pulldown assays

Generation of immobilized SH3 domain ligand: 20 μL of a 50% slurry of SNAP-capture pulldown resin was placed in a micro-centrifuge tube. The resin was washed (3x, 10 bead volumes) with pulldown buffer (20 mM Tris-HCl, pH 7.5, 100 mM NaCl, 1 mM DTT and 0.2 mg/mL BSA). 8 μM of SNAP tag–polyproline peptide fusion (VSLARRPLPPLP) was loaded onto the resin at a final volume of 50 μL per 10 μL of bead in pulldown buffer (Leonard et al., 2014)**.** The resin was rotated at room temperature for 1 h and then washed (3x, 10 bead volumes) prior to performing pulldown assays.

SH3 pull down assays performed with *apo* SFKs: *apo* SFK (100 nM) in 50 μL of pulldown buffer was incubated with 10 μL of the immobilized SH3 domain ligand. The resin was rotated at room temperature for 1 h. Post incubation, the flow-through was collected, and the resin was washed (3x, 10 bead volumes). To elute the retained kinase, 50 μL of 1x SDS loading buffer was added and the beads were boiled at 95 °C for 10 min. All samples were separated via SDS–PAGE and visualized using Western blotting using Src (1:2500; in case of Figures 3D-E, S2C, S2D, 6E, and S5H-J), or Tyr-419 (in case of 7C and S6B). (Cell Signaling, #2110 for Src^{FL} constructs or Cell Signaling, #2109 for Src^{3D} constructs). The loaded amount of kinase was diluted to one fourth of the original concentration using 1x loading dye before running it on the gel as "I" (Input) along with the kinase

eluted ("E") off the resin. The scanned blots were quantified with ImageStudio Lite software and signal corresponding to input protein was scaled to original loaded kinase amount. The percentage of kinase retained on the resin (% retained) was then calculated on the basis of the loaded and eluted fraction based on curve fitting of immunoblot signal intensity to a Src titration.

SH3 pull down assays performed with purified inhibitor-SFKs complexes: Purified Src^{3D} V284C (100 nM) was diluted in pulldown buffer. 3 or 5 μM of CystIMATIK probes **1**, **2**, or **3** was added to make a kinase-inhibitor complex. The mixture was incubated for 30 min at room temperature before being added to 10 μL of the immobilized SH3 domain ligand. Pulldown and quantification (with an anti-Src antibody) were performed as described above (Pull down assays with *apo* SFKs). Inhibitor complexes of $Src^{TAMRA\text{-}3D}$ V284C (50 nM, Figure S3D) were generated as described above and pulldowns were performed as described above. Quantification was performed with fluorescent gel scanning (using RITC filter on GE Typhoon FLA 900).

SH3 pull down assays performed with inhibitor-treated cells: HEK293Ts expressing Src^{FLAG} V284C or Hck^{FLAG} WT or V284C were treated with 10 μM CystIMATIK probes **1**, **2**, or **3** for 2 h before removal of media, 1x PBS wash, and lysis in 100 μL Mod. RIPA buffer (10 μM **1**, **2**, or **3**, 50 mM Tris-HCL, pH 7.8 150 mM NaCl, 1% IGEPAL-630, 1 mM EDTA, 1x Pierce Protease Inhibitor Tablet (Pierce), and 1x Pierce Phosphatase Inhibitor tablet (Pierce) for 20 min on ice before clarification by centrifugation 17,000x g at 4 °C. Clarified lysate was added to 10 μL of the immobilized SH3 domain ligand and pulldown and quantification (with an anti-FLAG antibody) was performed as described above (Pull down assays with *apo* SFKs).

SH4 domain pulldown assay

For data shown in Figure 2.10, 10 μL of a 50% slurry of SNAP-capture pulldown resin was placed in a micro-centrifuge tube. The resin was washed (3x, 10 bead volumes) with pulldown buffer (20 mM Tris, pH 7.0, 300 mM NaCl, 1mM BME, 0.2 mg/mL BSA). 5 μM (in case of Figure 6J) or 10 μM (in case of Figure 6K) of $SH4^{SNAP}$ was loaded onto the resin at a final volume of 50 μL per 10 μL bead volume in pulldown buffer. The resin was rotated at room temperature for 1 h and then washed (3x, 10 bead volumes) prior to performing pulldown assays. Next 75 nM of Src^{CD} (WT or mutants) was added to the resin to a final volume of 50 μL and incubated for 1 h at room temperature. The resin was then washed (3x, 10 bead volumes) with pulldown buffer described above and protein bound to the resin was eluted with 50 μL 1x loading dye and bead was boiled at 95 °C for 10 min. All samples were separated via SDS–PAGE and visualized using Western blotting using anti-Src (1:2500; Cell

Signaling Technology #2109). For data shown in Figure S5I, pulldown was performed with 25 nM TAMRA-Src^{FL} V284C pre-treated with 5 μM of inhibitors **1**, **2** or **3** for 30 min in buffer (20 mM Tris, pH 7.5, 100 mM NaCl, 1 mM 2-mercaptoethanol, 0.2 mg/mL BSA) before incubating kinase-inhibitor complex with 2.5 μM of SH4^{Snap} protein conjugated to SNAP-capture pulldown resin. The resin was then washed (3x, 10 bead volumes) with pulldown buffer described above and protein bound to the resin was eluted with 50 μL 1x loading dye and bead was boiled at 95 °C for 10 min. All samples were separated via SDS–PAGE and visualized using RITC filter on GE Typhoon FLA 900.

For data shown in Figure 2.12, 10 μL of a 50% slurry of SNAP-capture pulldown resin was placed in a micro-centrifuge tube. The resin was washed (3x, 10 bead volumes) with pulldown buffer (20 mM Tris, pH 7.5, 100 mM NaCl, 1 mM 2-mercaptoethanol, 0.2 mg/mL BSA). 2.5 μM of SH4^{SNAP} (WT or P8N or P8N/K5I) was loaded onto the resin at a final volume of 50 μL per 10 μL bead volume in pulldown buffer. The resin was rotated at room temperature for 1 h and then washed (3x, 10 bead volumes) prior to performing pulldown assays with *apo*-Src$^{TAMRA-3D}$ WT (50 nM) as described above (SH4 domain pull down assays performed with *apo* SFKs). Quantification was performed with fluorescent gel scanning (using RITC filter on GE Typhoon FLA 900).

C-terminal Src kinase (Csk) accessibility assay

Csk was first profiled against CystIMATIK probes (**2** and **3**) using Csk peptide substrate (Csktide, KKKKEEIYFFFG) and γ^{32}P-ATP. 25 nM of Csk was incubated with CystIMATIK probes (initial concentration = 10 μM, 3-fold serial dilutions, 10 data points) and 100 μM of ATP for 30 min in kinase reaction buffer (76 mM HEPES, pH 8.0, 5 mM $MgCl_2$, 150 mM NaCl, 0.2 mg/mL BSA, 250 μM Na_3VO_4, and 1 mM DTT, 3.8 mM EGTA). 20 μM of Csktide and γ^{32}P-ATP (0.08 μCi/well) were added and reaction was incubated for 1 h, then 4.6 μL of this reaction was spotted on a phosphocellulose membrane. Membranes were washed with 0.5% phosphoric acid (3x, 10 min each wash) and dried, and the radioactivity was determined by phosphor-imaging with a GE Typhoon FLA 9000 phosphor-scanner. The scanned membranes were quantified using ImageStudio Lite and plotted using GraphPad prism to determine % activity of Csk at different concentrations of inhibitors.

Titrations of SFK^{3D} V284C starting at 1600 nM (2-fold serial dilutions) were incubated with 5 μM of **2** or **3** (SFK^{3D} V284C was >98% inhibitor bound) with kinase reaction buffer. Following a 1 h incubation at room temperature, 25 nM Csk was added and phosphorylation was initiated by the

addition of γ^{32}P-ATP (0.08 μCi/well) and 100 μM of cold ATP at a final volume of 30 μL. The enzymatic reaction was run at room temperature for 1 h and then terminated by spotting 4.6 μL of the reaction mixture onto a phosphocellulose membrane. Membranes were washed with 0.05% phosphoric acid (3x 10 min wash) and air-dried, and the radioactivity was determined by phosphor-imaging with a GE Typhoon FLA 9000 phosphor-scanner. The scanned membranes were quantified with ImageStudioLite, and data were analyzed using GraphPad Prism and counts per minute was determined by dividing the raw counts over duration of the reaction.

Co-Sedimentation assays

Generation of liposomes: For liposome co-sedimentation assay, sucrose loaded vesicles (1:1:1 phosphatidylcholine, phosphatidylserine and phosphatidylethanolamine (PC:PS:PE) or 2:1 PC and PS (2PC:PS)) were prepared as described previously (Giorgione and Newton, 2003).

Co-sedimentation of apo SFKs: Src^{FLAG} WT or E381T (150 nM) in co-sedimentation buffer (120 mM KCl, 6 mM $MgCl_2$, 24 mM HEPES, pH 7.6, 1 mM DTT and 0.3 mg/mL BSA) was spun in a polycarbonate ultracentrifuge tube at 50,000 rpm at 4 °C for 10 min. Supernatant was removed and Src^{FLAG} was then incubated with 200 μM liposome at room temperature for 30 min before spinning the mixture at 100,000 rpm for 20 min. Supernatant was carefully removed and treated with 3x SDS loading dye, this served as the soluble fraction ("S"). The pelleted Src ("P") was boiled with 1x SDS loading dye at 95 °C for 10 min. All samples were separated via SDS-PAGE and visualized by Western blotting using an anti-Src antibody (1:2500, Cell Signaling Technology #2110). The scanned blots were quantified with LI-COR Odyssey software to determine the percentage of kinase pelleted with liposomes on the basis of pelleted and soluble Src based on curve fitting of immunoblot signal intensity to a Src titration.

Co-sedimentation of inhibitor SFK complexes: Src^{FLAG} WT (150 nM) in co-sedimentation buffer was spun in a polycarbonate ultracentrifuge tube at 50,000 rpm at 4 °C for 10 min. The soluble Src^{FLAG} WT was then incubated with DMSO or 5 μM inhibitors **4**, **5**, or **6** at room temperature for 30 min. The kinase-inhibitor complex was then added to 200 □ M liposome and co-sedimentation assay was performed and quantified as described above (Co-sedimentation of *apo* SFKs).

Microscopy

SYF cells were plated on 18 mm glass slides (Fisher) in a 12-well tissue culture plate at a density of $2x10^4$. 24 h after plating, cells were transfected with a 3:1 ratio of μL turbofectin:μg DNA following

manufacturer's instructions. For untreated SYFs, 24 h after transfection the cells were washed once with PBS and fixed with a 4% paraformaldehyde mixture in PBS (Electron Microscopy Sciences) for 15 min. After fixing, cells were stained with NucBlue (Thermo) and Wheat-germ agglutinin conjugated to Alexafluor647 (Thermo) for 15 min.

SYF cells treated with CystIMATIK probes: SYFs were treated 24 h post-transfection with 10 μM **1**, 3 μM **2** or 10 μM **3** unless otherwise noted (Figure 5C: treated with 1, 3, or 10 μM of **3**) for 15 min (except where otherwise noted, as in Figures 5B and S4C). For cells treated with both **2** and **3**, cells were treated with 3 μM **2** for 15 min, then 10 μM **3** for 15 min . Cells treated with Rock Inhibitor GSK429286A (Selleck Chem) were treated with 10 μM of the inhibitor for 2 h, then with 10 μM **3** for 15 min. After treatment, cells were then washed once with PBS and fixed with a 4% paraformaldehyde mixture in PBS (Electron Microscopy Sciences) for 15 min. After fixing, cells were stained with NucBlue (Thermo) and Wheat-germ agglutinin conjugated to Alexafluor647 (Thermo) for 15 min.

HeLa cells treated with CystIMATIK probes: Flp-In T-Rex HeLa cells (gift from Stephen Taylor (Tighe et al., 2008)) stably expressing Src^{myr} or Src^{myr} V284C were plated on 18 mm glass slides (Fisher) in a 12-well tissue culture plate at a density of $2x10^4$ with 1 μg/mL doxycycline. After 48 h, cells were treated with 5 μM **3b**, an analog of **3** which differs by a methyl group **2** followed by **3b** (same as described for SYFs), or Rock inhibitor GSK429286A followed by 5 μM **3b** (same as described for SYFs). After inhibitor treatment, cells were washed once with 1x PBS and fixed with a 4% paraformaldehyde mixture in 1x PBS for 15 min, followed by incubation with 250 μL of PBS containing NucBlue, Wheat-germ agglutinin conjugated to Alexafluor694 (Thermo) in the dark for 5 min.

For blebbing quantification of both SYF and HeLa fixed cells, slides were washed twice with 1x PBS, then mounted using Fluormount G (Southern Biotechnology) onto microscopy slides and sealed with nail polish. Images were obtained on a Leica SP8X, and images were processed using imageJ. Randomized images were scored by an unbiased scorer as either blebbing or not blebbing after viewing a training set of blebbing or non-blebbing cells for each condition. Cells were scored if they contained a single nucleus, had an intact and continuous membrane, and the majority of the cell was in the image. A cell was considered to be blebbing if it contained 3 or more rounded membrane protrusions. All images, as well as training sets and a master image list have been uploaded to Mendeley Data. Replicates consist of images from a single slide, and 2120 total cells were scored. All microscopy images were brightened for clarity.

Src autophosphorylation assay

Src^{FL} WT and E381T and $Src^{\Delta SH4}$ WT and E381T were purified in their dephosphorylated form. 160 µL kinase reaction mixture was prepared by adding Src constructs (final Src concentration = 50 nM) in kinase reaction buffer (76 mM HEPES, pH 7.5, 5 mM MgCl2, 150 mM NaCl, 3.8 mM EGTA, 0.2 mg/mL BSA, 150 uM Na_3VO_4). 32 µL of this was added to 3x loading dye for a 0 min timepoint sample. To initiate the autophosphorylation reaction, 30 µM ATP was then added to the rest 128 µL kinase reaction mixture and at various timepoints, the reaction was stopped by adding an aliquot of the reaction to 3x loading dye. Samples from 0, 5, 10 and 20 min were run on a SDS-PAGE gel and amount of phosphorylated and non-phosphorylated Src was visualized using anti-pTyr419 and anti-Tyr419 antibody (1:2500 dilution) respectively. Bands were quantified using ImageStudio Lite and percent autophosphorylated was calculated.

Src autophosphorylation assay with the SH4 domain

Src^{FL} WT (50 nM), E381T (35 nM), I444K (35 nM) or Src^{CD} WT (30 nM) purified in their dephosphorylated form were incubated with 5 µM SNAP protein or 5 µM $SH4^{SNAP}$ protein for 30 min in kinase reaction buffer (76 mM HEPES, pH 7.5, 5 mM $MgCl_2$, 150 mM NaCl, 3.8 mM EGTA, 0.2 mg/mL BSA, 150 uM Na_3VO_4). 30 µL of this reaction was added to 3x loading dye for a 0 min timepoint sample. To initiate the autophosphorylation reaction, 100 µM ATP was added and at the end of each timepoint, 30 µL of the reaction mixture was added to fresh 3x loading dye to terminate autophosphorylation. Samples from each timepoint were run on a SDS-PAGE gel and amount of phosphorylated Src and total Src was visualized using anti-pTyr419 and anti-Src antibody (1:2500 dilution), respectively. Bands were quantified using ImageStudio Lite and ratio of pTyr419 to total Src was determined.

Maleimide labeling and mass spectrometry

Purified Src^{FL} or Src^{3D} constructs K445C were diluted to 800 nM in mass spectrometry buffer (50 mM HEPES, pH 7.6, 150 mM NaCl, 5% glycerol and 0.02% (wt/vol) n-Dodecyl □ -D-maltoside (DDM))(Kahsai et al., 2014) treated with 5 µM of inhibitors **5** or **6**, and incubated at 25 ºC for 30 min. The kinase-inhibitor complex was then treated with 1 mM heavy or light N-ethyl maleimide (NEM) in a LoBind 1.5 mL eppendorf tube at 25 ºC for 30 min. The NEM labeling reaction was quenched with 10 mM of DTT in NH_4HCO_3 solution. 20 µL each of heavy and light maleimide-

treated reactions were mixed and protein was precipitated using 0.02% deoxycholate and 10% trichloroacetic acid on ice for 10 min. The precipitated protein was pelleted by spinning at 10,000 rpm for 15 min. The pellet was dried with 10 µL acetone and re-suspended in peptide solubilization buffer (8 M urea, 200 mM Tris-HCl, pH 8.0, 2.4 mM iodoacetamide, 0.001% DDM) by vortexing briefly. The mixture was incubated in the dark for 30 min. Trypsin digestion solution (1 µg/mL of trypsin in 1 mM $CaCl_2$, 200 mM Tris-HCl, pH 8.0) was added and the protein was digested overnight at 37 °C. Peptide was desalted using C18 ZipTips (Milipore) and each sample was run on the Finnigan LTQ Ion trap. [M+3H] peptide masses for both heavy and light NEM labeled peptides was analyzed using Xcalibur Quant software. Light and heavy NEM labeling reactions were swapped for each inhibitor and the above procedure was repeated.

2.6 REFERENCES

Bjorge, J.D., Bellagamba, C., Cheng, H.-C., Tanaka, A., Wang, J.H., and Fujita, D.J. (1995). Characterization of Two Activated Mutants of Human pp60c-srcThat Escape c-Src Kinase Regulation by Distinct Mechanisms. Journal of Biological Chemistry *270*, 24222–24228.

Boggon, T.J., and Eck, M.J. (2004). Structure and regulation of Src family kinases. Oncogene *23*, 7918–7927.

Charras, G.T. (2008). A short history of blebbing. J Microsc *231*, 466–478.

Devkota, S., Joseph, R.E., Boyken, S.E., Fulton, D.B., and Andreotti, A.H. (2017). An Autoinhibitory Role for the Pleckstrin Homology Domain of Interleukin-2-Inducible Tyrosine Kinase and Its Interplay with Canonical Phospholipid Recognition. Biochemistry *56*, 2938–2949.

Florio, M., Wilson, L.K., Trager, J.B., Thorner, J., and Martin, G.S. (1994). Aberrant protein phosphorylation at tyrosine is responsible for the growth-inhibitory action of pp60v-src expressed in the yeast Saccharomyces cerevisiae. Molecular Biology of the Cell *5*, 283–296.

Fowler, D.M., and Fields, S. (2014). Deep mutational scanning: a new style of protein science. Nat Meth *11*, 801–807.

Fowler, D.M., Araya, C.L., Fleishman, S.J., Kellogg, E.H., Stephany, J.J., Baker, D., and Fields, S. (2010). High-resolution mapping of protein sequence-function relationships. Nat Meth *7*, 741–746.

Fowler, D.M., Araya, C.L., Gerard, W., and Fields, S. (2011). Enrich: software for analysis of protein function by enrichment and depletion of variants. Bioinformatics *27*, 3430–3431.

García-Nafría, J., Watson, J.F., and Greger, I.H. (2016). IVA cloning: A single-tube universal cloning system exploiting bacterial In Vivo Assembly. Nature Publishing Group *6*, 27459.

Gietz, R.D., and Schiestl, R.H. (2007). High-efficiency yeast transformation using the LiAc/SS carrier DNA/PEG method. Nature Protocols *2*, 31–34.

Giorgione, J., and Newton, A.C. (2003). Measuring the binding of protein kinase C to sucrose-loaded vesicles. Methods Mol. Biol. *233*, 105–113.

Golkowski, M., Vidadala, R.S.R., Lombard, C.K., Suh, H.W., Maly, D.J., and Ong, S.-E. (2017). Kinobead and Single-Shot LC-MS Profiling Identifies Selective PKD Inhibitors. J. Proteome Res. *16*, 1216–1227.

Gonfloni, S., Williams, J.C., Hattula, K., Weijland, A., Wierenga, R.K., and Superti-Furga, G. (1997). The role of the linker between the SH2 domain and catalytic domain in the regulation and function of Src. Embo J. *16*, 7261–7271.

Hall, B.G., Acar, H., Nandipati, A., and Barlow, M. (2013). Growth Rates Made Easy. Molecular Biology and Evolution *31*, 232–238.

Hantschel, O., Nagar, B., Guettler, S., Kretzschmar, J., Dorey, K., Kuriyan, J., and Superti-Furga, G. (2003). A myristoyl/phosphotyrosine switch regulates c-Abl. Cell *112*, 845–857.

Hiatt, J.B., Patwardhan, R.P., Turner, E.H., Lee, C., and Shendure, J. (2010). Parallel, tag-directed assembly of locally derived short sequence reads. Nat Meth *7*, 119–122.

Joseph, R.E., Wales, T.E., Fulton, D.B., Engen, J.R., and Andreotti, A.H. (2017). Achieving a Graded Immune Response: BTK Adopts a Range of Active/Inactive Conformations Dictated by Multiple Interdomain Contacts. Structure *25*, 1481–1494.e1484.

Kahsai, A.W., Rajagopal, S., Sun, J., and Xiao, K. (2014). Monitoring protein conformational changes and dynamics using stable-isotope labeling and mass spectrometry. Nat Protoc *9*, 1301–1319.

Klinghoffer, R.A., Sachsenmaier, C., Cooper, J.A., and Soriano, P. (1999). Src family kinases are required for integrin but not PDGFR signal transduction. Embo J. *18*, 2459–2471.

Krishnamurty, R., Brigham, J.L., Leonard, S.E., Ranjitkar, P., Larson, E.T., Dale, E.J., Merritt, E.A., and Maly, D.J. (2012). Active site profiling reveals coupling between domains in SRC-family kinases. Nat Chem Biol *9*, 43–50.

Kritzer, J.A., Freyzon, Y., and Lindquist, S. (2018). Yeast can accommodate phosphotyrosine: v-Src toxicity in yeast arises from a single disrupted pathway. FEMS Yeast Research.

Kung, J.E., and Jura, N. (2016). Structural Basis for the Non-catalytic Functions of Protein Kinases. Structure *24*, 7–24.

LaFevre-Bernt, M., Sicheri, F., Pico, A., Porter, M., Kuriyan, J., and Miller, W.T. (1998). Intramolecular regulatory interactions in the Src family kinase Hck probed by mutagenesis of a conserved tryptophan residue. Journal of Biological Chemistry *273*, 32129–32134.

Lahiry, P., Torkamani, A., Schork, N.J., and Hegele, R.A. (2010). Kinase mutations in human disease: interpreting genotype–phenotype relationships. Nature Reviews Genetics *11*, 60–74.
Leonard, S.E., Register, A.C., Krishnamurty, R., Brighty, G.J., and Maly, D.J. (2014). Divergent Modulation of Src-Family Kinase Regulatory Interactions with ATP-Competitive Inhibitors. ACS Chem. Biol. *9*, 1894–1905.

Levy, J.B., Iba, H., and Hanafusa, H. (1986). Activation of the transforming potential of p60c-src by a single amino acid change. Proc. Natl. Acad. Sci. U.S.a. *83*, 4228–4232.

Maffei, M., Arbesú, M., Le Roux, A.-L., Amata, I., Roche, S., and Pons, M. (2015). The SH3 Domain Acts as a Scaffold for the N-Terminal Intrinsically Disordered Regions of c-Src. Structure *23*, 893–902.

Manning, G., Whyte, D.B., Martinez, R., Hunter, T., and Sudarsanam, S. (2002). The protein kinase complement of the human genome. Science *298*, 1912–1934.

McLaughlin, S., and Aderem, A. (1995). The myristoyl-electrostatic switch: a modulator of reversible protein-membrane interactions. Trends in Biochemical Sciences *20*, 272–276.

Olsen, J.G., Teilum, K., and Kragelund, B.B. (2017). Behaviour of intrinsically disordered proteins in protein–protein complexes with an emphasis on fuzziness. Cellular and Molecular Life Sciences *74*, 3175–3183.

Patwardhan, P., and Resh, M.D. (2010). Myristoylation and Membrane Binding Regulate c-Src Stability and Kinase Activity. Mol. Cell. Biol. *30*, 4094–4107.

Rappsilber, J., Mann, M., and Ishihama, Y. (2007). Protocol for micro-purification, enrichment, pre-fractionation and storage of peptides for proteomics using StageTips. Nature Protocols *2*, 1896–1906.

Rivoire, O., Reynolds, K.A., and Ranganathan, R. (2016). Evolution-Based Functional Decomposition of Proteins. PLoS Comput Biol *12*, e1004817.

Röhrig, U.F., Majjigapu, S.R., Grosdidier, A., Bron, S., Stroobant, V., Pilotte, L., Colau, D., Vogel, P., Van den Eynde, B.J., Zoete, V., et al. (2012). Rational Design of 4-Aryl-1,2,3-Triazoles for Indoleamine 2,3-Dioxygenase 1 Inhibition. J. Med. Chem. *55*, 5270–5290.

Rubin, A.F., Gelman, H., Lucas, N., Bajjalieh, S.M., Papenfuss, A.T., Speed, T.P., and Fowler, D.M. (2017). A statistical framework for analyzing deep mutational scanning data. Genome Biol. *18*, 741.

Seidel-Dugan, C., Meyer, B.E., Thomas, S.M., and Brugge, J.S. (1992). Effects of SH2 and SH3 deletions on the functional activities of wild-type and transforming variants of c-Src. Mol. Cell. Biol. *12*, 1835–1845.

Serafimova, I.M., Pufall, M.A., Krishnan, S., Duda, K., Cohen, M.S., Maglathlin, R.L., McFarland, J.M., Miller, R.M., Frödin, M., and Taunton, J. (2012). Reversible targeting of noncatalytic cysteines with chemically tuned electrophiles. Nat Chem Biol *8*, 471–476.

Sigal, C.T., Zhou, W., Buser, C.A., McLaughlin, S., and Resh, M.D. (1994). Amino-terminal basic residues of Src mediate membrane binding through electrostatic interaction with acidic phospholipids. Proc. Natl. Acad. Sci. U.S.a. *91*, 12253–12257.

Skora, L., Mestan, J., Fabbro, D., Jahnke, W., and Grzesiek, S. (2013). NMR reveals the allosteric opening and closing of Abelson tyrosine kinase by ATP-site and myristoyl pocket inhibitors. Proc. Natl. Acad. Sci. U.S.a. *110*, E4437–E4445.

Song, Y., DiMaio, F., Wang, R.Y.-R., Kim, D., Miles, C., Brunette, T.J., Thompson, J., and Baker, D. (2013). High-Resolution Comparative Modeling with RosettaCM. Structure *21*, 1735–1742.

Spassov, D.S., Ruiz-Saenz, A., Piple, A., and Moasser, M.M. (2018). A Dimerization Function in the Intrinsically Disordered N-Terminal Region of Src. Cell Reports *25*, 449–463.e4.

Starita, L.M., Young, D.L., Islam, M., Kitzman, J.O., Gullingsrud, J., Hause, R.J., Fowler, D.M., Parvin, J.D., Shendure, J., and Fields, S. (2015). Massively Parallel Functional Analysis of BRCA1 RING Domain Variants. Genetics *200*, 413–422.

Suzuki, Y., Onge, R.P.S., Mani, R., King, O.D., Heilbut, A., Labunskyy, V.M., Chen, W., Pham, L., Zhang, L.V., Tong, A.H.Y., et al. (2011). Knocking out multigene redundancies via cycles of sexual assortment and fluorescence selection. Nat Meth *8*, 159–164.

Taylor, S.S., Keshwani, M.M., Steichen, J.M., and Kornev, A.P. (2012). Evolution of the eukaryotic protein kinases as dynamic molecular switches. Philosophical Transactions of the Royal Society B: Biological Sciences *367*, 2517–2528.

Theile, C.S., Witte, M.D., Blom, A.E.M., Kundrat, L., Ploegh, H.L., and Guimaraes, C.P. (2013). Site-specific N-terminal labeling of proteins using sortase-mediated reactions. Nature Protocols *8*, 1800–1807.

Thompson, E.E., Kornev, A.P., Kannan, N., Kim, C., Eyck, Ten, L.F., and Taylor, S.S. (2009). Comparative surface geometry of the protein kinase family. Protein Science *18*, 2016–2026.
Tien, M.Z., Meyer, A.G., Sydykova, D.K., Spielman, S.J., and Wilke, C.O. (2013). Maximum Allowed Solvent Accessibilites of Residues in Proteins. PLoS ONE *8*, e80635.

Tighe, A., Staples, O., and Taylor, S. (2008). Mps1 kinase activity restrains anaphase during an unperturbed mitosis and targets Mad2 to kinetochores. The Journal of Cell Biology *181*, 893–901.

Tournaviti, S., Hannemann, S., Terjung, S., Kitzing, T.M., Stegmayer, C., Ritzerfeld, J., Walther, P., Grosse, R., Nickel, W., and Fackler, O.T. (2007). SH4-domain-induced plasma membrane dynamization promotes bleb-associated cell motility. Journal of Cell Science *120*, 3820–3829.

Towler, D.A., Adams, S.P., Eubanks, S.R., Towery, D.S., Jackson-Machelski, E., Glaser, L., and Gordon, J.I. (1988). Myristoyl CoA:protein N-myristoyltransferase activities from rat liver and yeast

possess overlapping yet distinct peptide substrate specificities. Journal of Biological Chemistry *263*, 1784–1790.

Wang, Q., Vogan, E.M., Nocka, L.M., Rosen, C.E., Zorn, J.A., Harrison, S.C., and Kuriyan, J. (2015). Autoinhibition of Bruton's tyrosine kinase (Btk) and activation by soluble inositol hexakisphosphate. Elife *4*, e06074.

Wang, Q., Cahill, S.M., Blumenstein, M., and Lawrence, D.S. (2006). Self-Reporting Fluorescent Substrates of Protein Tyrosine Kinases. J. Am. Chem. Soc. *128*, 1808–1809.

Xu, W., Doshi, A., Lei, M., Eck, M.J., and Harrison, S.C. (1999). Crystal structures of c-Src reveal features of its autoinhibitory mechanism. Mol. Cell *3*, 629–638.
Xu, W., Harrison, S.C., and Eck, M.J. (1997). Three-dimensional structure of the tyrosine kinase c-Src. Nature *385*, 595–602.

Young, M.A., Gonfloni, S., Superti-Furga, G., Roux, B., and Kuriyan, J. (2001). Dynamic coupling between the SH2 and SH3 domains of c-Src and Hck underlies their inactivation by C-terminal tyrosine phosphorylation. Cell *105*, 115–126.

Chapter 3. COMPREHENSIVE IDENTIFICATION OF RESISTANCE MUTATIONS TO CONFORMATION-SELECTIVE KINASE INHIBITORS

This chapter is adapted from a manuscript currently in preparation. The inhibitors LF-278, LF-279, and LF-280 were synthesized by Linglan Fang in the Maly Lab.

3.1 ABSTRACT

Kinase inhibitors are routinely employed as cancer therapeutics, but their long-term usefulness is limited due to the emergence of drug resistance. For some inhibitors, resistance is caused by mutations arising in the targeted kinase. These resistance mutations can be quite diverse; even inhibitors of the same kinase can exhibit a unique collection of mutations. Understanding the mutational routes to drug resistance for a given kinase is critical, both for genomics-guided medicine and for improving the design of next-generation inhibitors. To comprehensively investigate how kinase sequence affects drug resistance, we used a massively-parallel yeast assay to test a library of ~3,500 Src kinase mutants against a panel of inhibitors that each target a distinct conformation of Src's catalytic domain. Here, we present a maps of mutations that confer resistance to each of our conformation-selective Src inhibitors. We identify resistance mutations that are shared between all tested inhibitors as well as mutations that are unique to a given inhibitor. Finally, we compare our experimentally-derived mutations to ones observed in inhibitor-resistant cancers and find high concordance, demonstrating the applicability of our method.

3.2 INTRODUCTION

Targeted therapeutics, in particular kinase inhibitors (KIs), have revolutionized the treatment of specific cancers (Gharwan and Groninger, 2015; Zhang et al., 2009). Most KIs target the kinase's catalytic domain (CD) and prevent ATP binding, thereby turning off oncogenic activity. Unfortunately, as with other cancer therapies, patients treated with KIs nearly always develop resistance. KI resistance is a complex and heterogeneous clinical outcome; with diverse and overlapping causes (Garraway and Jänne, 2012; Lovly and Shaw, 2014). One recurring mechanism observed across a variety of KIs occurs through single mutations in the target kinase that render it

insensitive to drug. These resistance mutations can be quite stereotyped, for example, 50% of lung cancer patients taking the EGFR inhibitor erlotinib will acquire the EGFR T790M mutation which disfavors erlotinib binding (Yun et al., 2008) However, for other cancer targets, the spectrum of observed resistance mutations is much more varied; with dozens of unique mutations identified for some kinase-inhibitor pairs (Apperley, 2007) (Choi et al., 2010) Interestingly, resistance mutations for one KI may still be sensitive to other KIs (Lin et al., 2017; Soverini et al., 2011), thus creating opportunities for treatment decisions based on a patient's specific resistance genotype.

How can a single mutation result in inhibitor resistance? One obvious explanation is through the addition of unfavorable chemical interactions with the inhibitor. For example, mutation of the "gatekeeper" residue (which sits near the back of the ATP binding pocket) to a bulkier, hydrophobic residue can introduce steric clashes with KIs, and indeed, gatekeeper mutations are commonly discovered in patients who stop responding to inhibitor treatment (Gibbons et al., 2012). Similarly, other residues that also make inhibitor contacts, like those in hinge region, are recurrent sites for resistance mutations (Balzano et al., 2011). However, the mechanistic basis for many other clinically observed mutations that do not directly interfere with drug binding are less clear.

One important factor to consider is that the CD is structurally dynamic and shifts between inactive and active states. Two conserved structural features are primarily responsible for determining these states: the αC-helix and the activation loop (which contains the DFG-motif) (**Figure 3.1A**). In the active conformation, both of these features are stationed "in" towards the hinge region and coordinate ATP binding and proper substrate positioning, thereby allowing the phosphotransferase reaction to occur. However, when either of these features are shifted "out", substrate recognition cannot occur and catalytic activity is impaired. One consequence of this dynamic property of the CD is that different KIs selectively recognize and bind to distinct CD conformations (hereafter referred to as binding modes) (**Figure 3.1B**). Most currently available KIs fall into one of three binding modes, though others exist (Wu et al., 2016). Type 1 inhibitors bind the active conformation (αC-in/DFG-in). Type 1.5 inhibitors bind an inactive conformation, where the activation loop is correctly positioned but the αC helix is pushed outwards (αC-out/DFG-in). Finally, Type 2 inhibitors recognize an alternative inactive conformation where the DFG motif is rotated 180° away from the active site (αC-in/DFG-out). Thus, for a given KI to function, the targeted kinase must be able to adopt the precise conformation that the KI recognizes. Therefore, one mechanism whereby mutations could confer drug resistance is by preventing the kinase from adopting the necessary conformation.

Hundreds of resistance mutations to diverse inhibitor-kinase pairs have been identified, but we still lack broad insights into the nature of these mutations, especially with respect to conformationally-selective KIs. Better understanding of the specific residues that impact inhibitor binding could improve the design of novel compounds, but current methods for identifying these resistance mutations are low-throughput and time-consuming. These technical limitations are especially glaring given the vast number of mutations that potentially could exist for a given kinase (e.g., the average 250 amino acid CD has 5,000 theoretical single mutants). Methods to comprehensively interrogate KI resistance at amino acid-resolution would enable investigation into several outstanding questions. For example, what are the commonalities and differences with respect to observed resistance mutations across different inhibitors? Are certain conformation-selective inhibitors impaired by mutations at specific structural features or motifs? And, given the exquisite structural homology across human kinase CDs, can we identify common residues that may affect sensitivity to these three general inhibitor binding modes?

To address these questions, we use a deep mutational scanning (DMS) (Fowler and Fields, 2014) approach to investigate the impact of nearly every mutation in Src kinase's CD on the efficacy of a panel of conformation-selective inhibitors. We identify dozens of mutations that antagonize inhibitor efficacy, including ones unique to each inhibitor. Clustering these mutations based on binding mode identifies structural elements that may contribute to the adoption of specific conformations. Lastly, we benchmark these newly discovered Src mutations against previously identified resistance mutations in other clinically-relevant kinases, suggesting that these residues may broadly be important to consider for future drug development endeavors.

3.3 RESULTS

Synthesis of conformationally-selective Src inhibitors

We synthesized three conformation-selective Src inhibitors, LF-278, LF-279 and LF-280 (**Figure 3.1C**) that share the same adenosine-mimicking moiety, but differ in the precise CD conformation they recognize. LF-278 recognizes the active αC-helix-in/DFG-in, while LF-279 and LF-280 are selective for two different inactive conformations, the αC-helix-out/DFG-in and αC-helix-in/DFG-out, respectively. These inhibitors are structural analogs of our previously published Cystimatik probes (Ahler *et al.*, 2019), except they lack the electrophilic groups.

Comprehensive resistance mutant identification

To comprehensively identify mutations of Src that confer resistance to a panel of its pharmacological inhibitors, we used a modified protocol of a previously described yeast assay for the massively-parallel functional characterization of Src mutants (Ahler *et al.*, 2019). Briefly, expression of human Src in *S. cerevisiae* is toxic to yeast due to uncontrolled phosphorylation, but this growth defect can be remedied upon treatment with a Src inhibitor. To calibrate growth conditions, we identified concentrations of each inhibitor sufficient to fully rescue the growth of yeast expressing Src WT , but which had no effect on the growth of yeast expressing Src T341I drug-resistant mutant (**Figure 3.1D**).

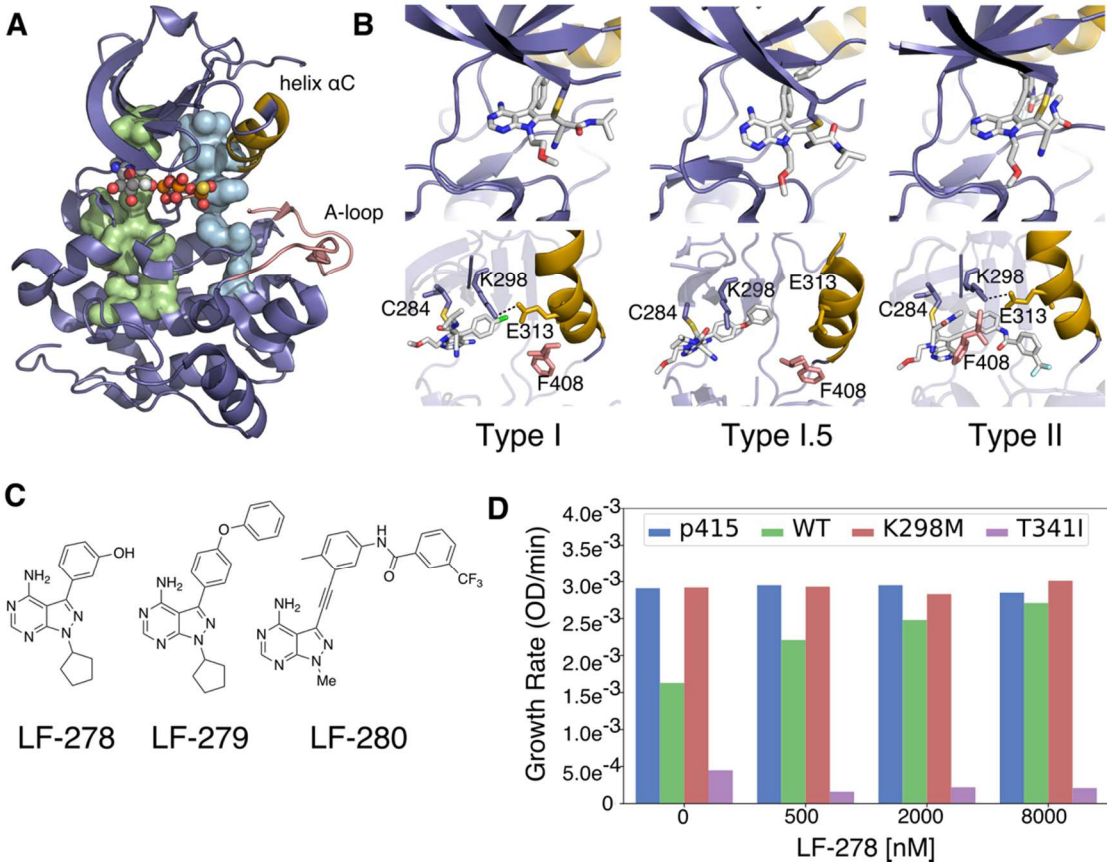

Figure 3.1. Src inhibitors selective for different catalytic domain conformations.

A. Crystal structure of Src's catalytic domain, with the αC-helix (yellow) and activation loop (pink, contains the DFG motif) depicted. PDB: **3DQW**. **B**. Crystal structures of Src's catalytic domain indicating the αC-helix and DFG motif conformations of Type I (left, PDB: **5SWH**), Type I.5 (middle, PDB: **5TEH**), and Type II (right, PDB: **5SYS**) inhibitors. The catalytic salt bridge between K298 and E313 is shown (broken in αC-helix-out). **C**. Chemical structures of the three inhibitors used in this study. **D**. Growth rates of yeast expressing Src WT (green), catalytically-inactive K298M (red), inhibitor-resistant T341I (purple) or empty vector (blue) in varying concentrations of LF-278.

Next, we grew a previously described yeast library of Src mutants (Ahler *et al.*, 2019) in varying concentrations of each inhibitor and sampled outgrowth at various time points. At each time point we extracted plasmid DNA, amplified barcodes, and then deeply sequenced the barcode amplicons to quantify mutant frequencies. Activity scores were calculated for 3,510 Src mutants in each of the three inhibitors (**Methods**). Even at the highest inhibitor concentrations, the degree of Src inhibition appeared to differ between the inhibitors (**Figure 3.2A**). Therefore, to account for this difference in inhibition and, thus selective pressure, we quantile normalized all activity scores across the three inhibitor selections (**Methods)**. Unless otherwise indicated, all subsequent analyses use quantile normalized scores (**Figure 3.2B**). As expected, most mutants were sensitive to all tested inhibitors as indicated by the distribution of scores, however some mutants were still active in the presence of inhibitor. We defined "resistance" as any nonsynonymous mutant that had an activity score above the 3x standard deviation of the synonymous distribution (after filtering out singleton residues to reduce false positives). Using this definition, we identified 107 mutations for LF-278, 86 for LF-279, and 114 for LF-280.

Resistance mutations occur throughout catalytic domain

These comprehensive data enable broad detection of resistance patterns for our different inhibitors. Grouping the resistance mutations by inhibitor, we find relatively few universal resistance mutations as well as many drug-specific ones (**Figure 3.2C)**. Twenty-two mutations occurring at seven positions conferred resistance to all inhibitors. These universal resistance sites included residues like L276 and V326, both of which are hotspots for resistance in several other kinases (**Figure 3.2D**). Interestingly, LF-278 and LF-280 (which both recognize αC-helix-in conformations) share a majority of mutations in common, whereas LF-279 (which uniquely recognizes an αC-helix-out conformation) appears to have more private ones.

Next, to gain a residue-level perspective of resistance, we collapsed all identified mutations down to their amino acid positions and mapped them onto Src's CD. One straightforward hypothesis is that residues that make direct binding interactions with an inhibitor are likely to confer resistance when mutated, due to the abolishment of these crucial bonds. To test this, we identified each inhibitor's "binding pocket" based on previously published crystal structures co-crystalized with analogous inhibitors (**Methods**). Surprisingly, resistance mutations almost entirely mapped to distal residues, with only LF-278 (**Figure 3.2E**) having any resistance mutations at our defined binding pockets.

Given the unexpectedly high number of resistance mutations occurring at residues distant from the binding pocket, we wondered how these mutations could be operating. One possibility is that these mutations stimulate intrinsic Src activity, thereby resulting in resistance. Previously, we classified this same Src library on the basis of activity (in the absence of any inhibitor) into three categories: gain of function, loss of function, and WT-like (Ahler *et al.*, 2019). We used these same categories to annotate each resistance mutation with respect to its effect on basal kinase activity. Interestingly, the vast majority resistance mutations are all gain of function (**Figure 3.2F**), suggesting that mutations which bias Src towards active states are also broadly sufficient to impair drug inhibition. Thus, drug resistance through intrinsically-increased kinase activity appears to be the predominant route to overcoming inhibition in our Src scan.

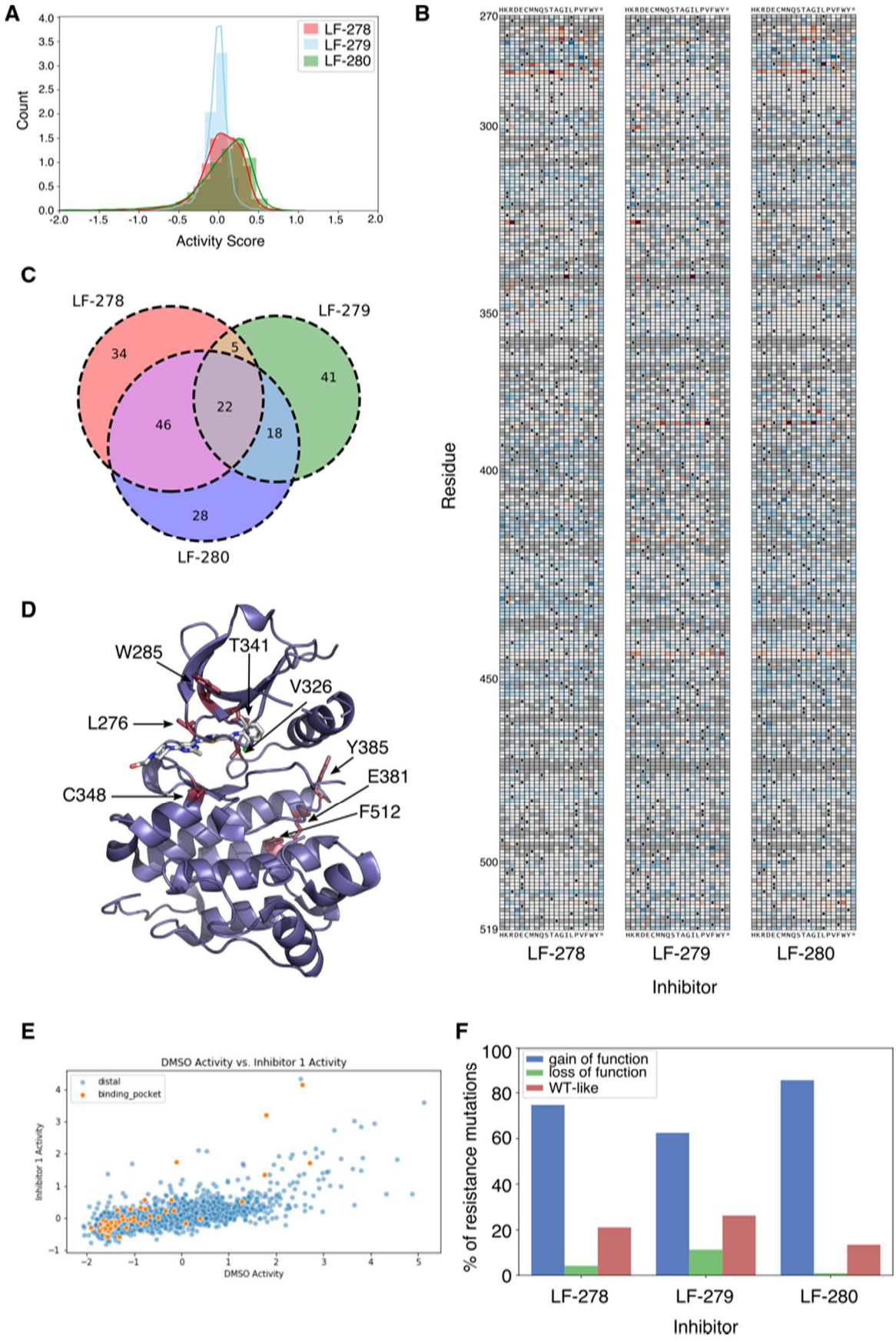
A
LF-278
LF-279
LF-280
Count
Activity Score
B
Residue
Inhibitor
LF-278
LF-279
LF-280
C
LF-278
LF-279
LF-280
34
5
41
22
46
18
28
D
W285
T341
V326
L276
Y385
E381
C348
F512
E
DMSO Activity vs. Inhibitor 1 Activity
distal
binding_pocket
Inhibitor 1 Activity
DMSO Activity
F
gain of function
loss of function
WT-like
% of resistance mutations
LF-278
LF-279
LF-280
Inhibitor

Figure 3.2. Comprehensive mapping of Src resistance mutations.

A. Activity score distributions of all nonsynonymous Src mutants under inhibitor treatment. **B**. Heatmaps of quantile normalized activity scores for Src mutants for each of the three inhibitors. Red indicates higher activity while blue indicates lower activity. Black dots indicate the WT amino acid at that position and grey boxes indicate missing data. **C.**Venn diagram showing the number of shared and unique resistance mutants for each inhibitor. **D**. Crystal structure of Src's CD (PDB: **3G5D**) indicating residues of resistance mutations common to all three inhibitors. **E.** Comparison of activity scores in DMSO vs. LF-278 for Src mutant library. Color of dot indicates residue makes direct interaction with inhibitor (orange) or is distant from the binding site (blue). **F.** Percentage of resistance mutants that are intrinsically gain of function, WT-like, or loss of function with respect to inhibitor. Classifications were derived previously (Ahler *et al.* 2019).

Comparison with known resistance mutants in other kinases

Finally, we benchmarked our newly identified Src resistance mutations against other kinases with previously identified mutants. To do this, we first collected all observed resistance mutations from the COSMIC database v87 (Forbes et al., 2017), which contains 195 unique resistance mutations in nine kinase targets associated with 18 different inhibitors (**Table 3.1**). Next, when a co-crystal structure was available, we classified each inhibitor-kinase pair according to binding mode (Ung et al., 2018) resulting in seven Type I, three Type I.5, and six Type II inhibitors. Grouping the data by binding mode reveals the majority of mutations represented in COSMIC are for Type II inhibitors, which is primarily driven by resistance mutations in ABL to the widely-used inhibitor imatinib (**Figure 3.3A**).

Next, to identify analogous resistance mutations across drug targets, we aligned the kinase sequences using Src as reference. Then, we annotated each aligned position with the clinically-derived resistance mutants and our experimentally-derived Src resistance mutants (**Figure 3.3B**). This integrated view of both experimentally and clinically defined resistance mutations enabled shared hotspots of resistance to emerge, including at the β1/β2 sheets (positions 274-285) and at the hinge region between the two kinase lobes (positions 339-344). Additionally, our Src data identified CD regions that had not previously been annotated with resistance mutations in other inhibitors. For example, the LF-279 scan identified a series of residues (positions 331, 335, and 337) that line the interface between the αC-helix and β4-sheet, and mutations here are especially resistant to LF-279. Given that the side chains of V331, E335 and I337 jut into this interface, it is tempting to speculate that mutations here may act by preventing the adoption of the αC-helix-out conformation. In summary, our Src results broadly agree with known mutations in other kinases, but also identify CD subdomains which may influence conformations relevant to specific binding modes.

Table 3.1. Kinases, inhibitors and resistance mutants represented in COSMIC v.87 database

Kinase	Inhibitor	Binding Mode	# of unique resistance mutants
ABL1	Bosutinib	II	5
ABL1	Dasatinib	I	9
ABL1	Imatinib	II	85
ABL1	Nilotinib	II	9
ALK	Alectinib	I	4
ALK	Ceritinib	I	7
ALK	Crizotinib	I	9
BRAF	Imatinib	N/A	1
BRAF	Vemurafenib	I.5	1
BTK	Ibrutinib	N/A	5
EGFR	Afatinib	I	1
EGFR	Erlotinib	I.5	1
EGFR	Geftinib	I	2
EGFR	Osimertinib	I	10
FLT3	Quizartinib	II	4
FLT3	Soraftenib	N/A	3
FLT3	Sunitinib	N/A	1
KIT	Crizotinib	N/A	1
KIT	Imatinib	II	23
KIT	Nilotinib	N/A	1
KIT	Sunitinib	II	1
MET	Capmatinib	N/A	2
MET	Crizotinib	I.5	7
MET	Savoltinib	N/A	1
PGFRA	Imatinib	N/A	1
PGFRA	Sunitinib	N/A	1

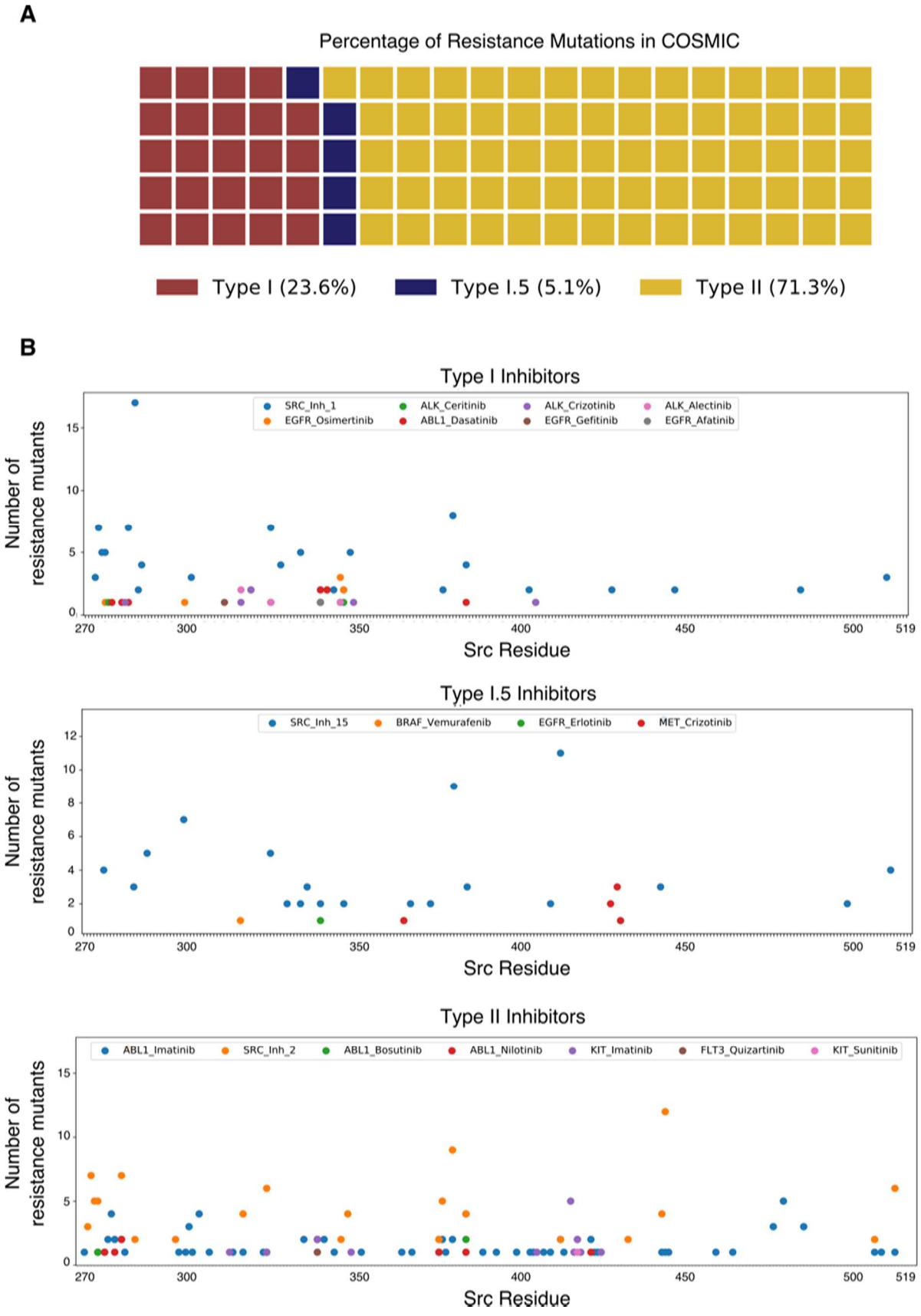
A
Percentage of Resistance Mutations in COSMIC
Type I (23.6%)
Type I.5 (5.1%)
Type II (71.3%)
B
Type I Inhibitors
SRC_Inh_1
EGFR_Osimertinib
ALK_Ceritinib
ABL1_Dasatinib
ALK_Crizotinib
EGFR_Gefitinib
ALK_Alectinib
EGFR_Afatinib
Number of resistance mutants
Src Residue
Type I.5 Inhibitors
SRC_Inh_15
BRAF_Vemurafenib
EGFR_Erlotinib
MET_Crizotinib
Number of resistance mutants
Src Residue
Type II Inhibitors
ABL1_Imatinib
SRC_Inh_2
ABL1_Bosutinib
ABL1_Nilotinib
KIT_Imatinib
FLT3_Quizartinib
KIT_Sunitinib
Number of resistance mutants
Src Residue

Figure 3.3. Kinase resistance mutations in COSMIC

A. Percentage of resistance mutations in COSMIC grouped by inhibitor binding mode. **B**. Number of resistance mutations for all Type I (top), Type 1.5 (middle) or Type II (bottom) inhibitors in the COSMIC database with Src DMS data added in. All kinases are numbered according to analogous Src residue. Resistance mutations for inhibitors with no ascribed binding mode or that lack analogous Src residues are not included.

3.4 DISCUSSION

We tested a library of thousands of single amino acid mutants of Src kinase against a panel of inhibitors that recognize distinct conformations of Src's CD. In addition to identifying broadly resistant mutations, we discovered mutations that uniquely conferred resistance to specific inhibitors. A subset of these unique resistance mutations mapped to precise regions in Src's CD, pinpointing residues that might be responsible for the adoption of specific conformations. Given the structural homology across kinase CDs, these residues may be general contributors to the structural regulation of kinases.

The quantity of mutations in this study enabled us to investigate broad sequence-function relationships relating to KI resistance. For example, we saw that binding pocket residues were, by and large, not primary sites of resistance mutations. This may in part be explained by the near uniform loss of activity observed upon mutating these residues. We also identify mutations that appear to selectively impair inhibitor recognition. What could explain this? One reasonable interpretation is that these mutations may specifically prevent adoption of the CD conformation a KI recognizes, but still allow some catalytic function. Further structural studies to prove whether these mutations do indeed bias towards specific conformations will be necessary.

Drug resistance is a near universal problem for KIs. Therefore, from a clinical perspective, methods for the identification of resistance mechanisms before an inhibitor is even approved could enable a more streamlined and rational drug discovery pipeline. This concept was recently put into practice by Loxo Oncology, who developed larotrectinib, the first FDA-approved KI for cancers with TRK mutations (Cocco et al., 2018).At the same time, Loxo developed an additional TRK inhibitor that could bypass predicted larotrectinib resistance mutations (identified using *in vitro* mutagenesis). Pleasingly, this follow-up inhibitor was used to immediately treat patients who became resistant to larotrectinib with efficacious results (Drilon et al., 2017). Thus, we envision that DMS could be a

general approach for drug companies to employ to improve the design of their next-generation inhibitors.

The data presented here are still new and many more analyses are required. As such, some experimental limitations of our system must be considered when interpreting these results. For example, although KI binding modes are one important difference between our tested inhibitors, other factors certainly exist. Differences in drug potency, solubility, and stability over experimental time course—irrespective of binding mode—could contribute to the perceived differences in resistance mutations. Moreover, our mutational scan was thorough, but not complete. In particular, residues in the hinge region—which make important KI interactions—were poorly represented in our data. Finally, our analytic methods restrict us to make qualitative definitions of resistance. A model to generate a more quantitative measure of resistance from high-throughput data would be of great value.

In summary, we present here our initial maps of resistance to conformationally-selective Src inhibitors. Although the analyses performed so far have been rudimentary, intriguing results have nevertheless emerged. For example, one hypothesis for the LF-279-specific patch of mutants occurring at the αC-β4 interface could be impairment of the inactive αC-helix-out movement. Indeed, restriction of αC-helix dynamics is one gain of function mechanism seen in other kinases (Foster *et al.*, 2016), suggesting these activating mutants may intrinsically be insensitive to any Type 1.5 inhibitor. Clearly, orthogonal approaches to validate these identified resistance mutations will be necessary. To this end, we are currently pursuing more traditional *in vitro* biochemical assays of kinase activity and inhibitor sensitivity to characterize select mutants. Finally, because Src itself is not currently a FDA-approved drug target in oncology, we hope to exploit the structural commonalities amongst kinases and use our Src data to predict resistance mutations to other kinases with currently employed inhibitors in the clinic.

3.5 METHODS

S. cerevisiae genetics and cell culture

All experiments were performed in BY4741 Green Monster (a generous gift from Dr. Fritz Roth). All Src constructs were cloned into the p415 GAL1 plasmid and transformants were selected for by plating on C-Leu media. All growth experiments were performed in C-Leu media to maintain plasmid.

Identifying resistance mutations

To identify resistance mutations, we grew yeast expressing our previously described Src mutant library (Ahler *et al.*, 2019) in the absence or presence of varying concentrations of Src inhibitor. Upon inhibitor treatment, yeast harboring sensitive Src variants have their growth rescued, while those expressing resistant Src variants continue to grow poorly. Time points were sampled throughout growth, plasmids extracted, barcodes amplified and deeply sequenced on an Illumina NextSeq run.

Data analysis

Illumina sequencing reads were processed using bcl2fastq and and analyzed using Enrich2 (Rubin et al., 2017). To account for differences in selection pressure across the different inhibitor treatments, mutants were divided into nonsynonymous or synonymous and each category was quantile normalized across all three inhibitor selections.

Binding pocket definition

The binding pocket for each tested inhibitor was determined using structures of Src co-crystalized with inhibitors analogous to LF-278, LF-279, and LF-280 (**PDB**: 5SWH, 5TEH, 5SYS, respectively). Residues were included in the binding pocket if any atom in the residue was <3.5Å away (Euclidean distance) from any atom in the given inhibitor.

Resistance mutant comparisons with other kinases

To compare our experimentally-identified Src mutations to known resistance mutations in other kinases, we extracted all "Drug Resistance" mutations for kinases in the COSMIC database v87. We aligned this set of kinases to the Src sequence using the MUSCLE algorithm. Classification of inhibitor types for each kinase-drug pair were established from literature. Analogous Src residue numbering was generated using custom scripts.

3.6 REFERENCES

Ahler E., Register A.C., Chakraborty S., Fang L., Dieter E.M., Sitko K.A., et al. (2019). A Combined Approach Reveals a Regulatory Mechanism Coupling Src's Kinase Activity, Localization and Phosphotransferase-Independent Functions. Molecular Cell *74*.

Apperley, J.F. (2007). Part I: mechanisms of resistance to imatinib in chronic myeloid leukaemia. Lancet Oncol. *8*, 1018–1029.

Balzano, D., Santaguida, S., Musacchio, A., and Villa, F. (2011). A general framework for inhibitor resistance in protein kinases. Chem. Biol. *18*, 966–975.

Choi, Y.L., Soda, M., Yamashita, Y., Ueno, T., Takashima, J., Nakajima, T., Yatabe, Y., Takeuchi, K., Hamada, T., Haruta, H., et al. (2010). EML4-ALK mutations in lung cancer that confer resistance to ALK inhibitors. N. Engl. J. Med. *363*, 1734–1739.

Cocco, E., Scaltriti, M., and Drilon, A. (2018). NTRK fusion-positive cancers and TRK inhibitor therapy. Nature Publishing Group *15*, 1–17.

Drilon, A., Nagasubramanian, R., Blake, J.F., Ku, N., Tuch, B.B., Ebata, K., Smith, S., Lauriault, V., Kolakowski, G.R., Brandhuber, B.J., et al. (2017). A Next-Generation TRK Kinase Inhibitor Overcomes Acquired Resistance to Prior TRK Kinase Inhibition in Patients with TRK Fusion-Positive Solid Tumors. Cancer Discov *7*, 963–972.

Foster, S. A., Whalen, D. M., Özen, A., Wongchenko, M. J., Yin, J., Yen, I., et al. (2016). Activation Mechanism of Oncogenic Deletion Mutations in BRAF, EGFR, and HER2. *Cancer Cell*, *29*(4), 477–493.

Forbes, S.A., Beare, D., Boutselakis, H., Bamford, S., Bindal, N., Tate, J., Cole, C.G., Ward, S., Dawson, E., Ponting, L., et al. (2017). COSMIC: somatic cancer genetics at high-resolution. Nucleic Acids Res. *45*, D777–D783.

Fowler, D.M., and Fields, S. (2014). Deep mutational scanning: a new style of protein science. Nat. Methods *11*, 801–807.

Garraway, L.A., and Jänne, P.A. (2012). Circumventing Cancer Drug Resistance in the Era of Personalized Medicine. Cancer Discov *2*, 214–226.

Gharwan, H., and Groninger, H. (2015). Kinase inhibitors and monoclonal antibodies in oncology: clinical implications. Nature Publishing Group *13*, 209–227.

Gibbons, D.L., Pricl, S., Kantarjian, H., Cortes, J., and Quintás-Cardama, A. (2012). The rise and fall of gatekeeper mutations? The BCR-ABL1 T315I paradigm. Cancer *118*, 293–299.

Lin, J.J., Riely, G.J., and Shaw, A.T. (2017). Targeting ALK: Precision Medicine Takes on Drug Resistance. Cancer Discov *7*, 137–155.

Lovly, C.M., and Shaw, A.T. (2014). Molecular Pathways: Resistance to Kinase Inhibitors and Implications for Therapeutic Strategies. Clin Cancer Res *20*, 2249–2256.

Rubin, A.F., Gelman, H., Lucas, N., Bajjalieh, S.M., Papenfuss, A.T., Speed, T.P., and Fowler, D.M. (2017). A statistical framework for analyzing deep mutational scanning data. Genome Biol. *18*, 150.

Soverini, S., Hochhaus, A., Nicolini, F.E., Gruber, F., Lange, T., Saglio, G., Pane, F., Müller, M.C., Ernst, T., Rosti, G., et al. (2011). BCR-ABL kinase domain mutation analysis in chronic myeloid

leukemia patients treated with tyrosine kinase inhibitors: recommendations from an expert panel on behalf of European LeukemiaNet. Blood *118*, 1208–1215.

Ung, P.M.-U., Rahman, R., and Schlessinger, A. (2018). Redefining the Protein Kinase Conformational Space with Machine Learning. Cell Chemical Biology *25*, 916–924.e2.

Wu, P., Nielsen, T.E., and Clausen, M.H. (2016). Small-molecule kinase inhibitors: an analysis of FDA-approved drugs. Drug Discov. Today *21*, 5–10.

Yun, C.-H., Mengwasser, K.E., Toms, A.V., Woo, M.S., Greulich, H., Wong, K.-K., Meyerson, M., and Eck, M.J. (2008). The T790M mutation in EGFR kinase causes drug resistance by increasing the affinity for ATP. Proc. Natl. Acad. Sci. U.S.a. *105*, 2070–2075.

Zhang, J., Yang, P.L., and Gray, N.S. (2009). Targeting cancer with small molecule kinase inhibitors. Nat Rev Cancer *9*, 28–39.

Chapter 4. CONCLUSIONS AND FUTURE DIRECTIONS

In this chapter I summarize the results of my thesis and speculate on future directions. During my thesis, I developed a yeast growth assay for the massively-parallel characterization of Src mutants. I used this system to investigate two broad questions regarding Src biology: 1) what are the protein-intrinsic mechanisms that regulate Src activity? 2) how does Src become resistant to kinase inhibitors?

4.1 SUMMARY OF FINDINGS

The primary finding from my dissertation work is the discovery of a novel regulatory interaction between Src's SH4 and catalytic domains that govern its activity, conformation, and localization. That we were able to uncover this interaction in Src—one of the oldest and best studied kinases around—is perhaps surprising. However, two aspects of our specific approach empowered this finding. First, our mutational scanning approach was unbiased (at least, with respect to protein residues). Thus, we were able to functionally interrogate regions of Src that had been understudied or historically ignored. Second, Src's SH4 domain is intrinsically disordered, which makes standard approaches to elucidating the functional roles of these regions difficult. Our deep mutational scanning approach is fundamentally a genetic one, which is unaffected by technical difficulties imposed at the protein product level. Given that many proteins in the human proteome are predicted to contain similar intrinsically unstructured regions (Babu, 2016), our study is a proof of concept that high-throughput mutagenesis is a powerful method to probe protein domains that are refractory to traditional experimental techniques.

Finally, I think these studies demonstrate the experimental flexibility that deep mutational scanning approaches afford. Both **Chapter 2** and **Chapter 3** used the exact same experimental system, with the only differences occurring at the selection step. By simply altering the functional assay (in my case, either adding Src inhibitor or not), entirely new biological questions can be interrogated using the same basic pipeline. Thus, the initial investment into getting these assays up and running can result in many diverse experimental opportunities for (relatively) little additional technical effort.

4.2 FUTURE DIRECTIONS AND APPLICATIONS

In **Chapter 3**, I detailed my preliminary resistance maps for conformationally-selective Src inhibitors. Although promising, there is a lot more to expand upon beyond the initial analyses presented here. For instance, the unique structural patterns of resistance observed for each inhibitor (**Figure 3.2B)** will require deeper mechanistic dives. Given that these inhibitors are essentially probes for unique CD conformations; these results may have larger implications for our understanding of the structural features that influence kinase dynamics.

Our approach identified residues important for Src's regulatory modes, but kinase regulation is diverse. The described yeast assay could in theory have promise for identifying protein-intrinsic mechanisms of regulation in other kinases. For example, many other of the human tyrosine kinases have been expressed in yeast and are active (Corwin et al., 2017), suggesting it may be relatively straightforward to interrogate these other kinases. In particular, investigating more disease-relevant kinases, like BTK (a drug target in several blood cancers) (Wang et al., 2013) or LYN (a regulator of BCR signaling) (Nguyen et al., 2016) may yield clinically-translatable insights.

4.3 REFERENCES

Babu, M.M. (2016). The contribution of intrinsically disordered regions to protein function, cellular complexity, and human disease. Biochem. Soc. Trans. *44*, 1185–1200.

Corwin, T., Woodsmith, J., Apelt, F., Fontaine, J.-F., Meierhofer, D., Helmuth, J., Grossmann, A., Andrade-Navarro, M.A., Ballif, B.A., and Stelzl, U. (2017). Defining Human Tyrosine Kinase Phosphorylation Networks Using Yeast as an In Vivo Model Substrate. Cell Systems *5*, 128–139.e4.

Nguyen, P.-H., Fedorchenko, O., Rosen, N., Koch, M., Barthel, R., Winarski, T., Florin, A., Wunderlich, F.T., Reinart, N., and Hallek, M. (2016). LYN Kinase in the Tumor Microenvironment Is Essential for the Progression of Chronic Lymphocytic Leukemia. Cancer Cell *30*, 610–622.

Wang, M.L., Rule, S., Martin, P., Goy, A., Auer, R., Kahl, B.S., Jurczak, W., Advani, R.H., Romaguera, J.E., Williams, M.E., et al. (2013). Targeting BTK with ibrutinib in relapsed or refractory mantle-cell lymphoma. N. Engl. J. Med. *369*, 507–516.